Increased glutamate transporter-associated anion currents cause glial apoptosis in episodic ataxia 6

Peter Kovermann[1, 4, *], **Verena Untiet**[1, 3, 4], **Yulia Kolobkova**[1, 4], **Miriam Engels**[1], **Stephan Baader**[2], **Karl Schilling**[2], **Christoph Fahlke**[1, *]

[1]Institut für Biologische Informationsprozesse, Molekular- und Zellphysiologie (IBI-1), Forschungszentrum Jülich, 52428 Jülich, Germany

[2]Anatomisches Institut, Rheinische Friedrich-Wilhelm-Universität, 53115 Bonn, Germany

[3]present address: Center for Translational Neuromedicine, Københavns Universitet, 2200 København N, Denmark

[4]These authors contributed equally

[*]Correspondence: p.kovermann@fz-juelich.de (P.K.), c.fahlke@fz-juelich.de (Ch.F.)

Running title: Increased glial anion currents in episodic ataxia 6

Keywords: Bergmann glia, chloride homeostasis, episodic ataxia, glial apoptosis, glutamate transporters

Abbreviations: CF = climbing fiber; $[\mathrm{Cl}^-]_{int}$ = internal chloride concentration; CNQX = 6-cyano-7-nitroquinoxaline-2,3-dione; MQAE = 1-(Ethoxycarbonylmethyl)-6-methoxy-quinolinium bromide; TUNEL = Terminal *d*UTP nick end labeling; UCPH-101 = 2-Amino-5,6,7,8-tetrahydro-4-(4-methoxyphenyl)-7-(naphthalen-1-yl)-5-oxo-4*H*-chromene-3-carbonitrile

SUMMARY (177 words 400 maximum)

Episodic ataxia type 6 is an inherited neurological condition characterized by combined ataxia and epilepsy. A severe form of this disease with episodes combining ataxia, epilepsy and hemiplegia was recently associated with a proline to arginine substitution at position 290 of the excitatory amino acid transporter 1 in a heterozygous patient. The excitatory amino acid transporter 1 is the predominant glial glutamate transporter in the cerebellum. However, this glutamate transporter also functions as an anion channel, and earlier work in heterologous expression systems demonstrated that the mutation impairs the glutamate transport rate, while increasing channel activity. To understand how these changes cause ataxia, we developed a constitutive transgenic mouse model. Transgenic mice display epilepsy, ataxia, and cerebellar atrophy and thus closely resemble the human disease. We observed increased glutamate-activated chloride efflux in Bergmann glia that triggers apoptosis of these cells during infancy. The loss of Bergmann glia results in reduced glutamate uptake and impaired neural network formation in the cerebellar cortex. This study shows how gain-of-function of glutamate transporter-associated anion channels causes ataxia through modifying cerebellar development.

Keywords: glutamate transporters, chloride homeostasis, Bergmann glia, glial apoptosis, episodic ataxia

INTRODUCTION

Episodic ataxias (EAs) are rare neurological syndromes characterized by paroxysmal cerebellar incoordination, variably combined with epilepsy, dystonia and migraine-like headache (Jen *et al.*, 2007). Eight variants of autosomal dominant EAs (EA1−8) have been defined with different genetic origins. EA6 has been reported in only seven families, with clinical symptoms differing from those of other EA forms by the addition of long-lasting attacks of ataxia and epilepsy and the absence of myokymia, nystagmus, and tinnitus. Mutations in *SLC1A3,* encoding the glial excitatory amino acid transporter 1 (EAAT1), the human homologue of the glutamate-aspartate transporter (GLAST) (Storck *et al.*, 1992), were identified in all seven families (Jen *et al.*, 2005; de Vries *et al.*, 2009; Pyle *et al.*, 2015; Choi *et al.*, 2017a; Choi *et al.*, 2017b; Iwama *et al.*, 2017).

A heterozygous *SLC1A3* missense mutation predicting arginine replacement of a proline residue in transmembrane domain 5 of *h*EAAT1 (P290R) was identified in a 10-year-old boy, who had suffered from episodes of ataxia, epilepsy, and hemiplegia throughout his childhood (Jen *et al.*, 2005). The patient also experienced attacks of headache, visual field neglect, and hemiplegia for at least twice the duration of those in other EA patients. Magnetic resonance imaging scan showed mild cerebellar atrophy, and electroencephalography revealed subclinical seizure activity in one episode and epileptiform discharges in another one (Jen *et al.*, 2005). EAATs function as both secondary-active glutamate transporters and anion channels (Fahlke *et al.*, 2016), and P290R substitution exerts opposing effects on these functions in heterologous expression systems. It reduces the speed of conformational changes associated with Na^+ association/dissociation with the outward-facing EAAT1, thereby decreases the glutamate transport rate, and increases the open probability of the anion channel (Winter *et al.*, 2012; Hotzy *et al.*, 2013).

To investigate how changes in glial glutamate transporter function cause the neurological symptoms of EA6, we used a constitutive heterozygous mouse model carrying the targeted missense mutation in EAAT1/GLAST (*Slc1a3*$^{P290R/+}$).

MATERIAL AND METHODS

Animals

Wildtype (WT), homozygous GLAST knock-out (*Slc1a3*$^{-/-}$), and heterozygous GLAST mutant (*Slc1a3*$^{P290R/+}$) mice of both sexes with the genetic backgrounds: C57BL/6N (WT, *Slc1a3*$^{P290R/+}$) and 129/SvJ (WT, *Slc1a3*$^{-/-}$, *Slc1a3*$^{P290R/+}$), and FVB/N (Tg(GFAP–EGFP)14Mes/J) were studied at ages between P5−P800 (Supplementary Material). Mouse studies in this manuscript conforms with the Animal Research: Reporting of *In Vivo* Experiments (ARRIVE) guidelines (McGrath *et al.*, 2010).

Motor coordination testing

Motor coordination was tested in the ledge test (Guyenet *et al.*, 2010) by manually placing WT and mutant mice on a 1 cm wide ledge and encouraging them to walk along the ledge for 2´ by gentle nudges (Supplementary Material). Rotarod testing was performed by placing female mice (~P50) on an accelerating rotarod (Ugo-Basile, Italy) and measuring latencies to fall off the rotating rod. Mice usually underwent a short training and were subjected to three test sessions within two consecutive days (day 1, 10:00–12:00 h and 14:00–16:00 h; day 2, 10:00–12:00 h) after successful completion of this training. Each session consisted of three trials 10´ apart (Supplementary Material).

Visualization and quantification of specific cell types and components

Details about staining procedures and used antibodies are provided in the Supplementary Material and in Supplementary Table 2.

Preparation of acute cerebellar slices

After anesthetizing animals (P7–P900) with isoflurane and rapid decapitation, brains were placed in ice-cold oxygenated Ringer's solution A (in mM, 125 NaCl, 2.5 KCl, 1.25 NaH_2PO_4, 26 $NaHCO_3$, 0.5 $CaCl_2$, 5 $MgCl_2$, 20 $C_6H_{12}O_6$, 5% CO_2, and 95% O_2). Sagittal cerebellar slices (250 µm thick) were cut using a microtome ($\upsilon = 60$ Hz, amplitude = 1 mm) and transferred to a gauze slice holder in oxygenated Ringer's solution A for 30´ at 37°C, and 90´ to Ringer's solution B (125 NaCl, 2.5 KCl, 1.25 NaH_2PO_4, 26 $NaHCO_3$, 2 $CaCl_2$, 1 $MgCl_2$, 25 $C_6H_{12}O_6$) at RT. During experiments, the slices were constantly perfused with oxygenated Ringer's solution B or oxygenated ACSF (125 NaCl, 2.5 KCl, 1.25 NaH_2PO_4, 26 $NaHCO_3$, 2 $CaCl_2$, 1 $MgCl_2$). All experiments with acute slices were completed within 8 h after brain removal.

Cl^- current recordings in Bergmann glia cells

We performed whole-cell recordings of Bergmann glia cell anion currents in acute cerebellar slices of mice between P9−P14 under continuous perfusion with ACSF (artificial cerebrospinal fluid) at RT supplemented with 1 µM CNQX (Tocris Bioscience, Germany) using an EPC10 USB amplifier with PatchMaster software (HEKA Elektronik). Bergmann glia cells were visually identified by morphology and location in the Purkinje neuron layer. The pipette solution contained (in mM) 145 KCl, 1 $MgCl_2$, 10 HEPES/KOH (pH 7.2). Cells were held at membrane potentials of -80 mV/-100 mV/-120 mV, and glutamate-activated anion currents were elicited by application of Na-glutamate (1 mM) by a pressure-driven perfusion system

(PDES-DXH, NPI Electronic GmbH, Germany) coupled to standard micropipettes (Hilgenberg, Germany) placed 10–20 µm from the cell somata. A maximum of one Bergmann glia cell was tested per slice.

Fluorescence lifetime imaging microscopy

We measured the internal chloride concentration ($[Cl^-]_{int}$) of Bergmann glia cells by MQAE fluorescence lifetime imaging microscopy with an upright fluorescence microscope (A1 MP, Nikon, Netherlands) equipped with a 25× water immersion objective (Gensch, 2015; Untiet *et al.*, 2017). Acute cerebellar slices were incubated with 3.5 mM MQAE in Ringer's solution B for 30´. MQAE fluorescence is collisional quenched by Cl^- ions, resulting in a linear relationship between the inverse fluorescence lifetime and $[Cl^-]_{int}$ (Verkman, 1990):

$$\frac{\tau_0}{\tau} = 1 + K_{SV}\ [Cl^-]_{int} \text{ (Eq. 2)}$$

with $\boldsymbol{\tau}$ being the MQAE fluorescence lifetime at a given $[Cl^-]_{int}$, $\boldsymbol{\tau_0}$ the MQAE fluorescence lifetime in the absence of Cl^-, and K_{SV} the cell type-specific Stern–Volmer constant. After calibration in Bergmann glia cells using the 2-ionophore calibration experiments (Untiet *et al.*, 2017), $[Cl^-]_{int}$ for single cell soma was calculated from the mean fluorescence lifetime of all pixels within a defined region of interest. $[Cl^-]_{int}$ are given as means ± *CI* from 3–4 individual animals per time point and genotype.

Apoptosis assays

Bergmann glia cells were identified in acute cerebellar slices from the progeny of GFAP-EGFP reporter mice (FVB/N(GFAP-EGFP)14MES/J) crossbred with *Slc1a3*$^{P290R/+}$ mutants. After anesthetizing animals with isoflurane and rapid decapitation, brains were transferred into 4% PFA in phosphate buffer (PB, 30´, 4°C). Cerebella were then washed in PB (30´, RT) and incubated in PB supplemented with 10% $C_{12}H_{22}O_{11}$ (60´, RT) and 30% $C_{12}H_{22}O_{11}$ (12 h, 4°C) before embedding in NEG50 (Thermo Fisher Scientific, USA), and cut into sagittal slices (18 μm thick), using a HM560 microtome (MICROM, Germany). Slices were incubated with antibody against rabbit anti-active caspase 3 (CASP3) to label apoptotic cells. For immunochemical analysis, slices were incubated in CTA (5% ChemiBLOCKER−Merck-Millipore, 0.5% TritonX-100−Sigma Aldrich, 0.05% NaN_3, v/v) for 10´ and then overnight in CTA with primary antibody at RT. Secondary antibodies were applied in CTA for 60´. Apoptosis was quantified by averaging the number of CASP3-positive Bergmann glia cells per brain slice for each tested animal. TUNEL labeling of fragmented DNA in cerebellar nuclei was performed as a control for Bergmann glial apoptosis as described in Supplementary Material. Details about used antibodies/kits are listed in Supplementary Table 2.

Cell-attached recordings from Purkinje neurons

We visually identified Purkinje neurons in acute brain slices based on size and location between the granule cell layer and the molecular layer. For electrophysiological recordings pipettes (4–6 MΩ) were filled with a Ringer-like solution (in mM, 140 NaCl, 4 KCl, 10 HEPES/KOH, pH 7.4) and slices were constantly perfused with oxygenated ACSF (125 NaCl, 2.5 KCl, 2 $CaCl_2$, 2 $MgCl_2$, 1.25 NaH_2PO_4, 26 $NaHCO_3$) during the course of the experiment. Cell-attached patches were formed at neuron somata and currents were recorded at RT between 30´´ to 10´ in voltage-clamp mode at 0 mV (EPC10 amplifier, HEKA Elektronik). Data were analyzed off-line using Clampfit event-analysis functions (Molecular Devices, USA).

Statistical analysis

All statistical parameters were calculated with SigmaPlot (Systat Software GmbH), OriginPro (OriginLab Corp.), or Excel (Microsoft Corp.). Data are presented as means ($\bar{x}$), medians ($\tilde{x}_{0.5}$) ± CI (95% confidence interval), or σ (standard deviation) from individual animals. Ages are provided as postnatal days. Data were analyzed using Mann-Whitney *U*-tests or *2-way* ANOVA tests and Kruskal-Wallis ANOVA on ranks with Holm-Sidak or Dunn´s *post hoc* testing. *P*-values of ≤ 0.05 were considered significant with $P \leq 0.05$: *, $P \leq 0.01$: **, $P \leq 0.001$: ***; all *P*-values are provided in Supplementary Table 3.

Data availability

The source data that support the findings of this study are available from the corresponding author upon reasonable request.

RESULTS

Slc1a3$^{P290R/+}$ mice suffer from epilepsy and ataxia

Knock-in *Slc1a3*$^{P290R/+}$ mice (*Slc1a3*^{tm1P290RCfa}) were initially generated by homologous recombination in the C57BL/6N background (Supplementary Material; Supplementary Fig. 1). Heterozygous mice suffered from spontaneous generalized seizures and death during the weaning period with a peak between postnatal days (P) P25−P30 (Fig. 1A, gray), and we therefore backcrossed the mutation into the 129/SvJ strain, as a similar procedure has been successfully used to generate another animal model of severe epilepsy (Yu *et al.*, 2006). This change in genetic background reduced lethal seizure activity by about 70% ($n = 39/150$, C57/129Sv) and delayed the onset of the seizure period and the peak time of premature deaths to P35−P55 (Fig. 1A, red; Video 1). We monitored WT and *Slc1a3*$^{P290R/+}$ mice and scored fitness with respect to general condition, behavioral aspects, and EA6 associated pathology (Supplementary Table 1). Mutant male mice exhibited a severe phenotype with maximum scores between P40−P80, whereas female *Slc1a3*$^{P290R/+}$ mice showed a milder constitutive phenotype (Supplementary Fig. 2).

We assessed motor coordination by observing the *Slc1a3*$^{P290R/+}$ animals walking along the ledge of a cage (Fig. 1B) (Guyenet *et al.*, 2010). Ledge tests showed significantly more paw slips per step number in mutant animals (Fig. 1C; Video 2), with no difference between sexes ($n = 8/12/12/11$, WT♂/WT♀/Mut♂/Mut♀). Motor coordination was additionally tested by recording the time animals can walk on a rotating horizontal rod (Jones, 1968) (Fig. 1D–F). Fig. 1D shows averaged time series of consecutive rotarod sessions (labeled I−III) for WT and mutant animals on Kaplan-Meier curves (Kaplan, 1958). These values were corrected for episodes, in which mice did not walk forward, but rotated with the rotarod by holding on to it (spin failures, Supplementary Material; Fig. 1E and Supplementary Fig. 3A). In initial tests we observed a much higher frequency of such episodes for mutant male than for mutant female animals and therefore restricted rotarod testing to female animals (Supplementary Material). Compared with WT mice, mutant mice remained shorter times on the rotating rod and started significantly earlier to make mistakes (*n* = 8/7 animals, WT/Mut, Fig. 1F and Supplementary Fig. 3B). In the third trial, all WT performed the task without falling off and without spin failures, whereas 4/7 *Slc1a3*$^{P290R/+}$ animals still either fall off or rotated with the waltz (Fig. 1, D–F, Supplementary Fig. 3). In conclusion, *Slc1a3*$^{P290R/+}$ animals exhibit a robust EA6 phenotype with epilepsy and ataxia, thus resembling the phenotype of humans carrying the same mutation.

Cerebellar Bergmann glia cells from *Slc1a3*$^{P290R/+}$ mice degenerate during the second and third postnatal week

As EAAT1/GLAST is highly expressed in cerebellar Bergmann glia cells (Rothstein *et al.*, 1994; Torp *et al.*, 1994; Chaudhry *et al.*, 1995; Watase *et al.*, 1998), alterations in these cells likely represent initial steps in cerebellar dysfunction in *Slc1a3*$^{P290R/+}$ mice. Fig. 2A shows representative confocal images from the cerebellar cortex of WT and mutant mice (P20), immunostained with antibodies against glial fibrillary acidic protein (GFAP) and against brain lipid-binding protein (BLBP). Anti-BLBP permits visualization of Bergmann glia soma (Feng *et al.*, 1994), whereas anti-GFAP stains Bergmann glia fibers. In WT animals, Bergmann glia cells with typical unipolar morphology, i.e. soma in the Purkinje neuron layer and extensions in the molecular layer, were readily observed, however, such structures were absent in *Slc1a3*$^{P290R/+}$ mice at P20. We identified Bergmann glia cell fibers as GFAP-positive processes in the cerebellar molecular layer, which originate from Purkinje neuron layers, and counted them in WT and mutant animals between P5–P800. Prior to P10, WT and mutant animals had similar fiber numbers, indicating normal development of Bergmann glia in *Slc1a3*$^{P290R/+}$ mice to this age. However, between P10–P20, a pronounced age-dependent reduction in Bergmann glia cell fiber numbers occurred in *Slc1a3*$^{P290R/+}$ cerebella (Fig. 2B). GFAP-positive Bergmann glia fibers were reduced in all cerebellar regions, while glial development remained unaffected in the hippocampus and the cerebral cortex (data not shown). The number of Bergmann glia cell soma and fibers were reduced by a similar percentage (Fig. 2C), indicating loss of Bergmann glia cells and not mere retraction of fibers in the *Slc1a3*$^{P290R/+}$ cerebellum. Whereas the Bergmann glial cells were reduced by more than 70% in the Purkinje layer of mutant animals, the number of glial cells only slightly increased in the molecular layer (Fig. 2C). Immunostaining of cerebellar slices and western blotting of cerebellar lysates against the Bergmann glia markers Brain lipid binding protein (BLBP), S100β, and GLAST showed decreased numbers of Bergmann glia cell somata (Supplementary Fig. 4A, B) and reduced relative protein expression of the markers (Supplementary Fig. 4C, D and Supplement: uncropped_western_blots.pdf). These results indicate Bergmann glia cell death rather than mislocalization of glial cells to the molecular layer. In *Slc1a3*$^{-/-}$ (*Slc1a3*^{tm1Kta}, GLAST knockout) mice, the density of Bergmann glia cell fibers was not different from WT at P50 (Fig. 2B), demonstrating that loss of EAAT1/GLAST glutamate transporter does not result in Bergmann glia cell degeneration at this age (Watase *et al.*, 1998).

Altered cell distribution in the cerebellar cortex of *Slc1a3*$^{P290R/+}$ mice

Slc1a3$^{P290R/+}$ animals vary widely in cerebellar morphology, ranging from increased density of granule cells in the molecular layer (Fig. 2D, E and F, Supplementary Fig. 5A–F) to massive degeneration associated with foamy syncytial structures (Supplementary Fig. 5G and H). In contrast, adult WT cerebella are characterized by a defined layered structure with virtually no granule cells in the molecular layer. Since fibers from Bergmann glia cells and from their progenitors serve as migration pathways for cerebellar granule cells in the developing cerebellum (Rakic, 1971; Hatten *et al.*, 1984), changes in Bergmann glia function might result in the mislocalization of granule cells. In mutant cerebella without severe degeneration, we regularly observed mislocalized cells that are recognized by antibodies against NeuN, a specific nuclear marker for cerebellar granule cells (Mullen *et al.*, 1992; Weyer and Schilling, 2003) (Fig. 2D and E). We conclude that mutant EAAT1/GLAST expression impairs granule cell migration to the internal granule cell layer during development.

We also observed multipolar astrocytes in the molecular layer of *Slc1a3*$^{P290R/+}$ cerebella, which did not only differ from Bergmann glia cells in localization of their cell somas, but also in morphology (Fig. 2E and G). We co-stained slices with antibodies against glutamate receptor 1 and 2 (GLUR1, GLUR2) and GFAP (Fig. 2E and Supplementary Fig. 6A), since GLUR2 is expressed in astrocytes, but not in Bergmann glia cells (Keinanen *et al.*, 1990; Iino *et al.*, 2001; Droste *et al.*, 2017). Colocalization of GLUR2 and GFAP antibodies indicates that most of the ectopic glial cells were astrocytes rather than transformed Bergmann glia cells. We performed additionally immunostaining against glial proteins BLBP and S100β that distinguishes radial glia - expressing BLBP and S100β - and astrocytes - expressing S100β alone (Supplementary Fig. 6B) and provides additional evidence for invasion of reactive astrocytes into the molecular layer. Invasion of reactive astrocytes is a typical repair mechanism of the central nervous system (Sofroniew, 2005; Anderson *et al.*, 2014).

P290R expression alters the morphology and number of Purkinje neuron synapses in the cerebellum

Purkinje neurons form glutamatergic synapses with parallel fibers (PFs) or climbing fibers (CFs), and Bergmann glia cells not only provide a scaffold for the outgrowth of Purkinje neuron dendritic trees, but also ensheath newly developing synapses (Palay, 1974; Grosche *et al.*, 1999; Yamada *et al.*, 2000; Lordkipanidze and Dunaevsky, 2005). Ultrastructural analyses illustrate that most of these synapses are almost completely surrounded by Bergmann glia cell processes in WT animals. This close wrapping of Purkinje neuron synapses by Bergmann glia cells could not be observed in the molecular layer of *Slc1a3*$^{P290R/+}$ animals (Supplementary Fig. 7).

During development the number of CFs in contact with a certain Purkinje neuron is reduced to one, and these changes are associated with the formation of PF synapses (Woodward *et al.*, 1974; Crepel, 1982; Mariani, 1982). To test for developmental changes in mutant animals, we quantified glutamatergic and GABAergic synapses in mutant animals by immunostaining PF synapses with anti-VGLUT1, CF synapses with anti-VGLUT2 (Miyazaki *et al.*, 2003) or anti-GAD65/67 antibodies, which label GABAergic synapses (Fig. 3, Supplementary Material) in animals between P30–P65. All tested cerebellar regions of mutant animals had an increased density of VGLUT1-positive clusters of presynaptic boutons (Fig. 3A and B), while VGLUT2-positive clusters are reduced in all tested cerebellar regions of mutant animals (Fig. 3A and C). The density of GAD65/67-positive synapses was slightly reduced in the region between lobules V and VI of mutant animals, whereas nodular regions had similar GAD65/67-positive cluster densities in both WT and mutant animals (Fig. 3A and D). Taken together, these findings demonstrate that expression of P290R modifies synaptic morphology and connections in the cerebellum.

Increased P290R anion current is associated with glia cell apoptosis

P290R enhances EAAT1 anion currents in heterologous expression systems (Winter *et al.*, 2012), so that *Slc1a3*$^{P290R/+}$ Bergmann glia cells are expected to exhibit increased EAAT1/GLAST anion currents. We measured glutamate-elicited Cl^- currents using whole-cell patch clamping of Bergmann glia cells from acute brain slices of mice between P9–P14 by applying brief pulses (200 ms) of glutamate (1 mM) at a holding potential near to their reversal potential (-80 mV). In these experiments, the pipette solution contained (in mM) 145 KCl, 1 $MgCl_2$, 10 HEPES/KOH (pH 7.2). Bergmann glial cells were visually identified and distinguished from multipolar astrocytes - that are present in *Slc1a3*$^{P290R/+}$ molecular layers (Fig. 2E and G, Supplementary Fig. 6) - based on their size and location in proximity to Purkinje neurons. In a few cases, we inadvertently established the whole-cell configuration with neuronal cells, which could be easily distinguished from glial cells by their firing activity and discarded. Glutamate application elicited inward currents that were significantly increased in Bergmann glia cells from *Slc1a3*$^{P290R/+}$ mice (Fig. 4A, 60.7 ± 26.2/120.3 ± 63.2 pA, ±*CI*, n = 3/6 animals, WT/Mut, P = 0.024). Since P290R modifies the voltage dependence of EAAT1 anion currents and causes prominent activation by hyperpolarization (Winter *et al.*, 2012), we also compared glutamate-elicited currents of WT and *Slc1a3*$^{P290R/+}$ Bergmann glia cells at -100 mV, and -120 mV with their respective currents at -80 mV. Hyperpolarization caused only minor current increases in WT Bergmann glia cells, but significantly enhanced glutamate-elicited currents in *Slc1a3*$^{P290R/+}$ Bergmann glia cells (Fig. 4B–C).

Since EAAT1/GLAST anion channels are major determinants of the internal Cl^- concentration ($[Cl^-]_{int}$) in Bergmann glia cells (Untiet *et al.*, 2017), it was mandatory to test how increased EAAT1/GLAST anion currents affect $[Cl^-]_{int}$ in *Slc1a3*$^{P290R/+}$ Bergmann glia cells. We performed fluorescence lifetime imaging microscopy using the Cl^--sensitive dye MQAE in acute cerebellar slices (Untiet *et al.*, 2017) between P4–P14 (Methods, Fig. 4D–F). $[Cl^-]_{int}$ was lower in *Slc1a3*$^{P290R/+}$ mice than in WT, and incubation of *Slc1a3*$^{P290R/+}$ slices with the EAAT1/GLAST blocker UCPH-101 (10 µM) increased the $[Cl^-]_{int}$ to values close to those of WT (Fig. 4F). In Bergmann glia cells $[Cl^-]_{int}$ is in a dynamic equilibrium between Cl^- accumulation via NKCC transporters and Cl^- efflux through EAAT anion channels (Untiet *et al.*, 2017). Changes in numbers or transport rates of each protein shift the equilibrium and modify $[Cl^-]_{int}$. Reduced $[Cl^-]_{int}$ thus provide additional evidence for increased Cl^- efflux in *Slc1a3*$^{P290R/+}$ Bergmann glia cells.

We observed small difference in $[\mathrm{Cl}^-]_{int}$ between WT and mutant mice also in the first postnatal week, i.e. before onset of glutamatergic innervation. EAAT1/GLAST is expressed at these ages (Schreiner *et al.*, 2014), and EAAT anion channels are not exclusively activated by external glutamate, but also assume a basal activity under glutamate-free conditions or with internal glutamate (Fahlke *et al.*, 2016). Increased activity of P290R EAAT1/GLAST anion channels thus fully accounts for altered $[\mathrm{Cl}^-]_{int}$ also at ages below P7.

$[\mathrm{Cl}^-]_{int}$ was smaller in *Slc1a3*$^{P290R/+}$ than in WT Bergmann glia cells, but still larger than expected for passive distribution. Thus, activation of EAAT1/GLAST and EAAT2/GLT-1 anion channels at the onset of glutamatergic synaptic transmission during the second postnatal week (Watanabe and Kano, 2011) results in Cl^- efflux from Bergmann glia cells in both *Slc1a3*$^{P290R/+}$ and WT animals. These currents are larger in *Slc1a3*$^{P290R/+}$ as in WT animals and might cause cell shrinking and apoptosis of mutant Bergmann glia cells (Porcelli *et al.*, 2004; Ernest *et al.*, 2008). We crossed reporter mice with GFAP-conjugated enhanced green fluorescent protein (GFAP-EGFP) with *Slc1a3*$^{P290R/+}$ animals, stained cerebellar tissue from P9–P15 with antibodies for active caspase-3 (CASP3), and identified apoptotic glial cells by colocalization of EGFP and CASP3 (Fig. 5A and B). Fig. 5B shows the numbers of apoptotic cells from WT and *Slc1a3*$^{P290R/+}$ brain slices during postnatal development, demonstrating significantly increased levels of apoptotic events in mutant cerebella (Fig. 5B, left) and significantly more apoptotic Bergmann glial cells (Fig. 5B, right) between P10–P13 in the animal model. Since CASP3 activation was reported also during normal development (Oomman *et al.*, 2005), we additionally tested the apoptosis marker TUNEL in GFAP-EGFP expressing mice of both genotypes (Gavrieli *et al.*, 1992). We observed substantially more TUNEL signals in mutant than in WT cerebella (Fig. 5C). In mutant animals TUNEL co-localizes with nuclei of cells expressing GFAP-EGFP in the Purkinje cell layer, indicating glia apoptosis. (Fig. 5D and E). The number of apoptotic Bergmann glia cells detected by

TUNEL/GFAP-EGFP co-localization was comparable to the CASP3 assay between P10−P13 (CASP3: 10.2 ± 2.9, TUNEL: 20.2 ± 15.1, means ± *CI*, n = 15/7 mutant animals, CASP3/TUNEL). We also observed increased numbers of TUNEL and of CASP3 signals that did not co-localize with GFAP, (Fig. 5A and B, and Fig. 5C−E, CASP3: 33.6 ± 6.2, TUNEL: 149.4 ± 96.8, means ± *CI*, n = 15/7 mutant animals, CASP3/TUNEL). These signals might be due to earlier apoptosis events of Bergmann glial cells or to apoptosis of other cell types, such as migrating granule cells in the external granule cell layer.

Abnormal spiking properties of *Slc1a3*$^{P290R/+}$ Purkinje neurons

Cerebellar Purkinje neurons represent the only neuronal output of the cerebellar cortex (Marr, 1969). In the absence of synaptic input, they fire action potentials with precisely regulated interspike intervals (ISIs) (Bell and Grimm, 1969; Arancillo *et al.*, 2015), and changes in the frequency and in the temporal precision of ISIs are known to impair motor coordination (Hoebeek *et al.*, 2005; Walter *et al.*, 2006; Alvina and Khodakhah, 2010; Jayabal *et al.*, 2017). We measured spontaneous simple spiking activity with cell-attached patch clamp recordings (Donato *et al.*, 2006) in vermal regions in lobes V/VI, VI to VIII and VIII/IX of acute WT and mutant cerebellar slices. Representative recordings from WT and *Slc1a3*$^{P290R/+}$ mice at P10 (Fig. 6A) and P40 (Fig. 6C) demonstrate typical biphasic spikes, corresponding to inward and outward currents during action potentials (Womack and Khodakhah, 2002). In Purkinje neurons from WT animals the spontaneous spiking frequency increases during development from 10.1 ± 7.9 Hz at P10 to 35.8 ± 11.8 Hz at P40 (±*CI*, n = 7/6 animals). In *Slc1a3*$^{P290R/+}$ animals, the developmental acceleration was less pronounced, resulting in significantly slower firing in mutant Purkinje neurons at P40 (10.4 ± 11.9 Hz, ±*CI*, n = 4 animals) (Fig. 6E).

To compare the temporal precision of simple spiking activities, we calculated ISI covariances (CV) and intrinsic variabilities (CV2) for WT and mutant Purkinje neurons (Holt *et al.*, 1996). For all tested ages, CV and CV2 were not different between WT and mutant Purkinje neurons (Fig. 6F and G). The CV values observed in *Slc1a3*$^{P290R/+}$ animals were in good agreement with other reports studying acute slices at similar temperatures (Wulff *et al.*, 2009; Jayabal *et al.*, 2017). Smaller CV values (below 0.1) were only reported in acute slices from older mice (Jayabal *et al.*, 2016) or in studies at physiological temperatures (Hansen *et al.*, 2013). We conclude that the developmental acceleration of simple spike frequencies (McKay and Turner, 2005) is absent in *Slc1a3*$^{P290R/+}$, probably due to progressive glia and neuron degeneration.

Loss of Bergmann glia modifies climbing fiber regulation of Purkinje neuron activity in *Slc1a3*$^{P290R/+}$ mice

Bergmann glial processes ensheath glutamatergic synapses between CFs and Purkinje neurons (Supplementary Figure 7), and glutamate uptake into Bergmann glial processes helps reducing glutamate spillover from the synaptic cleft after simultaneous release of multiple synaptic vesicles (Wadiche and Jahr, 2001). The CF-Purkinje neuron synapse thus represents a system well suited to study the functional consequences of EAAT1/GLAST dysfunction and Bergmann glia degeneration on glutamatergic synaptic transmission in the cerebellum.

CF activity typically interrupts simple spike activity for periods up to several hundred ms, the so-called CF pauses (Eccles *et al.*, 1966; Bell and Grimm, 1969; Latham and Paul, 1971; Sato *et al.*, 1992). These pauses play a role in signal transmission to the deep cerebellar nuclei during learning processes (Otis *et al.*, 2012). We measured the lengths of these pauses in WT and *Slc1a3*$^{P290R/+}$ Purkinje neurons after pulses with supersaturating glutamate concentrations at ages below P30. At these ages, simple spike activity was similar for WT and mutant Purkinje neurons (Fig. 6E). Fig. 7A depicts representative responses from WT and mutant Purkinje neurons to glutamate application, and in Fig. 7B, aligned simple spike events were plotted versus time with corresponding histograms of aligned events binned at 100 ms, before and after the glutamate puff. In WT Purkinje neurons the glutamate application evokes a short period of augmented spike firing, followed by a short depressed phase as described earlier (Tang *et al.*, 2017). While the baseline simple spike activities are recovered within several seconds after the pulse in WT Purkinje neurons (1.2 ± 0.7 sec) in most cases, silent periods were significantly longer in *Slc1a3*$^{P290R/+}$ Purkinje neurons (39.2 ± 57.2 sec, ±*CI*, $n = 10/3$ animals, $P = 0.011$, Fig. 7C). We conclude that glutamate uptake is severely reduced in *Slc1a3*$^{P290R/+}$ mice and results in altered synaptic transmission between CFs and Purkinje neurons.

Cerebellar degeneration in *Slc1a3*$^{P290R/+}$ mice

We reasoned that the absence of Bergmann glia cells might result in cerebellar atrophy and compared the sizes of WT and *Slc1a3*$^{P290R/+}$ cerebella in old mice (i.e. > P180). Quantification of cerebellar transversal areas revealed smaller values in all tested *Slc1a3*$^{P290R/+}$ than in corresponding WT animals (Fig. 8A), due to a reduction of all cerebellar regions (Fig. 8B). We observed similar alterations in mutant female and male mice ($n = 5/5$ animals, Mut♂/Mut♀, $P = 0.55$), and thus pooled results from both sexes in subsequent analyses. The mean size was reduced by 37 ± 13% (±σ, $n = 10/10$ animals, WT/Mut) in *Slc1a3*$^{P290R/+}$, and six out of ten cerebella were reduced by > 35% in transversal sizes. Nissl staining of slices from whole vermis regions of mutant mice show fewer cerebellar lobes and a smaller total sagittal plane, with smaller granule cell layers and molecular layer areas (Fig. 8C and D). There was no obvious size reduction in white matter area of *Slc1a3*$^{P290R/+}$ slices ($n = 4/4$ animals, WT/Mut, Fig. 8D). We additionally compared the number of Purkinje cells and the thickness of molecular layers from younger WT and mutant animals (P27−60) from lobes VI and X. There was no difference in molecular layer thickness between genotypes ($P = 0.391$). The number of Purkinje cells was significantly reduced in the external region of mutant lobes VI (4.4 ± 0.5/3.7 ± 1.3 Purkinje neurons/100 µm, ±*CI*, $n = 8/11$, WT/Mut, $P = 0.003$), but not in the other tested regions (Supplementary Fig. 8). We conclude that loss of Bergmann glia cells leads to generalized cerebellar degeneration in *Slc1a3*$^{P290R/+}$ mice, likely because Bergmann glial apoptosis impairs glutamate removal and causes excitotoxic Purkinje neuron death.

DISCUSSION

Episodic ataxia type 6 is an inherited condition characterized by impaired motor coordination with epilepsy and migraine-like headache. Thus far, all reported cases have been associated with mutations in *SLC1A3* (Jen *et al.*, 2005; de Vries *et al.*, 2009; Pyle *et al.*, 2015; Choi *et al.*, 2017a; Choi *et al.*, 2017b; Iwama *et al.*, 2018), but how these mutations cause the specific clinical phenotype of episodic ataxia is still insufficiently understood. To answer this question we used a knock-in mouse model expressing EAAT1/GLAST carrying a mutation recently described in a human patient (Jen *et al.*, 2005). *Slc1a3*$^{P290R/+}$ mice suffer from epileptic attacks, ataxia and cerebellar atrophy and thus exhibit similar neurological symptoms as the patient with the same mutation. Disease-associated *SLC1A3* mutations were initially assumed to modify glutamate transport rates and to affect synaptic transmission via decreased EAAT1 glutamate uptake. However, comparison of the neurological symptoms of *Slc1a3*$^{P290R/+}$ and the corresponding knock-out animal *Slc1a3*$^{-/-}$ - that lacks completely EAAT1/GLAST-mediated glutamate uptake and only suffers from moderate impairment of motor coordination (Watase *et al.*, 1998; Perkins *et al.*, 2016) - argues against this assumption. We here demonstrate that expression of P290R EAAT1 reduces glutamate uptake by a different mechanism: gain-of-function of EAAT1/GLAST Cl^- currents significantly impairs cerebellar glutamate homeostasis by causing Bergmann glia degeneration.

P290R causes gain-of-function of *h*EAAT1 anion channel activity in heterologous expression systems (Winter *et al.*, 2012), and we found significantly increased glutamate-induced anion currents in *Slc1a3*$^{P290R/+}$ Bergmann glia cells. Although Bergmann glia $[Cl^{-}]_{int}$ was slightly lower in mutant than in WT, these values were significantly larger than expected for passive distributions (Fig. 4). Increased P290R EAAT1/GLAST anion channel activity will thus result in enhanced Cl^{-} efflux and excessive cell shrinkage in *Slc1a3*$^{P290R/+}$ Bergmann glia cells upon establishment of glutamatergic synaptic signaling in the second postnatal week. Cl^{-} loss and cell shrinkage can trigger apoptosis (Walev *et al.*, 1995; Friis *et al.*, 2005), and EAAT1/GLAST anion channel gain-of-function can thus account for glial apoptosis in *Slc1a3*$^{P290R/+}$ at ages between P9–P14 (Fig. 4 and 5). We were not able to show cell shrinkage in mutant animals directly, most likely since cell shrinkage leads to apoptosis in a fast and irreversible manner. EAAT1/GLAST is highly expressed in glial cells in the cerebellum, so Bergmann glia cell apoptosis is likely to be the first stage of cerebellar degeneration (Fig. 2 and 5).

We observed Bergmann glial apoptosis with two markers, TUNEL and CASP3 (Fig. 5). Recent reports (Oomman *et al.*, 2004; Oomman *et al.*, 2005) described a constitutive expression of CASP3 in a large percentage of rat Bergmann glial cells, whereas other apoptosis markers as TUNEL or Annexin V were absent. We could only detect CASP3 expression in apoptotic cells in mutant animals, but not in WT Bergmann glial cells, suggesting species-specific roles of CASP3 in mouse and rat.

Spontaneous spiking of Purkinje neurons is controlled by feed-forward inhibition by interneurons (Marr, 1969; Midtgaard, 1992; Hausser and Clark, 1997; Wulff *et al.*, 2009) and thus represents a marker for the integrity of the cerebellar network. Although Purkinje neuron activity was comparable in young WT and mutant animals, degenerative processes result in lower frequency spiking in adult *Slc1a3*$^{P290R/+}$ mice (Fig. 6). Similar changes in Purkinje neuron activity were observed in another ataxia animal model, the ataxin 2 (*Atxn2*) mouse carrying a mutation of ataxin 2 (ATXN2^{Q127}: Tg(Pcp2-ATXN2*127Q)#Plt/0) found in patients with spinocerebellar ataxia type 2. These animals exhibited cerebellar degeneration and decreased Purkinje neuron firing rates, with no major difference in firing precision (Hansen *et al.*, 2013).

Purkinje neurons receive glutamatergic inputs from olivary climbing fibers, with synaptic activity usually followed by a period without spontaneous spiking (Eccles *et al.*, 1966; Bell and Grimm, 1969; Latham and Paul, 1971; Sato *et al.*, 1992), the so-called CF pause. The prominent Bergmann glia degeneration in *Slc1a3*$^{P290R/+}$ causes a significant reduction in glutamate uptake in these animals that results in increased CF pause durations in Purkinje neurons of these mice (Fig. 7). Changes in CF pause durations are a common finding in mouse models for ataxia and hemiplegic migraine, for example in a migraine mouse model carrying a mutation in *Cacna1a* (Gao *et al.*, 2012) or in ataxic mice lacking BK channels (Cheron *et al.*, 2009).

Slc1a3$^{P290R/+}$ animals exhibit degradation of Bergmann glia in the cerebellum, but not of glial cells in other brain regions such as hippocampus or cortex. This difference is likely due to separate expression levels of EAAT1/GLAST and/or distinct $[Cl^{-}]_{int}$ in Bergmann glia. Insertion of the homologous P>R mutation into *Drosophila* EAAT1 (Eaat1$^{P>R}$) or expression of mutant human EAAT1 caused episodic paralyzes with compromised astrocyte morphology and developmental impairment in *Drosophila* larvae (Parinejad *et al.*, 2016). This phenotype was mimicked by overexpression of K^{+}-Cl^{-} cotransporter and could be rescued by Na^{+}-K^{+}-$2Cl^{-}$ cotransporter expression. These findings highlight the physiological importance of $[Cl^{-}]_{int}$ homeostasis for glial function, but also identify differences between mouse Bergmann glia cells and *Drosophila* glial cells: Bergmann glial apoptosis is an initial stage of cerebellar degeneration in *Slc1a3*$^{P290R/+}$ mice, while Eaat1$^{P>R}$ larvae have impaired astrocyte infiltration but no degeneration. Glial cells express various Cl^{-}-coupled transporters, whose function might be modified by reduced $[\mathrm{Cl}^-]_{int}$ in *Slc1a3*$^{P290R/+}$ mice. Glial GATs are $\mathrm{Na}^+/\mathrm{Cl}^-$/GABA transporters, and the observed changes in $[\mathrm{Cl}^-]_{int}$ would cause a reduction of resting [GABA] by about 20% between P10–P12. $\mathrm{Cl}^-/\mathrm{HCO}_3^-$ exchange might modify intracellular pH in *Slc1a3*$^{P290R/+}$glia. However, since the main alteration in *Slc1a3*$^{P290R/+}$ is a dramatic reduction in the number of Bergmann glia cells, all these predicted changes are minor compared with the morphological changes.

So far, five different brain disorders have been associated with *SLC1A3* mutations: episodic ataxia (Jen *et al.*, 2005; de Vries *et al.*, 2009; Choi *et al.*, 2017a; Iwama *et al.*, 2018); migraine (Kovermann *et al.*, 2017); Tourette syndrome (Adamczyk *et al.*, 2011); attention deficit hyperactivity disorder (ADHD) and autism (van Amen-Hellebrekers *et al.*, 2016). Although the underlying physiological mechanisms are insufficiently understood, these conditions might share fundamental pathophysiological processes: a sequence variant predicting E219D, found in some individuals with Tourette syndrome (Adamczyk *et al.*, 2011), increases the relative probability of surface membrane insertion for human EAAT1; and *SLC1A3* duplication is likely to increase EAAT1 expression in ADHD and autism. In these diseases, increased EAAT1 numbers in the surface membrane are expected to enhance glutamate-activated anion currents in glial cells. It is tempting to speculate that these changes might alter glial function and neuronal migration, resulting in changes of neuronal network formation and function.

EAAT glutamate transporters are prototypical dual function proteins that mediate secondary-active glutamate transport and anion conductance. Although the structural basis of these two different transport processes has been established (Machtens *et al.*, 2015), the physiological impact of linking these distinct functions remains less clear. It is now clear that EAATs play a major role in regulating glial $[\mathrm{Cl}^-]_{int}$ in the mammalian central nervous system (Untiet *et al.*, 2017) and in glial differentiation in *Drosophila* (Parinejad *et al.*, 2016). Our work illustrates how changes in EAAT1 anion channel activity can have dramatic consequences on differentiation and integrity of the cerebellum. It has been known for decades that glial and neuronal EAATs have differences in anion channel activity (Wadiche *et al.*, 1995). Our findings highlight the impact of low glial EAAT anion channel activity on glial Cl^- homeostasis. Animals carrying a heterozygous P290R mutation, have only moderately increased EAAT-mediated anion currents, but exhibit dramatic changes in cerebellar differentiation and profound cerebellar degeneration. Hence, glial EAATs must be optimized for both effective secondary-active transport and low anion channel activity.

ACKNOWLEDGEMENTS

We are grateful to Christoph Aretzweiler, Marcel Böttcher, and Tanja Mertens, for technical assistance with genotyping and care of animals, and to Dr. Niels Danbolt for providing *Slc1a3*$^{-/-}$ knock-out animals. We acknowledge Nikola Kornadt-Beck for help with legal aspects of animal breeding, and Stefanie Ramrath for help in preparing sections for ultrastructural analyses, and Drs. Thomas Gensch, Arnd Baumann, and Anja Mataruga for helpful discussions.

FUNDING

This work was supported by the German Ministry of Education and Research (E-RARE network Treat-ION, BMBF 01GM1907C) to Ch. F. and by the German Research Foundation (FOR 2795; FA 301/13-1) to Ch. F..

COMPETING INTERESTS

The authors declare no conflict of interest.

FIGS AND FIG LEGENDS

Figure 1 – *Slc1a3*$^{P290R/+}$ mice suffer from epilepsy and ataxia. Image (A) depicts survival rates for C57BL/6 (gray) and 129/SvJ (red) *Slc1a3*$^{P290R/+}$ mice over time, with shaded areas indicating periods with pronounced seizure activity. Representative screen shots (B) from video recordings of WT and *Slc1a3*$^{P290R/+}$ mice moving on a ledge indicate that transgenic mice tend to slip (arrowheads) from the ledge with their hindlimbs. The whisker plot (C) shows the median paw slip numbers per step for adult (P50) WT (black) or *Slc1a3*$^{P290R/+}$ (red) mice of both sexes (circles, ♂; squares, ♀). The analysis revealed no detectable sex differences in Ledgetest performance ($P = 0.110$), but pronounced differences between genotypes in both sexes ($n = 8/12/12/11$, WT$^{♂}$/WT$^{♀}$/Mut$^{♂}$/Mut$^{♀}$, $P \leq 0.001^{♂}/P = 0.001^{♀}$). The averaged time series of mean scores (D) for three consecutive rotarod trial sessions (I–III) with adult female WT (black) or *Slc1a3*$^{P290R/+}$ (red) mice at P50 point to differences between WT and mutant animals. The increased mean spin failure frequencies (E) for WT or *Slc1a3*$^{P290R/+}$ ($P = 0.011$) and the decreased rotarod latencies to fall (F) indicate that *Slc1a3*$^{P290R/+}$ mice suffer from ataxia ($n = 8/7$, WT/Mut, $P = 0.031$). Data are shown as whisker-box plots with medians (whisker: 5-95th percentile, box: 25-75th percentile, single (C) and repeated measure (E, F) 2-*way* ANOVA and Holm-Sidak *post hoc* test); $^{*}P \leq 0.05$, $^{**}P \leq 0.01$, $^{***}P \leq 0.001$; all *P*-values are available online for this figure (Supplementary Table 3).

Video 1 – Representative seizure of a mutant mouse. Heterozygous *Slc1a3*$^{P290R/+}$ animal exhibit spontaneous generalized seizure during the weaning period (postnatal day 30).

Video 2 – Motor coordination of wildtype and heterozygous *Slc1a3*$^{P290R/+}$ mice during ledge tests. Mutant animals tend to slip with the hindlimbs from the ledge, during crossings (postnatal day 58).

Figure 2 – Degeneration of Bergmann glia cells and cellular reorganization of the cerebellar cortex in *Slc1a3*$^{P290R/+}$ mice. Representative confocal images (A) of paraffin-embedded cerebellar WT (top) or *Slc1a3*$^{P290R/+}$ (bottom) slices showing the vermis region of lobe V/VI immunostained for BLBP (yellow) and GFAP (P20, magenta), and indicate age-dependent changes in the numbers of Bergmann glia cell fibers (B) in the molecular layers of WT (black), *Slc1a3*$^{-/-}$ (orange) or *Slc1a3*$^{P290R/+}$ (red) cerebella. The data represent mean numbers of GFAP$^{\text{positive}}$ fibers per 100 µm Purkinje cell layer (PCL) in individual animals (*n* = 25/32 animals, WT/Mut). Bergmann glial cell numbers were counted (C) in the PCL and in the molecular layer (ML), and indicated that the median cell loss is much higher than the number of ectopic cells in the ML. Cerebellar regions stained for Nissl (D, P50) or stained for NeuN (E, > P100, green) indicate regions with anomalous enrichment of NeuN$^{\text{positive}}$ cells (E, arrowheads). The white boxes depict linear arrangements of Nissl-stained nuclei within the molecular layer of *Slc1a3*$^{P290R/+}$ mice (D). The whisker-box plots (F, G) show increased density of NeuN$^{\text{positive}}$ cells (F, *n* = 14/16 animals, WT/Mut) and increased density of GFAP$^{\text{positive}}$ cells (G, *n* = 14/19 animals, WT/Mut) in mutant lobes V/VI. Astrocytes mislocalize to the molecular layer in mutant cerebella; confocal images of the nodular region (E, bottom) of a *Slc1a3*$^{P290R/+}$ animal (> P100) immunostained for GFAP (magenta) and NeuN (green) indicate multipolar astrocytes in the molecular layer from mutant animals (E, bottom, left). Colocalization (white) of GLUR2 (yellow) with GFAP (magenta) in the molecular layer (E, bottom, right) of a *Slc1a3*$^{P290R/+}$ mouse shows that GFAP$^{\text{positive}}$ multipolar astrocytes do not emerge from the Bergmann glia cell pool (see also Supplementary Fig. 6). The density of GFAP$^{\text{positive}}$ multipolar cells in the molecular layers increases over time in *Slc1a3*$^{P290R/+}$ mice, but not in WT mice. Scale bars: 100 µm (A), 50 µm (D), 50/25 *µm* (E, top/bottom). Numbers of Bergmann glia fibers over time (B) are shown as means ± *SEM* of individual animals and genotype specific

differences over time were analyzed with 2-*way* ANOVA and Holm-Sidak *post hoc* testing. Data in C, F, and G are shown as whisker-box plots (whisker: ±*CI*, box: 25-75th percentile with each data point representing the values obtained from one individual animal (2-*way* ANOVA and Holm-Sidak *post hoc* tests; $^{*}P \leq 0.05$, $^{**}P \leq 0.01$, $^{***}P \leq 0.001$; all *P*-values are available online for this figure (Supplementary Table 3). Abbreviations: GCL – granule cell layer, ML – molecular layer, PCL – Purkinje cell layer.

Figure 3 – Altered synapse densities in *Slc1a3*$^{P290R/+}$ cerebella. Representative confocal images of WT and *Slc1a3*$^{P290R/+}$ cerebellar molecular layers (A) immunostained for the vesicular glutamate transporter VGLUT1 (blue, parallel fibers), VGLUT2 (red, climbing fibers) or for glutamate decarboxylase isoforms 65 and 67 (GAD65/67, yellow). Images (A) show overviews and magnified insets. Median densities of glutamatergic VGLUT1$^{\text{positive}}$ (B) and glutamatergic VGLUT2$^{\text{positive}}$ (C) clusters of synaptic boutons are different in WT and mutant animals, whereas the densities of GABAergic clusters (D) are similar (*n* = 3-5/5-7 in B; *n* = 3-5/5-9 animals in C; *n* = 4-7/4-8 animals in D (WT/Mut). Scale bars (A): overviews, 50 µm; insets, 10 µm. Data in B–D are shown as whisker-box plots with medians (whisker: ±*CI*, box: 25-75th percentile, each data point represent the mean density from an individual animal (2-*way* ANOVA and Holm-Sidak *post hoc* test); $^{*}P \leq 0.05$, $^{**}P \leq 0.01$, $^{***}P \leq 0.001$, all *P*-values are available online for this figure (Supplementary Table 3). Abbreviations: GCL – granule cell layer, ML – molecular layer, PCL – Purkinje cell layer.

Figure 4 – Enhanced EAAT1/GLAST chloride currents in *Slc1a3*$^{P290R/+}$ Bergmann glia cells. Bar graph (A) depicts pooled mean peak whole-cell current responses of Bergmann glia (-80 mV) to brief pulses (200 ms) of 1 mM L-Glu from experiments with acute cerebellar brain slices (±*CI*, *n* = 3/6 animals, big circles, WT/Mut). Individual tested cells are shown as shaded

small circles. In (B) representative glutamate-induced Bergmann glia cell whole-cell currents are shown for three different holding potentials for WT and mutant cells. A bar graph (C) summarizes Bergmann glia peak current responses of individual WT and *Slc1a3*$^{P290R/+}$ cells for the voltages -100 and -120 mV, normalized to their respective currents at -80 mV (±*CI*, n = 6/3–4 cells, WT/Mut). Representative FLIM recordings of cerebellar cortices (D) from WT and *Slc1a3*$^{P290R/+}$ mice at P11 reveal decreased $[Cl^-]_{int}$ in mutant Bergmann glia cells (*arrows*). $[Cl^-]_{int}$ is color-coded according to the color bar between images (Scale bar: 25 µm). Point plots (E) depict mean $[Cl^-]_{int}$ during first and second week of development for individual animals (big circles). $[Cl^-]_{int}$ of Bergmann glial cells was measured in WT and in *Slc1a3*$^{P290R/+}$ slices. Figure F summarizes data from the period with genotype-specific differences in the absence and in the presence of the EAAT1/GLAST-specific antagonist UCPH-101 (Abrahamsen *et al.*, 2013). In A and C data points are means ± *CI* from individual animals (A, Mann-Whitney *U*-test) or cells (C, 2-*way* ANOVA with repeated measures and Holm-Sidak *post hoc* tests). Data in E and F are presented and statistically analyzed as means ± *CI* of individual animals (big circles, 2-*way* ANOVA with Holm-Sidak *post hoc* test (E); Kruskal-Wallis ANOVA on ranks with Dunn´s *post hoc* test versus WT control (F)). Distribution of measured individual cells is depicted in the background (A, E, F, small circles); $^{*}P \leq 0.05$, $^{**}P \leq 0.01$, $^{***}P \leq 0.001$; all *P*-values are available online for this figure (Supplementary Table 3). Abbreviations: GCL – granule cell layer, ML – molecular layer, PCL – Purkinje cell layer.

Figure 5 – *Slc1a3*$^{P290R/+}$ Bergmann glia cell loss is caused by apoptosis during the second postnatal week. Apoptosis of Bergmann glia cells visualized by confocal imaging (A) of a *Slc1a3*$^{P290R/+}$ cerebellar cortex immunostained for GFAP and CASP3 (Scale bars: 50 µm) with colocalization of CASP3/GFAP-EGFP (asterisks) and CASP3 (hash) signals in a transgenic mouse. Point plots of mean numbers of total CASP3$^{\text{positive}}$ cells and CASP3$^{\text{positive}}$ Bergmann glia

of individual animals over time (B) demonstrate increased numbers of apoptotic Bergmann glia cells in *Slc1a3*$^{P290R/+}$ animals during the second postnatal week. Confocal images from whole sagittal cerebellar slices stained for fragmented DNA (C, EGFP/TUNEL) and magnified views from ROI (D) of mutant cerebellum as indicated in C. Merged views of EGFP/TUNEL and of TOPRO-3/TUNEL show the overlap of GFAP-EGFP and TUNEL signals, and the localization of TUNEL signals in the nuclei (C, arrowheads). Bar graphs in B show the mean numbers (±*CI*) of apoptotic signals (left) and the mean numbers of EGFP/CASP3 colocalized signals (right) per individual animal (n = 3–5 animals per genotype and age group, 2-*way* ANOVA with Holm-Sidak *post hoc* test). Bar graphs in E show the mean total numbers of TUNEL signals for individual animals ($n = 6/7$, WT/Mut, left) and the mean numbers (±*CI*) of GFAP-EGFP/TUNEL colocalized signals for the same animals (right). Statistical analyses were done with Kruskal-Wallis ANOVA on ranks and Dunn´s *post hoc* test for colocalized signals (left) and total apoptosis events (right), separately. Confocal image (F) shows colocalization of EGFP/TUNEL/CASP3. Scale bars: 100 µm (A), 1 mm (C); 100 µm, 25 µm, 10 µm (D); 10 µm (F); $^{*}P \leq 0.05$, $^{**}P \leq 0.01$, $^{***}P \leq 0.001$; all *P*-values are available online for this figure (Supplementary Table 3). Abbreviations: EGCL – external granule cell layer, GCL – granule cell layer, ML – molecular layer, PCL – Purkinje cell layer.

Figure 6 – *Slc1a3*$^{P290R/+}$ Purkinje neurons display abnormal spiking properties. Current traces obtained from cell-attached patch clamp recordings (A, C) show patterns of spontaneous firing from individual Purkinje neurons in acute slices from juvenile (A, P10) or adult (C, P40) WT or *Slc1a3*$^{P290R/+}$ mice. Burst plots (B, D) of representative Purkinje neuron spike trains for juvenile (B) or adult (D) WT or *Slc1a3*$^{P290R/+}$ mice. Spikes are shown as red bars and interspike intervals in gray scale according to the temporary covariance (CV2). Purkinje neuron mean simple spike frequencies (E) differ between P40 WT and mutant animals, whereas mean

absolute covariances (F) and mean covariances of interspike intervals (G) are similar in WT and mutant animals. Pooled data are shown as bars with means ± *CI*, with (E–G) representing mean values from the same animals (P10, $n = 7/8$; P20–30, $n = 6/4$; P40, $n = 6/4$ animals, WT/Mut, 2-*way* ANOVA with Holm-Sidak *post hoc* tests; $^{***}P \leq 0.001$); all *P*-values are available online for this figure (Supplementary Table 3).

Figure 7 – Increased climbing fiber pause durations in *Slc1a3*$^{P290/+}$ Purkinje neurons. Current traces from cell-attached patch clamp recordings of Purkinje neuron somata (A) show representative simple spike activities of WT and *Slc1a3*$^{P290R/+}$ Purkinje neurons before and after glutamate puff application (arrow). Pooled burst plots with corresponding histograms (B) from individual responses of WT and *Slc1a3*$^{P290R/+}$ Purkinje neurons show substantial prolonged recovery periods (C) for Purkinje neurons from *Slc1a3*$^{P290R/+}$ mice. Burst plots (B) are constructed from glutamate puff responses of $n = 7/3$ Purkinje neurons (WT/Mut), and histograms are binned at 100 ms. Bar plot (C) shows recovery times as means ± *CI* from mean pause lengths values observed in $n = 10/3$ individual animals (WT/Mut, big circles, Mann-Whitney *U*-test) and pooled glutamate responses from all tested cells (small circles). Lengths of scale bars are indicated in the figure (A); $^{*}P \leq 0.05$, *P*–value is available online for this figure (Supplementary Table 3).

Figure 8 – Cerebellar degeneration in old *Slc1a3*$^{P290R/+}$ mice. Overall views of fixed brains (A) from adult WT or *Slc1a3*$^{P290R/+}$ mice (> P180) of both sexes on a grid surface (grid size: 0.25 mm^2) show degeneration of cerebella from transgenic animals. Bar graphs (B) show details of size decreases by comparing different cerebellar areas for male and female animals and stacked bars with summed areas of WT and *Slc1a3*$^{P290R/+}$ cerebella show overall cerebellar size decreases for both sexes. Sagittal views of Nissl-stained vermis region (C) from a male 2.5 year

old (P921) *Slc1a3*$^{P290R/+}$ mouse. Insets demonstrate the orientation of the slice and the vermis layer structures for WT and *Slc1a3*$^{P290R/+}$ mice. Quantification of mean sagittal size distributions (D) of vermal cerebellar layers in elderly WT and mutant mice (~P600-P950) of both sexes show that molecular layer and granule cell layer denote substantial mass decreases, but not white matter and stacked bars with summed areas of WT and *Slc1a3*$^{P290R/+}$ cerebella show overall sagittal cerebellar size decreases. Bar graphs in B and D denote mean area sizes ± *CI* and in stacked bars, sizes are presented as means ± *SEM*. Each mean was calculated from (n = 5♂5♀/5♂5♀, B) and $n = 4/4$ (D) animals (WT/Mut). Data of both sexes were separately analyzed with 2-*way* ANOVA and Holm-Sidak *post hoc* tests. Color coding of cerebellar areas / layers is indicated in the insets in C and D. Scale bar: 250 µm (C; $^{*}P \leq 0.05$, $^{**}P \leq 0.01$, $^{***}P \leq 0.001$; all P-values are available online for this figure (Supplementary Table 3). Abbreviations: H – hemisphere, V – vermis, GCL – granule cell layer, ML – molecular layer, WM – white matter.

REFERENCES

Abrahamsen B, Schneider N, Erichsen MN, Huynh TH, Fahlke C, Bunch L*, et al.* Allosteric modulation of an excitatory amino acid transporter: The subtype-selective inhibitor UCPH-101 exerts sustained inhibition of EAAT1 through an intramonomeric site in the trimerization domain. J Neurosci 2013; 33: 1068-87.

Adamczyk A, Gause CD, Sattler R, Vidensky S, Rothstein JD, Singer H*, et al.* Genetic and functional studies of a missense variant in a glutamate transporter, SLC1A3, in Tourette syndrome. Psychiat Genet 2011; 21: 90-7.

Alvina K, Khodakhah K. The therapeutic mode of action of 4-aminopyridine in cerebellar ataxia. J Neurosci 2010; 30: 7258-68.

Anderson MA, Ao Y, Sofroniew MV. Heterogeneity of reactive astrocytes. Neurosci Lett 2014; 565: 23-9.

Arancillo M, White JJ, Lin T, Stay TL, Sillitoe RV. *In vivo* analysis of Purkinje cell firing properties during postnatal mouse development. J Neurophysiol 2015; 113: 578-91.

Bell CC, Grimm RJ. Discharge properties of Purkinje cells recorded on single and double microelectrodes. J Neurophysiol 1969; 32: 1044-55.

Browne DL, Litt M. Dinucleotide repeat polymorphisms near the *KCNA6* and *KCNA1* loci. Hum Mol Genet 1994; 3: 842.

Cader MZ, Steckley JL, Dyment DA, McLachlan RS, Ebers GC. A genome-wide screen and linkage mapping for a large pedigree with episodic ataxia. Neurology 2005; 65: 156-8.

Chaudhry FA, Lehre KP, van Lookeren Campagne M, Ottersen OP, Danbolt NC, Storm-Mathisen J. Glutamate transporters in glial plasma membranes: highly differentiated localizations revealed by quantitative ultrastructural immunocytochemistry. Neuron 1995; 15: 711-20.

Cheron G, Sausbier M, Sausbier U, Neuhuber W, Ruth P, Dan B, *et al.* BK channels control cerebellar Purkinje and Golgi cell rhythmicity *in vivo*. PloS One 2009; 4: e7991.

Choi KD, Jen JC, Choi SY, Shin JH, Kim HS, Kim HJ*, et al.* Late-onset episodic ataxia associated with *SLC1A3* mutation. J Hum Genet 2017a; 62: 443-6.

Choi KD, Kim JS, Kim HJ, Jung I, Jeong SH, Lee SH*, et al.* Genetic variants associated with episodic ataxia in Korea. Sci Rep 2017b; 7: 13855.

Conroy J, McGettigan P, Murphy R, Webb D, Murphy SM, McCoy B*, et al.* A novel locus for episodic ataxia:*UBR4* the likely candidate. Eur J Hum Genet 2014; 22: 505-10.

Crepel F. Regression of functional synapses in the immature mammalian cerebellum. Trends Neurosci 1982; 5 (Supplement C): 266-9.

Damji KF, Allingham RR, Pollock SC, Small K, Lewis KE, Stajich JM*, et al.* Periodic vestibulocerebellar ataxia, an autosomal dominant ataxia with defective smooth pursuit, is genetically distinct from other autosomal dominant ataxias. Arch Neurol 1996; 53: 338-44.

de Vries B, Mamsa H, Stam AH, Wan J, Bakker SL, Vanmolkot KR*, et al.* Episodic ataxia associated with EAAT1 mutation C186S affecting glutamate reuptake. Arch Neurol 2009; 66: 97-101.

Donato R, Page KM, Koch D, Nieto-Rostro M, Foucault I, Davies A*, et al.* The ducky^{2J} mutation in *Cacna2d2* results in reduced spontaneous Purkinje cell activity and altered gene expression. J Neurosci 2006; 26: 12576-86.

Droste D, Seifert G, Seddar L, Jadtke O, Steinhauser C, Lohr C. Ca^{2+}-permeable AMPA receptors in mouse olfactory bulb astrocytes. Sci Rep 2017; 7: 44817.

Eccles JC, Llinas R, Sasaki K. The excitatory synaptic action of climbing fibres on the Purkinje cells of the cerebellum. J Physiol 1966; 182: 268-96.

Ernest NJ, Habela CW, Sontheimer H. Cytoplasmic condensation is both necessary and sufficient to induce apoptotic cell death. J Cell Sci 2008; 121: 290-7.

Fahlke C, Kortzak D, Machtens JP. Molecular physiology of EAAT anion channels. Pflug Arch: Eur J Physiol 2016; 468: 491-502.

Feng L, Hatten ME, Heintz N. Brain lipid-binding protein (BLBP): a novel signaling system in the developing mammalian CNS. Neuron 1994; 12: 895-908.

Friis MB, Friborg CR, Schneider L, Nielsen MB, Lambert IH, Christensen ST*, et al.* Cell shrinkage as a signal to apoptosis in NIH 3T3 fibroblasts. J Physiol 2005; 567: 427-43.

Gao Z, Todorov B, Barrett CF, van Dorp S, Ferrari MD, van den Maagdenberg AM*, et al.* Cerebellar ataxia by enhanced $Ca_V2.1$ currents is alleviated by Ca^{2+}-dependent K^+-channel activators in *Cacna1a* (S218L) mutant mice. J Neurosci 2012; 32: 15533-46.

Gavrieli Y, Sherman Y, Ben-Sasson SA. Identification of programmed cell death *in situ* via specific labeling of nuclear DNA fragmentation. J Cell Biol 1992; 119: 493-501.

Gensch T, Untiet V, Franzen A, Kovermann P, Fahlke C. Determination of intracellular chloride concentrations by fluorescence lifetime imaging. Springer Series Chem: Springer Verlag 2015; p. 189-211.

Grosche J, Matyash V, Moller T, Verkhratsky A, Reichenbach A, Kettenmann H. Microdomains for neuron-glia interaction: parallel fiber signaling to Bergmann glial cells. Nat Neurosci 1999; 2: 139-43.

Guyenet SJ, Furrer SA, Damian VM, Baughan TD, La Spada AR, Garden GA. A simple composite phenotype scoring system for evaluating mouse models of cerebellar ataxia. J Vis Exp 2010; 39: 1787.

Hansen ST, Meera P, Otis TS, Pulst SM. Changes in Purkinje cell firing and gene expression precede behavioral pathology in a mouse model of SCA2. Hum Mol Genet 2013; 22: 271-83.

Hatten ME, Liem RK, Mason CA. Two forms of cerebellar glial cells interact differently with neurons *in vitro*. J Cell Biol 1984; 98: 193-204.

Hausser M, Clark BA. Tonic synaptic inhibition modulates neuronal output pattern and spatiotemporal synaptic integration. Neuron 1997; 19: 665-78.

Hoebeek FE, Stahl JS, van Alphen AM, Schonewille M, Luo C, Rutteman M*, et al.* Increased noise level of Purkinje cell activities minimizes impact of their modulation during sensorimotor control. Neuron 2005; 45: 953-65.

Holt GR, Softky WR, Koch C, Douglas RJ. Comparison of discharge variability *in vitro* and *in vivo* in cat visual cortex neurons. J Neurophysiol 1996; 75: 1806-14.

Hotzy J, Schneider N, Kovermann P, Fahlke C. Mutating a conserved proline residue within the trimerization domain modifies Na^+ binding to excitatory amino acid transporters and associated conformational changes. J Biol Chem 2013; 288: 36492-501.

Iino M, Goto K, Kakegawa W, Okado H, Sudo M, Ishiuchi S*, et al.* Glia-synapse interaction through Ca^{2+}-permeable AMPA receptors in Bergmann glia. Science 2001; 292: 926-9.

Iwama K, Iwata A, Shiina M, Mitsuhashi S, Miyatake S, Takata A*, et al.* A novel mutation in *SLC1A3* causes episodic ataxia. J Hum Genet 2018; 63: 207-11.

Jayabal S, Chang HH, Cullen KE, Watt AJ. 4-aminopyridine reverses ataxia and cerebellar firing deficiency in a mouse model of spinocerebellar ataxia type 6. Sci Rep 2016; 6: 29489.

Jayabal S, Ljungberg L, Watt AJ. Transient cerebellar alterations during development prior to obvious motor phenotype in a mouse model of spinocerebellar ataxia type 6. J Physiol 2017; 595: 949-66.

Jen JC, Graves TD, Hess EJ, Hanna MG, Griggs RC, Baloh RW. Primary episodic ataxias: diagnosis, pathogenesis and treatment. Brain 2007; 130: 2484-93.

Jen JC, Wan J, Palos TP, Howard BD, Baloh RW. Mutation in the glutamate transporter EAAT1 causes episodic ataxia, hemiplegia, and seizures. Neurology 2005; 65: 529-34.

Jones BJ, Roberts, D. J. The quantitative measurement of motor inco-ordination in naive mice using an accelerating rotarod. J Pharm Pharmacol 1968; 20: 302-4.

Kaplan EL, Meier, P. Nonparametric estimation from incomplete observations. J Am Ass 1958; 53: 34.

Keinanen K, Wisden W, Sommer B, Werner P, Herb A, Verdoorn TA, *et al.* A family of AMPA-selective glutamate receptors. Science 1990; 249: 556-60.

Kerber KA, Jen JC, Lee H, Nelson SF, Baloh RW. A new episodic ataxia syndrome with linkage to chromosome 19q13. Arch Neurol 2007; 64: 749-52.

Kovermann P, Hessel M, Kortzak D, Jen JC, Koch J, Fahlke C, *et al.* Impaired K^+ binding to glial glutamate transporter EAAT1 in migraine. Sci Rep 2017; 7: 13913.

Latham A, Paul DH. Spontaneous activity of cerebellar Purkinje cells and their responses to impulses in climbing fibres. J Physiol 1971; 213: 135-56.

Lordkipanidze T, Dunaevsky A. Purkinje cell dendrites grow in alignment with Bergmann glia. Glia 2005; 51: 229-34.

Machtens JP, Kortzak D, Lansche C, Leinenweber A, Kilian P, Begemann B, *et al.* Mechanisms of anion conduction by coupled glutamate transporters. Cell 2015; 160: 542-53.

Mariani J. Extent of multiple innervation of Purkinje cells by climbing fibers in the olivocerebellar system of *weaver*, *reeler*, and *staggerer* mutant mice. J Neurobiol 1982; 13: 119-26.

Marr D. A theory of cerebellar cortex. J Physiol 1969; 202: 437-70.

McGrath JC, Drummond GB, McLachlan EM, Kilkenny C, Wainwright CL. Guidelines for reporting experiments involving animals: the ARRIVE guidelines. Brit J Pharmacol 2010; 160: 1573-6.

McKay BE, Turner RW. Physiological and morphological development of the rat cerebellar Purkinje cell. J Physiol 2005; 567: 829-50.

Midtgaard J. Stellate cell inhibition of Purkinje cells in the turtle cerebellum *in vitro*. J Physiol 1992; 457: 355-67.

Miyazaki T, Fukaya M, Shimizu H, Watanabe M. Subtype switching of vesicular glutamate transporters at parallel fibre-Purkinje cell synapses in developing mouse cerebellum. Eur J Neurosci 2003; 17: 2563-72.

Mullen RJ, Buck CR, Smith AM. NeuN, a neuronal specific nuclear protein in vertebrates. Development 1992; 116: 201-11.

Oomman S, Finckbone V, Dertien J, Attridge J, Henne W, Medina M, *et al.* Active caspase-3 expression during postnatal development of rat cerebellum is not systematically or consistently associated with apoptosis. J Comp Neurol 2004; 476: 154-73.

Oomman S, Strahlendorf H, Finckbone V, Strahlendorf J. Non-lethal active caspase-3 expression in Bergmann glia of postnatal rat cerebellum. Brain Res Dev Brain Res 2005; 160: 130-45.

Ophoff RA, Terwindt GM, Vergouwe MN, van Eijk R, Oefner PJ, Hoffman SM, *et al.* Familial hemiplegic migraine and episodic ataxia type-2 are caused by mutations in the Ca^{2+} channel gene *CACNL1A4*. Cell 1996; 87(3): 543-52.

Otis TS, Mathews PJ, Lee KH, Maiz J. How do climbing fibers teach? Front Neural Circuits 2012; 6: 95.

Palay SLC-P, V. Cerebellar cortex. Berlin, Heidelberg: Springer; 1974.

Parinejad N, Peco E, Ferreira T, Stacey SM, van Meyel DJ. Disruption of an EAAT-mediated chloride channel in a *Drosophila* model of ataxia. J Neurosci 2016; 36: 7640-7.

Perkins EM, Suminaite D, Clarkson YL, Lee SK, Lyndon AR, Rothstein JD*, et al.* Posterior cerebellar Purkinje cells in an SCA5/SPARCA1 mouse model are especially vulnerable to the synergistic effect of loss of beta-III spectrin and GLAST. Hum Mol Genet 2016; 25: 4448-61.

Porcelli AM, Ghelli A, Zanna C, Valente P, Ferroni S, Rugolo M. Apoptosis induced by staurosporine in ECV304 cells requires cell shrinkage and upregulation of Cl^- conductance. Cell Death Differ 2004; 11: 655-62.

Pyle A, Smertenko T, Bargiela D, Griffin H, Duff J, Appleton M*, et al.* Exome sequencing in undiagnosed inherited and sporadic ataxias. Brain 2015; 138: 276-83.

Rakic P. Neuron-glia relationship during granule cell migration in developing cerebellar cortex. A Golgi and electronmicroscopic study in *Macacus Rhesus*. J Comp Neurol 1971; 141: 283-312.

Rothstein JD, Martin L, Levey AI, Dykes-Hoberg M, Jin L, Wu D*, et al.* Localization of neuronal and glial glutamate transporters. Neuron 1994; 13: 713-25.

Sato Y, Miura A, Fushiki H, Kawasaki T. Short-term modulation of cerebellar Purkinje cell activity after spontaneous climbing fiber input. J Neurophysiol 1992; 68: 2051-62.

Schreiner AE, Durry S, Aida T, Stock MC, Ruther U, Tanaka K*, et al.* Laminar and subcellular heterogeneity of GLAST and GLT-1 immunoreactivity in the developing postnatal mouse hippocampus. J Comp Neurol 2014; 522: 204-24.

Sofroniew MV. Reactive astrocytes in neural repair and protection. Neuroscientist 2005; 11: 400-7.

Storck T, Schulte S, Hofmann K, Stoffel W. Structure, expression, and functional analysis of a Na^+-dependent glutamate/aspartate transporter from rat brain. Proc Natl Acad Sci USA 1992; 89: 10955-9.

Tang T, Xiao J, Suh CY, Burroughs A, Cerminara NL, Jia L*, et al.* Heterogeneity of Purkinje cell simple spike-complex spike interactions: zebrin- and non-zebrin-related variations. J Physiol 2017; 595: 5341-57.

Torp R, Danbolt NC, Babaie E, Bjoras M, Seeberg E, Storm-Mathisen J*, et al.* Differential expression of two glial glutamate transporters in the rat brain: an *in situ* hybridization study. Eur J Neurosci 1994; 6: 936-42.

Untiet V, Kovermann P, Gerkau NJ, Gensch T, Rose CR, Fahlke C. Glutamate transporter-associated anion channels adjust intracellular chloride concentrations during glial maturation. Glia 2017; 65: 388-400.

van Amen-Hellebrekers CJ, Jansen S, Pfundt R, Schuurs-Hoeijmakers JH, Koolen DA, Marcelis CL*, et al.* Duplications of *SLC1A3*: Associated with ADHD and autism. Eur J Med Genet 2016; 59: 373-6.

Verkman AS. Development and biological applications of chloride-sensitive fluorescent indicators. Am J Physiol 1990; 259: C375-88.

Wadiche JI, Amara SG, Kavanaugh MP. Ion fluxes associated with excitatory amino acid transport. Neuron 1995; 15: 721-8.

Wadiche JI, Jahr CE. Multivesicular release at climbing fiber-Purkinje cell synapses. Neuron 2001; 32: 301-13.

Walev I, Reske K, Palmer M, Valeva A, Bhakdi S. Potassium-inhibited processing of IL-1 beta in human monocytes. EMBO J 1995; 14: 1607-14.

Walter JT, Alvina K, Womack MD, Chevez C, Khodakhah K. Decreases in the precision of Purkinje cell pacemaking cause cerebellar dysfunction and ataxia. Nat Neurosci 2006; 9: 389-97.

Watanabe M, Kano M. Climbing fiber synapse elimination in cerebellar Purkinje cells. Eur J Neurosci 2011; 34: 1697-710.

Watase K, Hashimoto K, Kano M, Yamada K, Watanabe M, Inoue Y*, et al.* Motor discoordination and increased susceptibility to cerebellar injury in GLAST mutant mice. Eur J Neurosci 1998; 10: 976-88.

Weyer A, Schilling K. Developmental and cell type-specific expression of the neuronal marker NeuN in the murine cerebellum. J Neurosci Res 2003; 73: 400-9.

Winter N, Kovermann P, Fahlke C. A point mutation associated with episodic ataxia 6 increases glutamate transporter anion currents. Brain 2012; 135: 3416-25.

Womack M, Khodakhah K. Active contribution of dendrites to the tonic and trimodal patterns of activity in cerebellar Purkinje neurons. J Neurosci 2002; 22: 10603-12.

Woodward DJ, Hoffer BJ, Altman J. Physiological and pharmacological properties of Purkinje cells in rat cerebellum degranulated by postnatal x-irradiation. J Neurobiol 1974; 5: 283-304.

Wulff P, Schonewille M, Renzi M, Viltono L, Sassoe-Pognetto M, Badura A*, et al.* Synaptic inhibition of Purkinje cells mediates consolidation of vestibulo-cerebellar motor learning. Nat Neurosci 2009; 12: 1042-9.

Yamada K, Fukaya M, Shibata T, Kurihara H, Tanaka K, Inoue Y*, et al.* Dynamic transformation of Bergmann glial fibers proceeds in correlation with dendritic outgrowth and synapse formation of cerebellar Purkinje cells. J Comp Neurol 2000; 418: 106-20.

Yu FH, Mantegazza M, Westenbroek RE, Robbins CA, Kalume F, Burton KA*, et al.* Reduced sodium current in GABAergic interneurons in a mouse model of severe myoclonic epilepsy in infancy. Nat Neurosci 2006; 9: 1142-9.

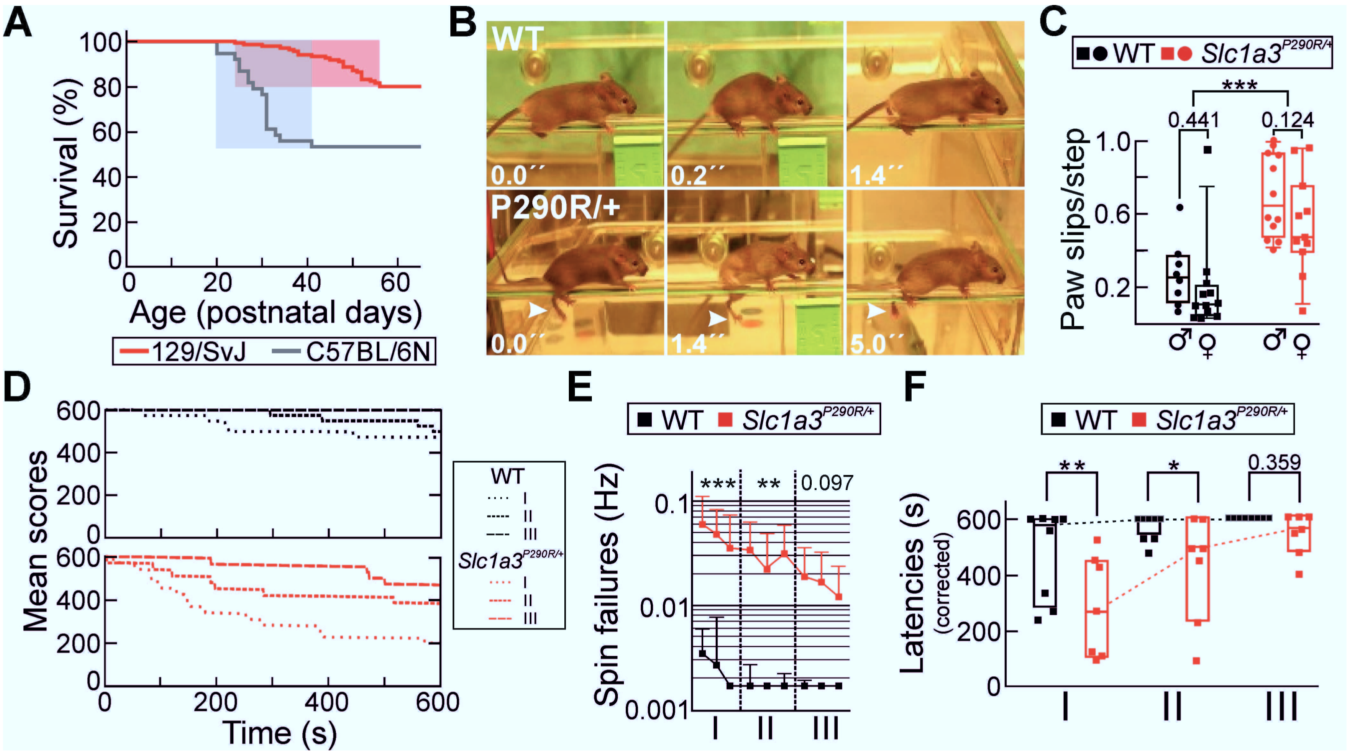
A
Survival (%)
100
80
60
40
20
0
0
20
40
60
Age (postnatal days)
129/SvJ
C57BL/6N
B
WT
0.0´´
0.2´´
1.4´´
P290R/+
0.0´´
1.4´´
5.0´´
C
WT
Slc1a3^P290R/+
***
0.441
0.124
Paw slips/step
1.0
0.6
0.2
♂ ♀
♂ ♀
D
Mean scores
600
400
200
0
600
400
200
0
0
200
400
600
Time (s)
WT
I
II
III
Slc1a3^P290R/+
I
II
III
E
WT
Slc1a3^P290R/+
Spin failures (Hz)
***
**
0.097
0.1
0.01
0.001
I
II
III
F
WT
Slc1a3^P290R/+
**
*
0.359
Latencies (s)
(corrected)
600
400
200
0
I
II
III

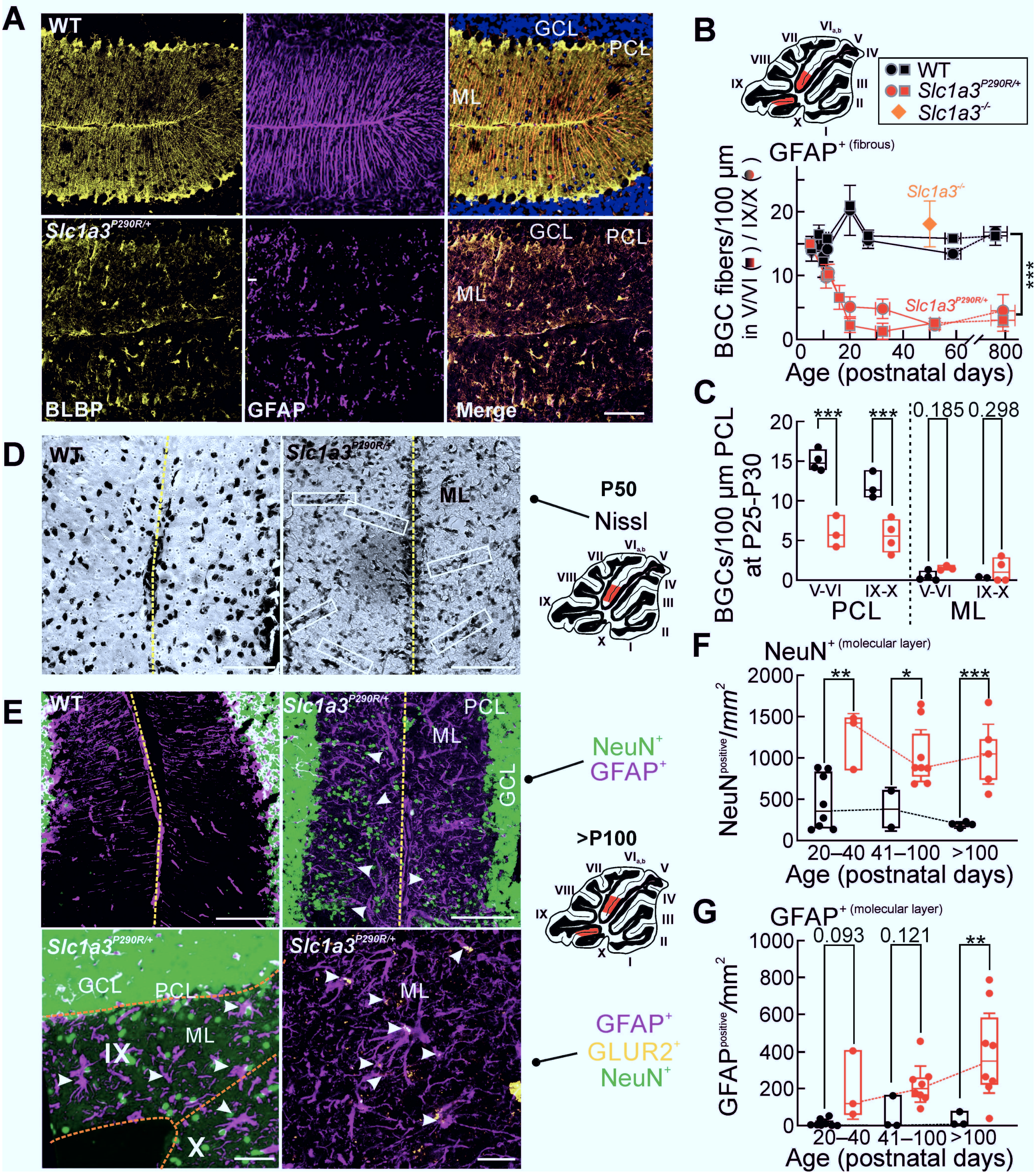
A
WT
GCL
PCL
ML
Slc1a3^P290R/+
GCL
PCL
ML
BLBP
GFAP
Merge
B
VI a,b
VII
V
VIII
IV
IX
III
II
X
I
WT
Slc1a3^P290R/+
Slc1a3^-/-
GFAP+ (fibrous)
BGC fibers/100 µm in V/VI ( ) / IX/X ( )
Slc1a3^-/-
Slc1a3^P290R/+
***
0
10
20
0
20
40
60
800
Age (postnatal days)
C
BGCs/100 µm PCL at P25-P30
***
***
0.185
0.298
0
5
10
15
20
V-VI
IX-X
V-VI
IX-X
PCL
ML
D
WT
Slc1a3^P290R/+
ML
P50
Nissl
E
WT
Slc1a3^P290R/+
PCL
ML
GCL
NeuN+
GFAP+
>P100
Slc1a3^P290R/+
GCL
PCL
ML
IX
X
Slc1a3^P290R/+
ML
GFAP+
GLUR2+
NeuN+
F
NeuN+ (molecular layer)
NeuN^positive/mm^2
**
*
***
0
500
1000
1500
2000
20–40
41–100
>100
Age (postnatal days)
G
GFAP+ (molecular layer)
GFAP^positive/mm^2
0.093
0.121
**
0
200
400
600
800
1000
20–40
41–100
>100
Age (postnatal days)

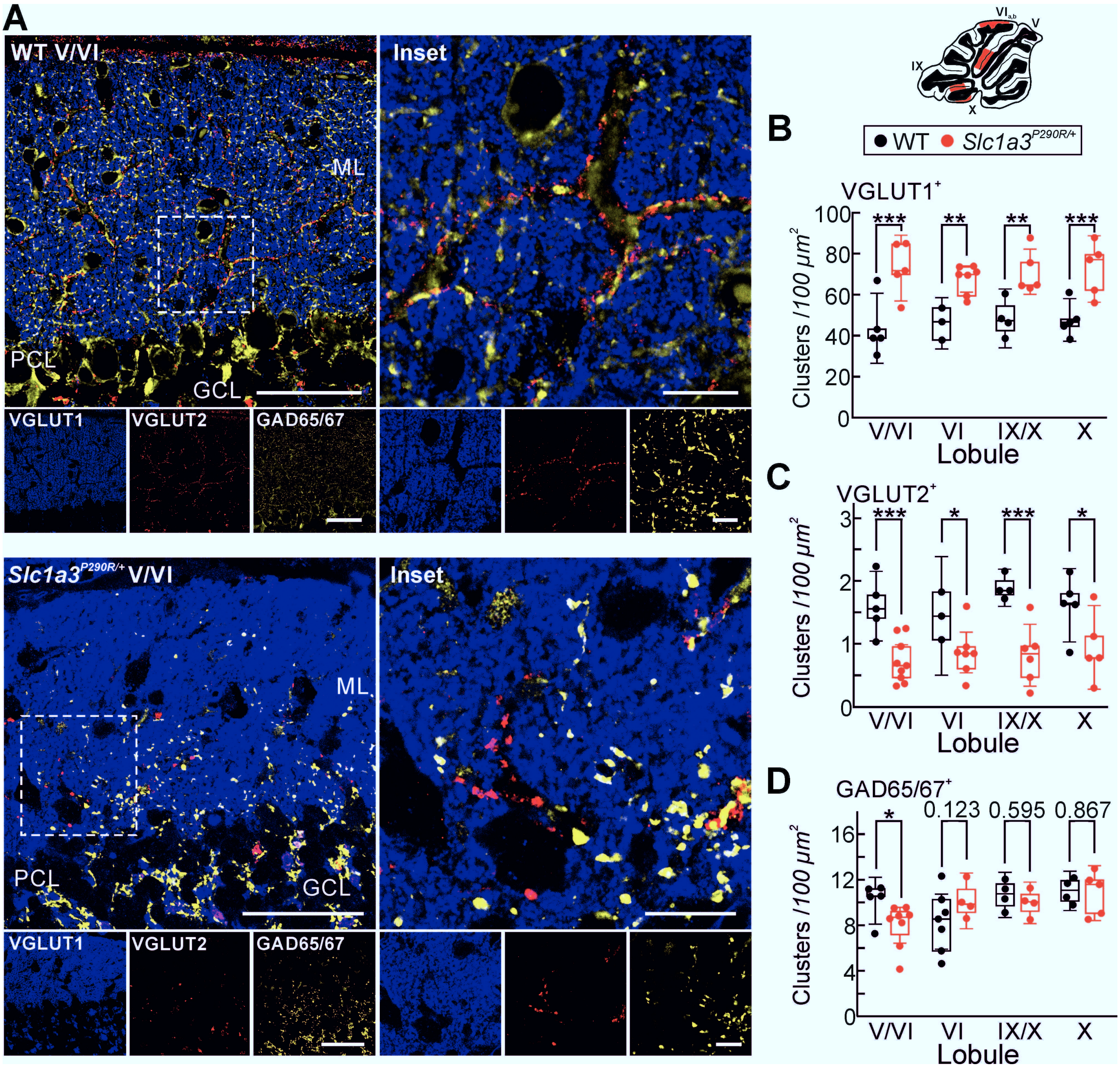
A
WT V/VI
Inset
ML
PCL
GCL
VGLUT1
VGLUT2
GAD65/67
Slc1a3^P290R/+ V/VI
Inset
ML
PCL
GCL
VGLUT1
VGLUT2
GAD65/67
VI a,b
V
IX
X
B
● WT ● Slc1a3^P290R/+
VGLUT1+
100
80
60
40
20
0
*** ** ** ***
Clusters /100 µm²
V/VI VI IX/X X
Lobule
C
VGLUT2+
3
2
1
0
*** * *** *
Clusters /100 µm²
V/VI VI IX/X X
Lobule
D
GAD65/67+
16
12
8
4
0
* 0.123 0.595 0.867
Clusters /100 µm²
V/VI VI IX/X X
Lobule

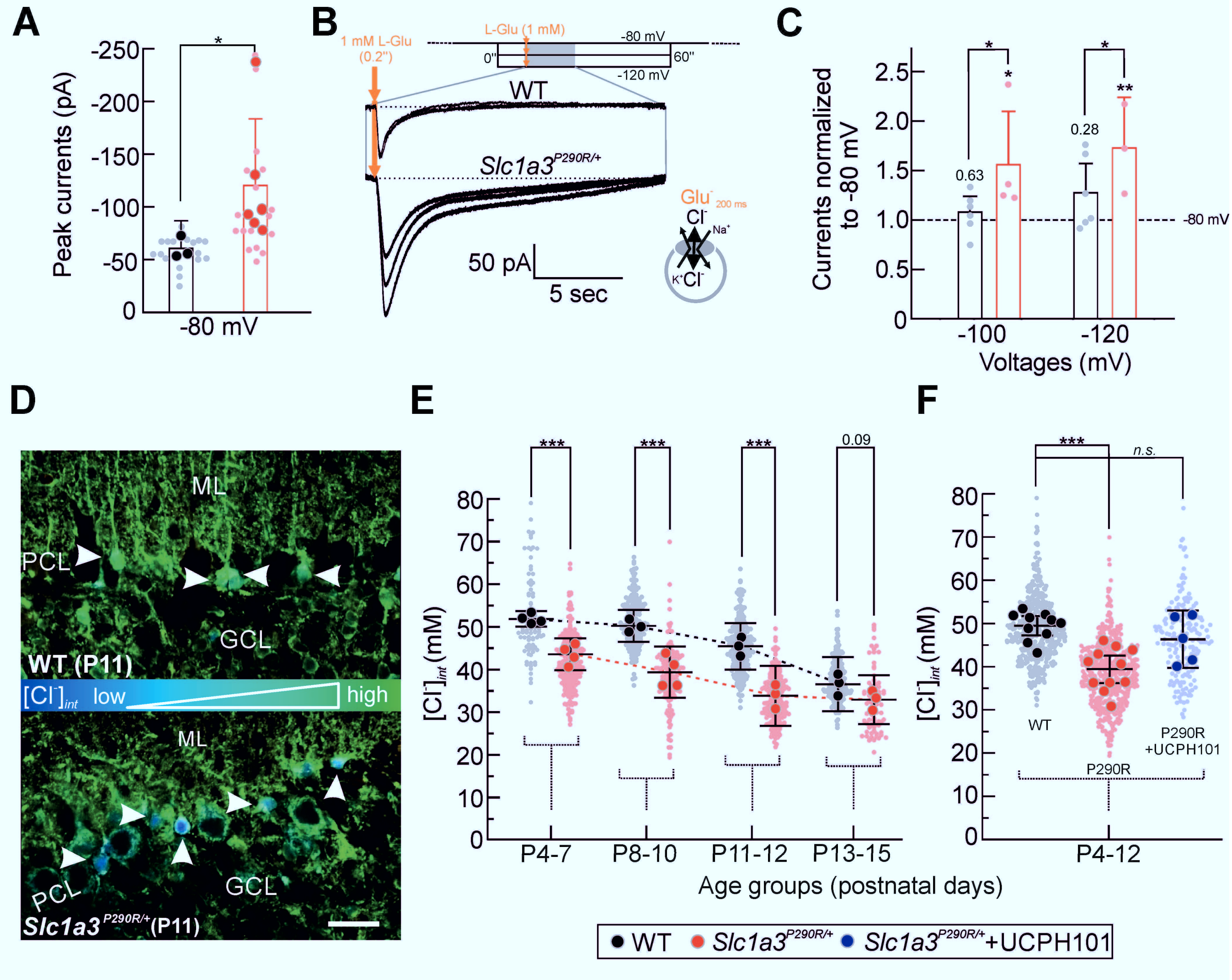
A
Peak currents (pA)
-250
-200
-150
-100
-50
0
*
-80 mV
B
1 mM L-Glu
(0.2")
L-Glu (1 mM)
-80 mV
0"
60"
-120 mV
WT
Slc1a3^P290R/+
50 pA
5 sec
Glu⁻ 200 ms
Cl⁻
Na⁺
K⁺Cl⁻
C
Currents normalized to -80 mV
2.5
2.0
1.5
1.0
0.5
0
*
*
*
**
0.63
0.28
-80 mV
-100
-120
Voltages (mV)
D
ML
PCL
GCL
WT (P11)
[Cl⁻]int low
high
ML
PCL
GCL
Slc1a3^P290R/+(P11)
E
***
***
***
0.09
[Cl⁻]int (mM)
80
70
60
50
40
30
20
10
0
P4-7
P8-10
P11-12
P13-15
Age groups (postnatal days)
F
***
n.s.
[Cl⁻]int (mM)
80
70
60
50
40
30
20
10
0
WT
P290R
P290R
+UCPH101
P4-12
● WT ● Slc1a3^P290R/+ ● Slc1a3^P290R/+ +UCPH101

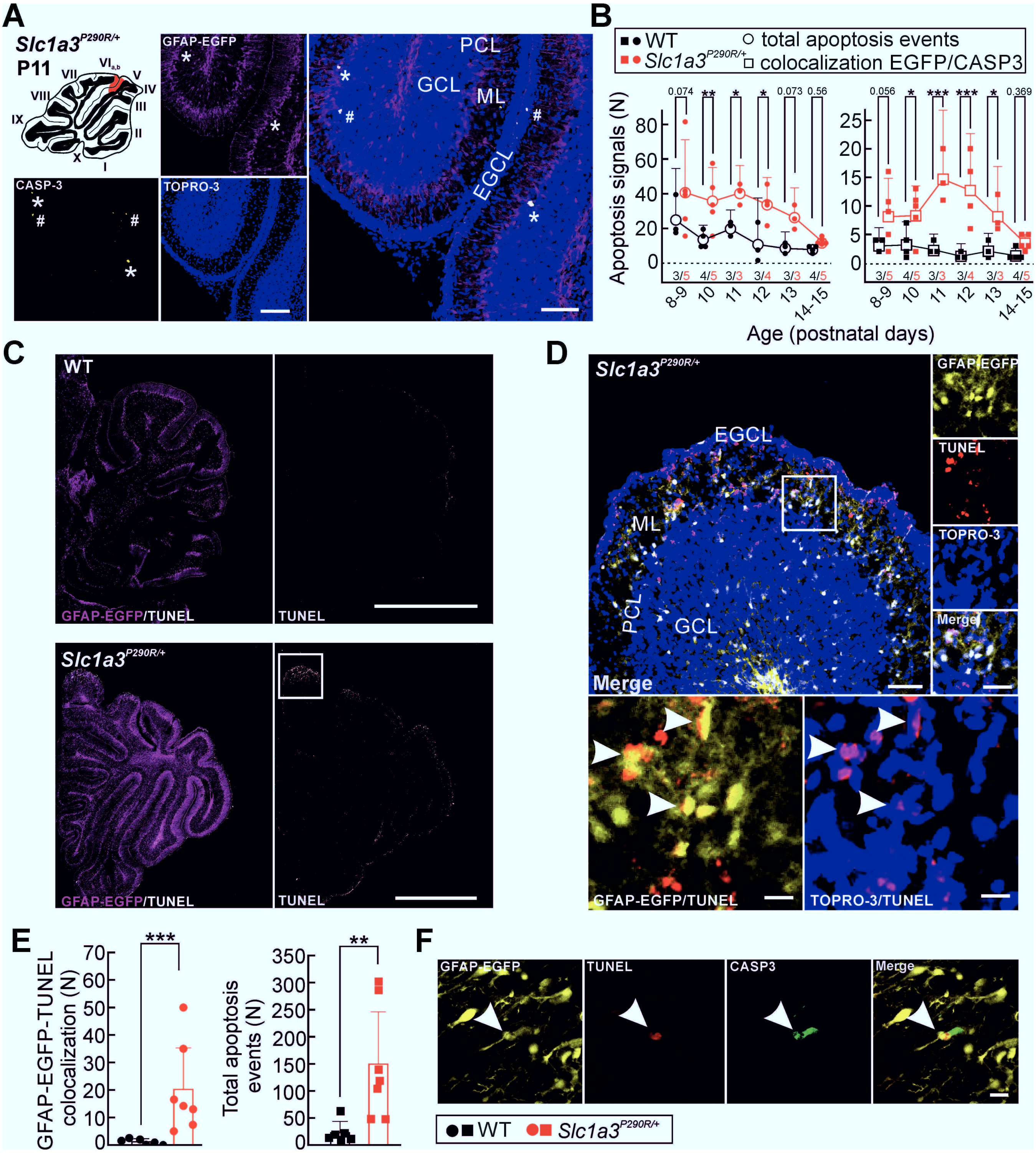
A
Slc1a3$^{P290R/+}$
P11
VII
VI$_{a,b}$
V
IV
III
II
I
VIII
IX
X
GFAP-EGFP
CASP-3
TOPRO-3
*
#
PCL
GCL
ML
EGCL
B
■● WT
■● Slc1a3$^{P290R/+}$
○ total apoptosis events
□ colocalization EGFP/CASP3
Apoptosis signals (N)
0.074
**
*
*
0.073
0.56
0.056
*
***
***
*
0.369
80
60
40
20
0
25
20
15
10
5
0
3/5
4/5
3/3
3/4
3/3
4/5
8-9
10
11
12
13
14-15
Age (postnatal days)
C
WT
GFAP-EGFP/TUNEL
TUNEL
Slc1a3$^{P290R/+}$
D
Slc1a3$^{P290R/+}$
EGCL
ML
PCL
GCL
Merge
GFAP-EGFP
TUNEL
TOPRO-3
Merge
GFAP-EGFP/TUNEL
TOPRO-3/TUNEL
E
***
GFAP-EGFP-TUNEL colocalization (N)
70
60
50
40
30
20
10
0
**
Total apoptosis events (N)
350
300
250
200
150
100
50
0
F
GFAP-EGFP
TUNEL
CASP3
Merge
●■ WT ●■ Slc1a3$^{P290R/+}$

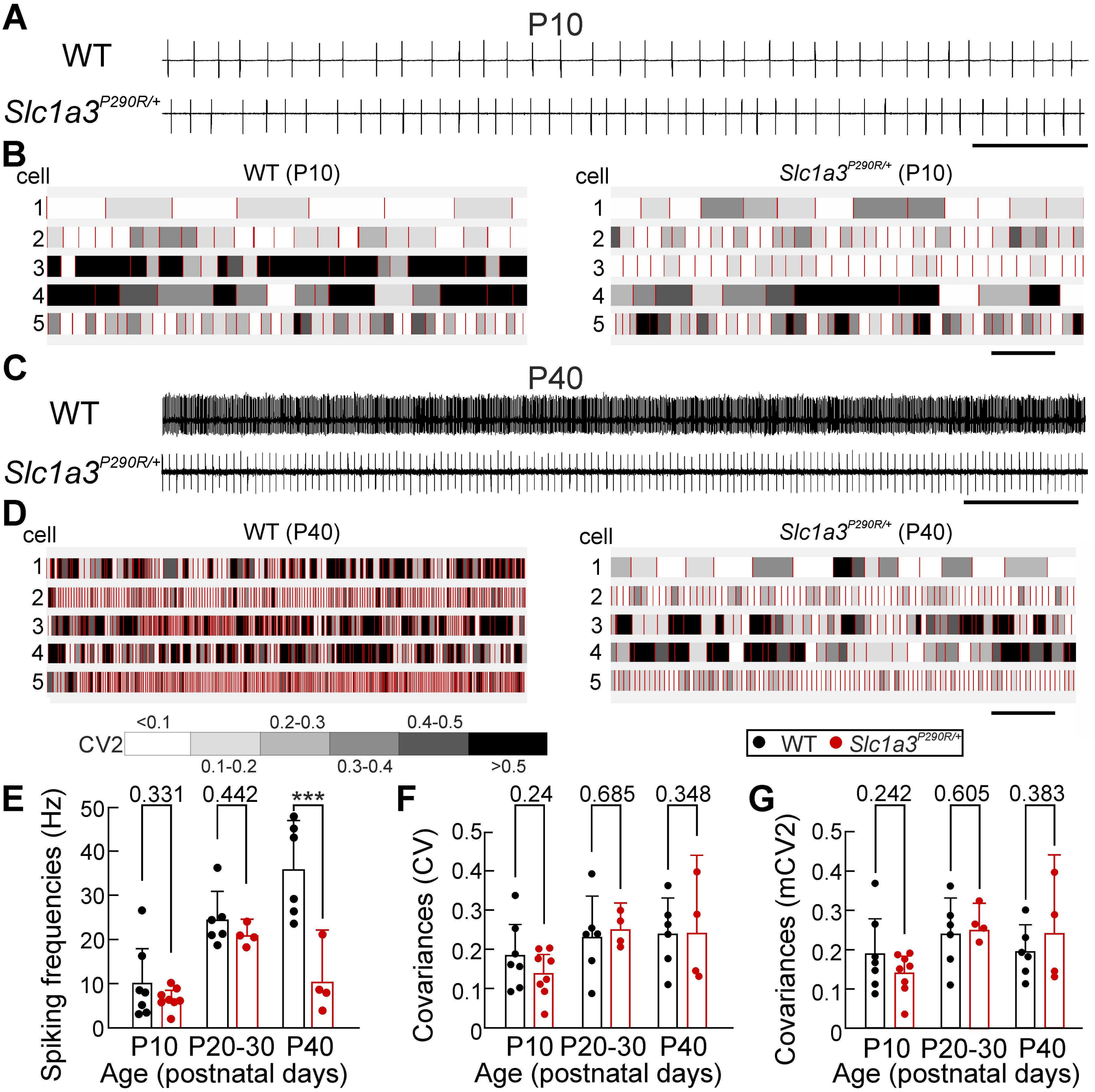
A
P10
WT
Slc1a3P290R/+
B
cell
WT (P10)
Slc1a3P290R/+ (P10)
1
2
3
4
5
C
P40
WT
Slc1a3P290R/+
D
cell
WT (P40)
Slc1a3P290R/+ (P40)
CV2
<0.1
0.1-0.2
0.2-0.3
0.3-0.4
0.4-0.5
>0.5
● WT ● Slc1a3P290R/+
E
Spiking frequencies (Hz)
0.331
0.442
***
0
10
20
30
40
50
P10 P20-30 P40
Age (postnatal days)
F
Covariances (CV)
0.24
0.685
0.348
0
0.1
0.2
0.3
0.4
0.5
P10 P20-30 P40
Age (postnatal days)
G
Covariances (mCV2)
0.242
0.605
0.383
0
0.1
0.2
0.3
0.4
0.5
P10 P20-30 P40
Age (postnatal days)

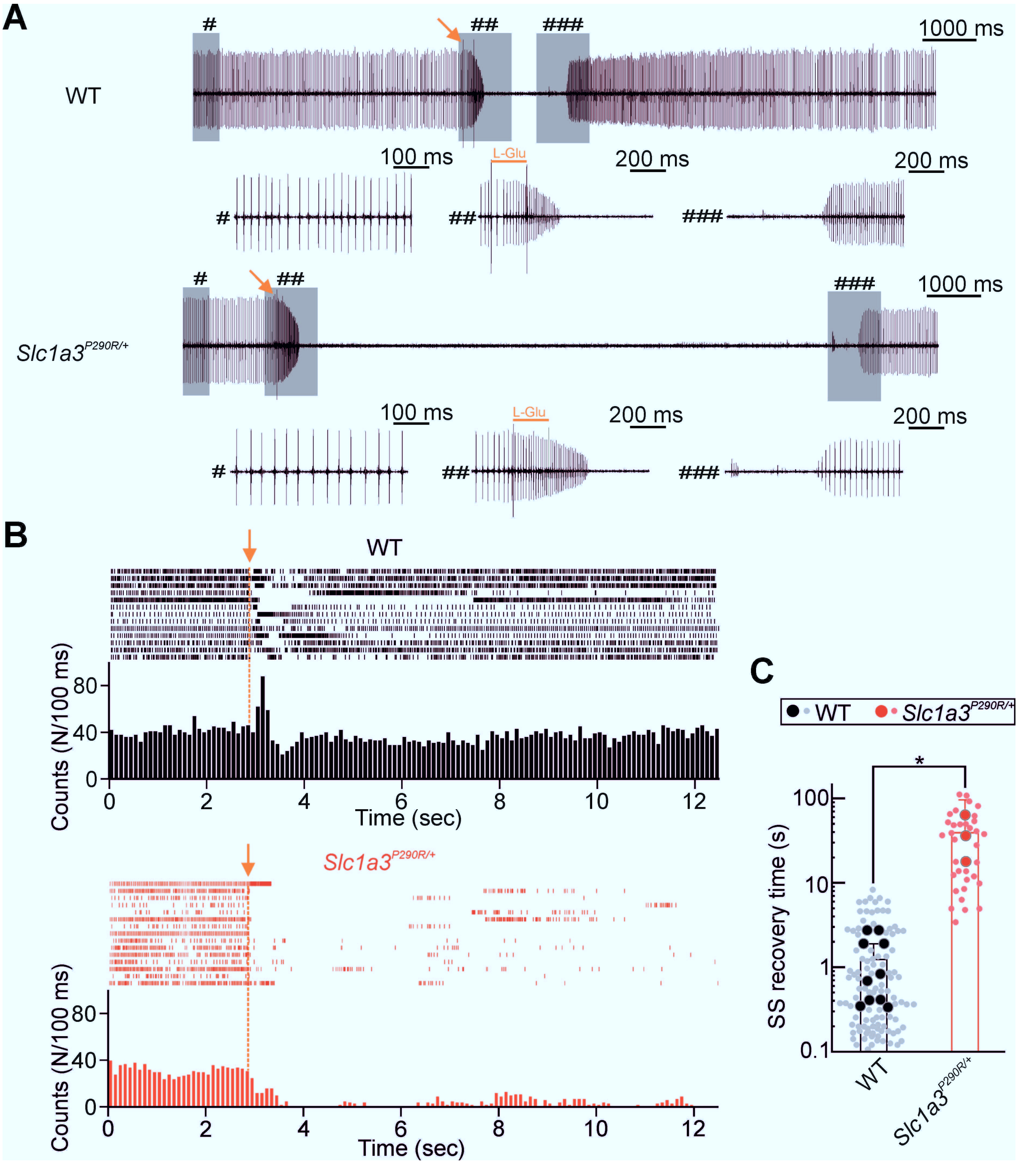
A
WT
#
##
###
1000 ms
100 ms
L-Glu
200 ms
200 ms
#
##
###
Slc1a3^P290R/+
#
##
###
1000 ms
100 ms
L-Glu
200 ms
200 ms
#
##
###
B
WT
Counts (N/100 ms)
80
40
0
0
2
4
6
8
10
12
Time (sec)
Slc1a3^P290R/+
Counts (N/100 ms)
80
40
0
0
2
4
6
8
10
12
Time (sec)
C
● WT
● Slc1a3^P290R/+
*
SS recovery time (s)
100
10
1
0.1
WT
Slc1a3^P290R/+

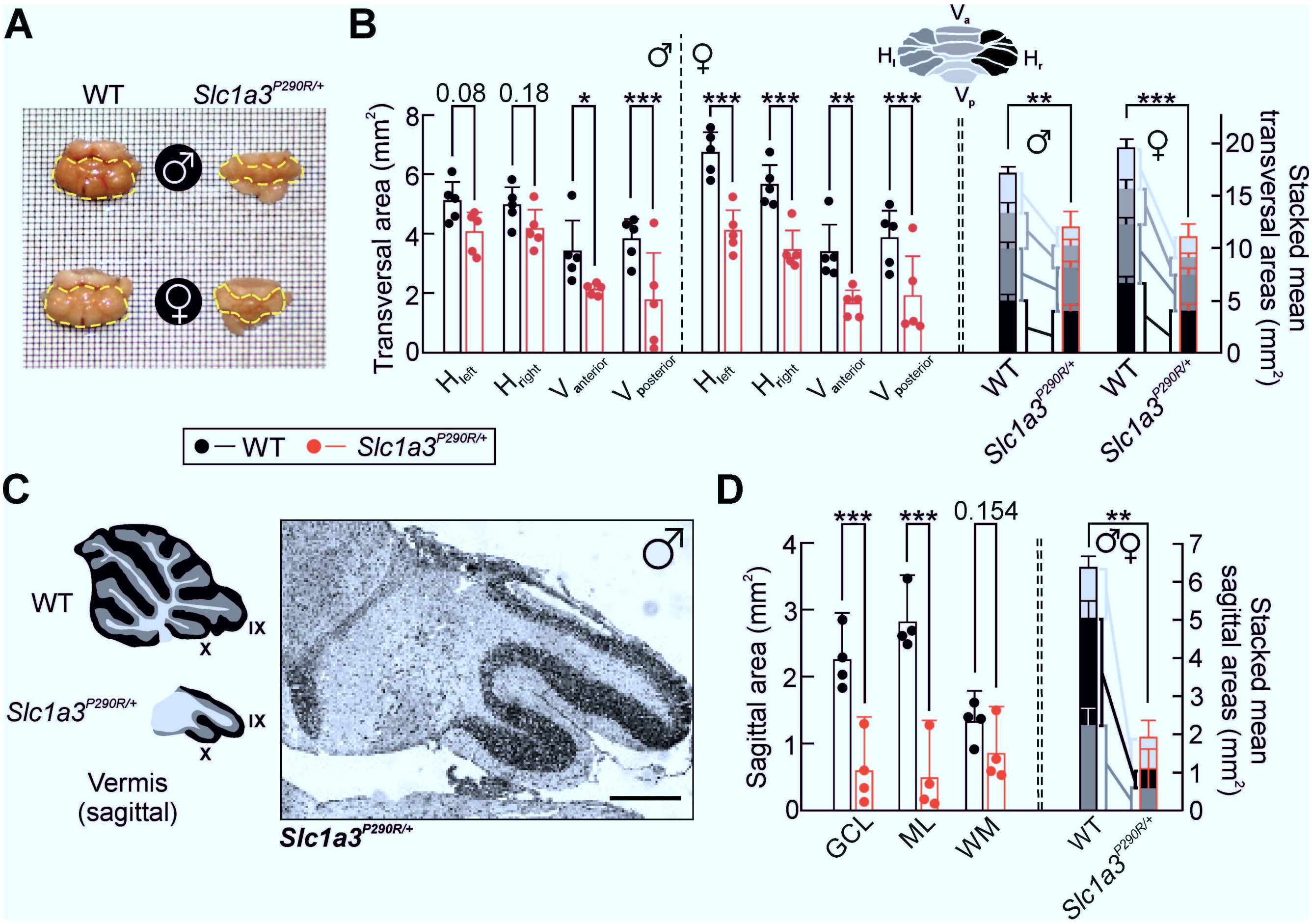
A
WT
Slc1a3P290R/+
♂
♀
B
♂
♀
Va
Hl
Hr
Vp
Transversal area (mm2)
0
2
4
6
8
0.08
0.18
*
***
***
***
**
***
**
***
Hleft
Hright
V anterior
V posterior
Hleft
Hright
V anterior
V posterior
WT
Slc1a3P290R/+
WT
Slc1a3P290R/+
Stacked mean transversal areas (mm2)
0
5
10
15
20
WT
Slc1a3P290R/+
C
WT
IX
X
Slc1a3P290R/+
IX
X
Vermis (sagittal)
♂
Slc1a3P290R/+
D
Sagittal area (mm2)
0
1
2
3
4
***
***
0.154
GCL
ML
WM
**
♂♀
WT
Slc1a3P290R/+
Stacked mean sagittal areas (mm2)
0
1
2
3
4
5
6
7

Supplementary Figures
for
Increased glutamate transporter-associated anion currents cause glial apoptosis in episodic ataxia 6

Peter Kovermann[1], Verena Untiet[3], Yulia Kolobkova[1], Miriam Engels[1],Stephan Baader[2], Karl Schilling[2], and Christoph Fahlke[1]

[1]Institut für Biologische Informationsprozesse, Molekular- und Zellphysiologie (IBI-1), Forschungszentrum Jülich, 52425 Jülich, Germany

[2]Anatomisches Institut, Rheinische Friedrich-Wilhelm-Universität, 53115 Bonn, Germany

[3]present address: Center for Translational Neuromedicine, Københavns Universitet, 2200 København N, Denmark

Table of content for Supplementary Figures:

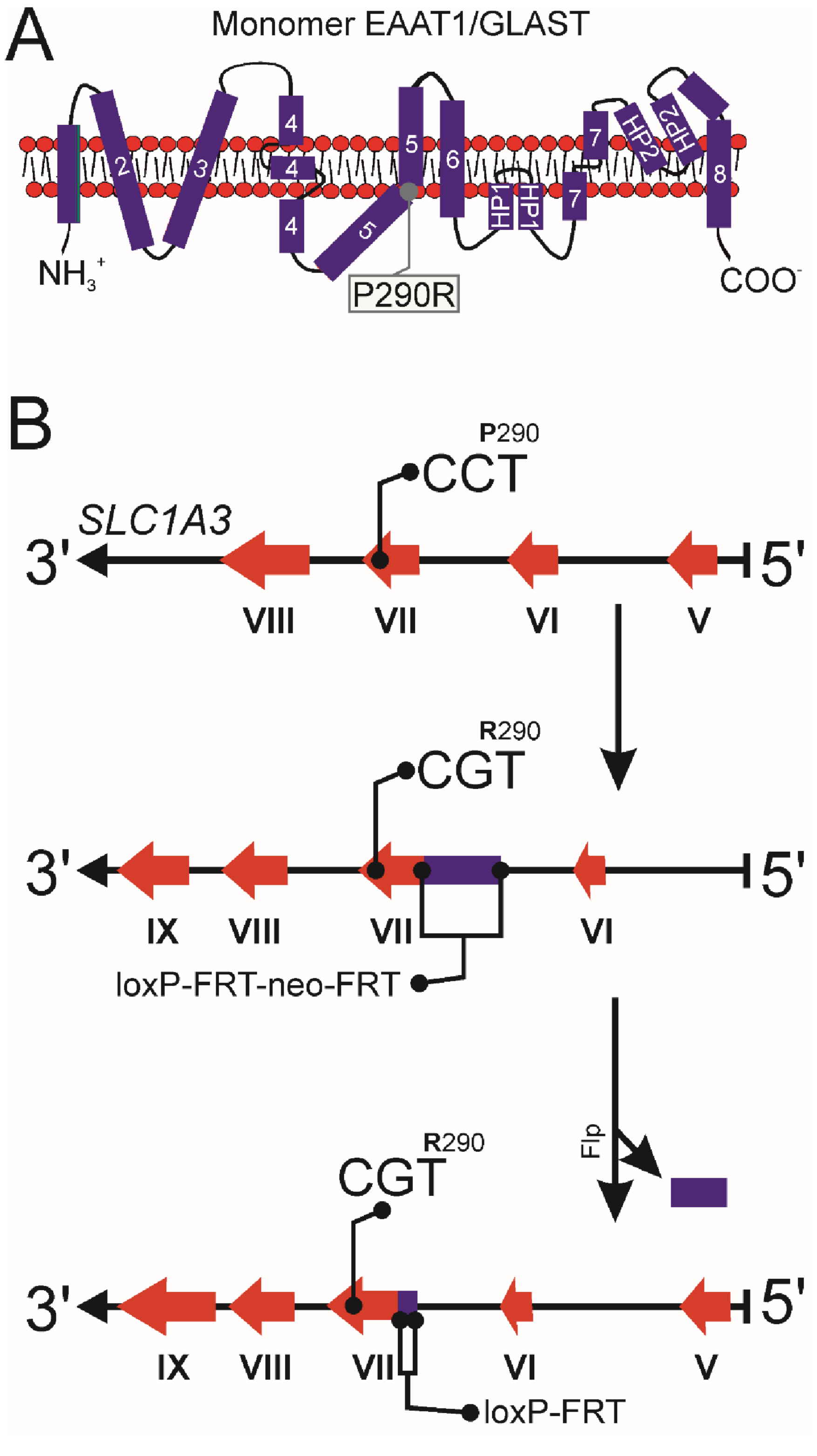

Supplementary Figure 1 – Targeting strategy of *Slc1a3*$^{P290R/+}$ transgene insertion. Transmembrane topology of EAAT1 monomers (**A**) and localization of the disease-associated mutation P290R. Schematic diagram (**B**) showing the location of the P290R mutation in the gene *Slc1a3* with target codons for the WT *Slc1a3*-targeting construct used for homologous recombination (B, top). Recombinase-mediated nucleotide exchange inserts the mutation and an FRT-flanked neomycin cassette (for selection) into exon VII (SA, short arm; LA, long arm; neo, neomycin, B, middle). The mutated *Slc1a3* gene after Flp-mediated excision of the neomycin cassette (B, bottom).

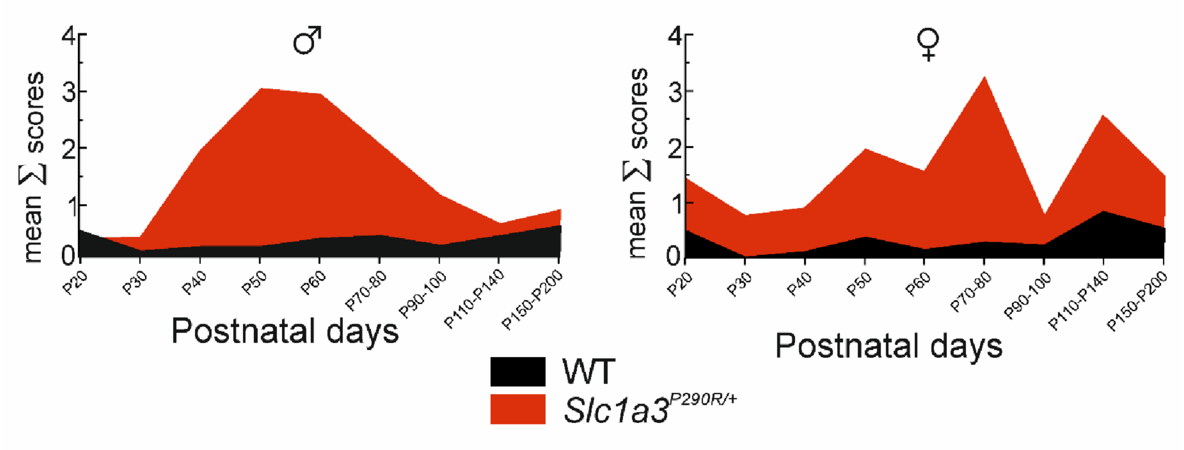

Supplementary Figure 2 – Fitness of WT and transgenic *$Slc1a3^{P290R/+}$* mice. Age dependences of fitness for WT and *$Slc1a3^{P290R/+}$* mice of mean sum of scores (see Supplementary Table 2) for male (left) and female (right) animals. These data represent the mean scores of 21/21 ♂ and 10/14 ♀ (WT/Mut) regularly scored animals.

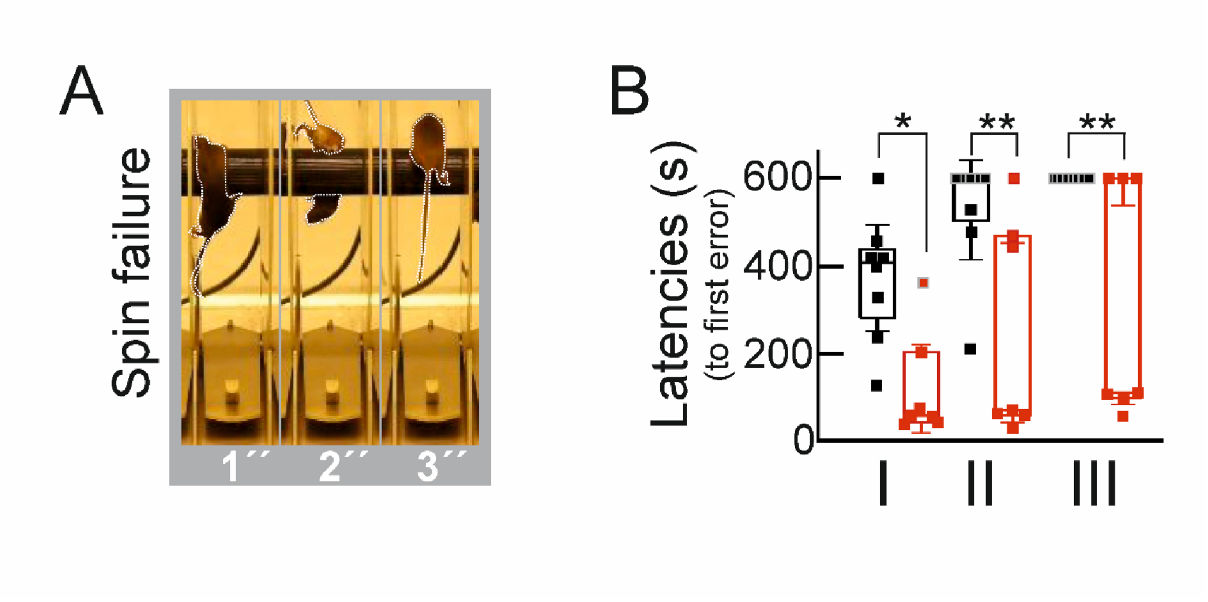

Supplementary Figure 3 – Spin failure case and error latencies of WT and mutant mice on the rotarod. The image series shows a representative case of a spin failure during the rotarod test, where a mouse is rotating with the waltz (**A**). Graph (**B**) depicts analysis of first error latencies for WT (black) and *$Slc1a3^{P290R/+}$* (red) mice without differentiation between *spin*- and *fall*- errors for the rotarod test shown in Fig. 1 (2-*way* ANOVA with repeated measures and Holm-Sidak *post hoc* tests); all *P*–values are available online for this figure (Supplementary Table 3).

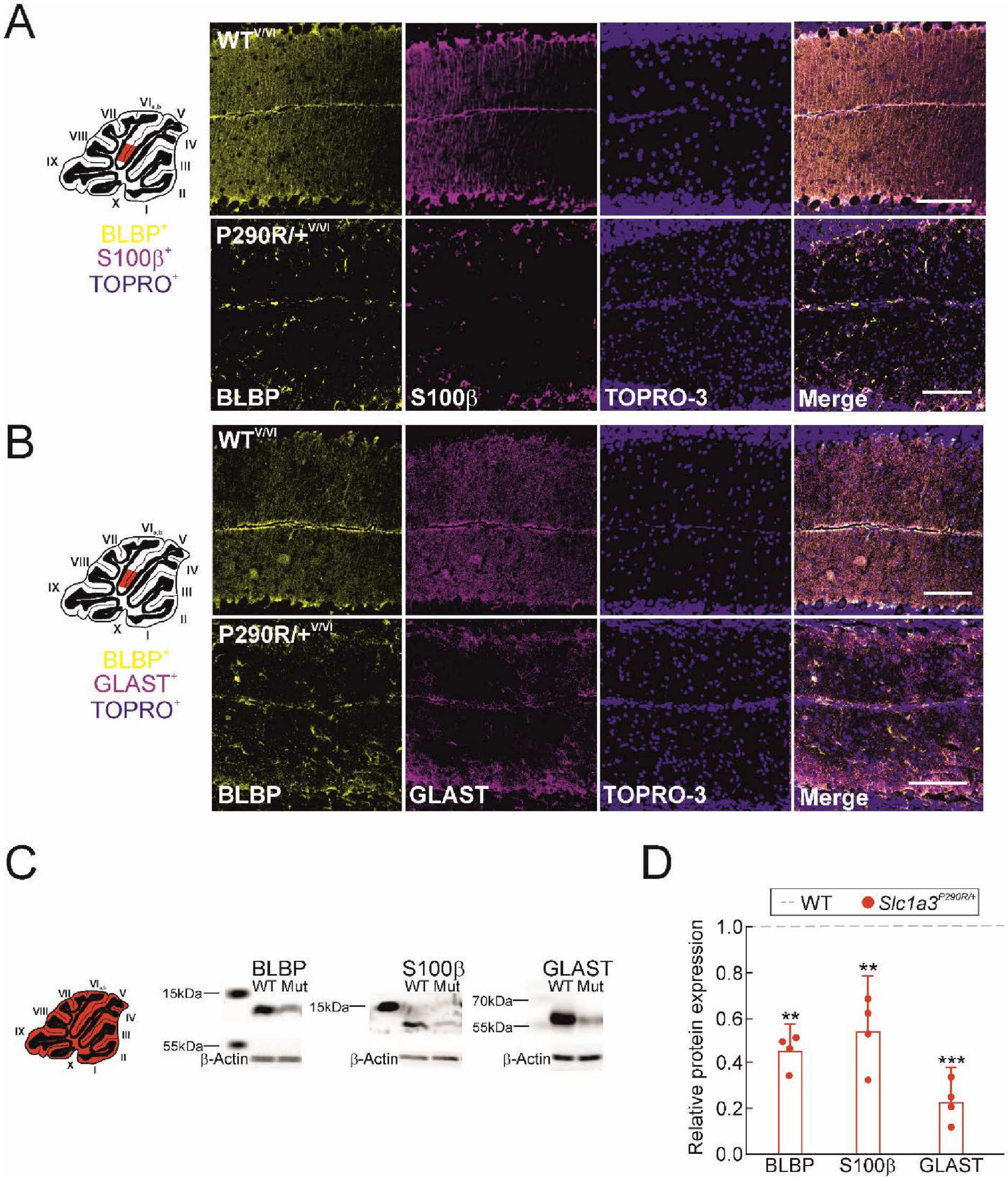

Supplementary Figure 4 – Immunostaining of Bergmann glial cells with specific markers. Confocal images of cerebella from WT and *Slc1a3*$^{P290R/+}$ mice immunostained against glial markers BLBP, S100β and BLBP, GLAST (**A**, **B**) show the differences in protein expression and cellular distribution between cerebella from WT and mutant mice. Western blots from whole cerebella lysates (**C**) depict relative protein expression of BLBP, S100β, and GLAST for WT and *Slc1a3*$^{P290R/+}$ cerebella. Bar graphs providing relative intensities of western blot signals (**D**) illustrate significant reduction of tested Bergmann glial markers a in *Slc1a3*$^{P290R/+}$. In D the relative expression of glial markers is shown as bars with means (±*CI*), after normalization to WT. Each marker was tested in cerebellar lysates from *n* = 3–4 / 4 (WT/Mut) different animals (2-*way* ANOVA and Holm-Sidak *post hoc* tests); all *P*–values are available online for this figure (Supplementary Table 3). Scale bars: 100 µm.

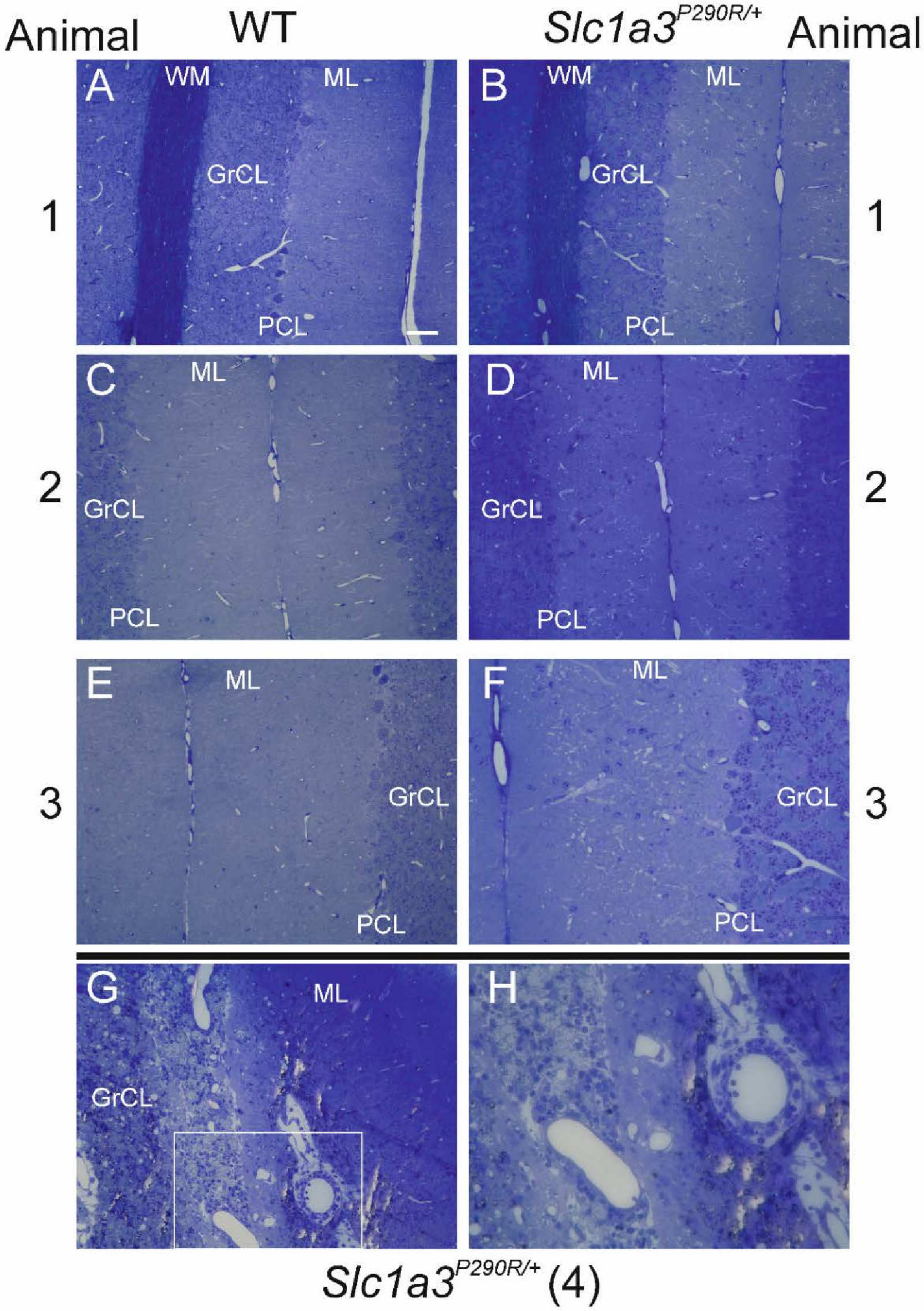

Supplementary Figure 5 – Semisections from the cerebella of WT and *Slc1a3*$^{P290R/+}$ animals at P50. A–F Nissl-stained sagittal semisections from cerebella in three WT (A, C, E) and *Slc1a3*$^{P290R/+}$ (B, D, F) mice, showing more nuclei in the molecular layer of cerebella in *Slc1a3*$^{P290R/+}$ mice. Nissl-stained sagittal section from a cerebellum of a fourth *Slc1a3*$^{P290R/+}$ mouse (**G**, **H**) shows a more severe cellular phenotype at this age. Magnified inset (H) of G. Scale bars: 50 µm (A–D, G), 25 µm (E, F, H).

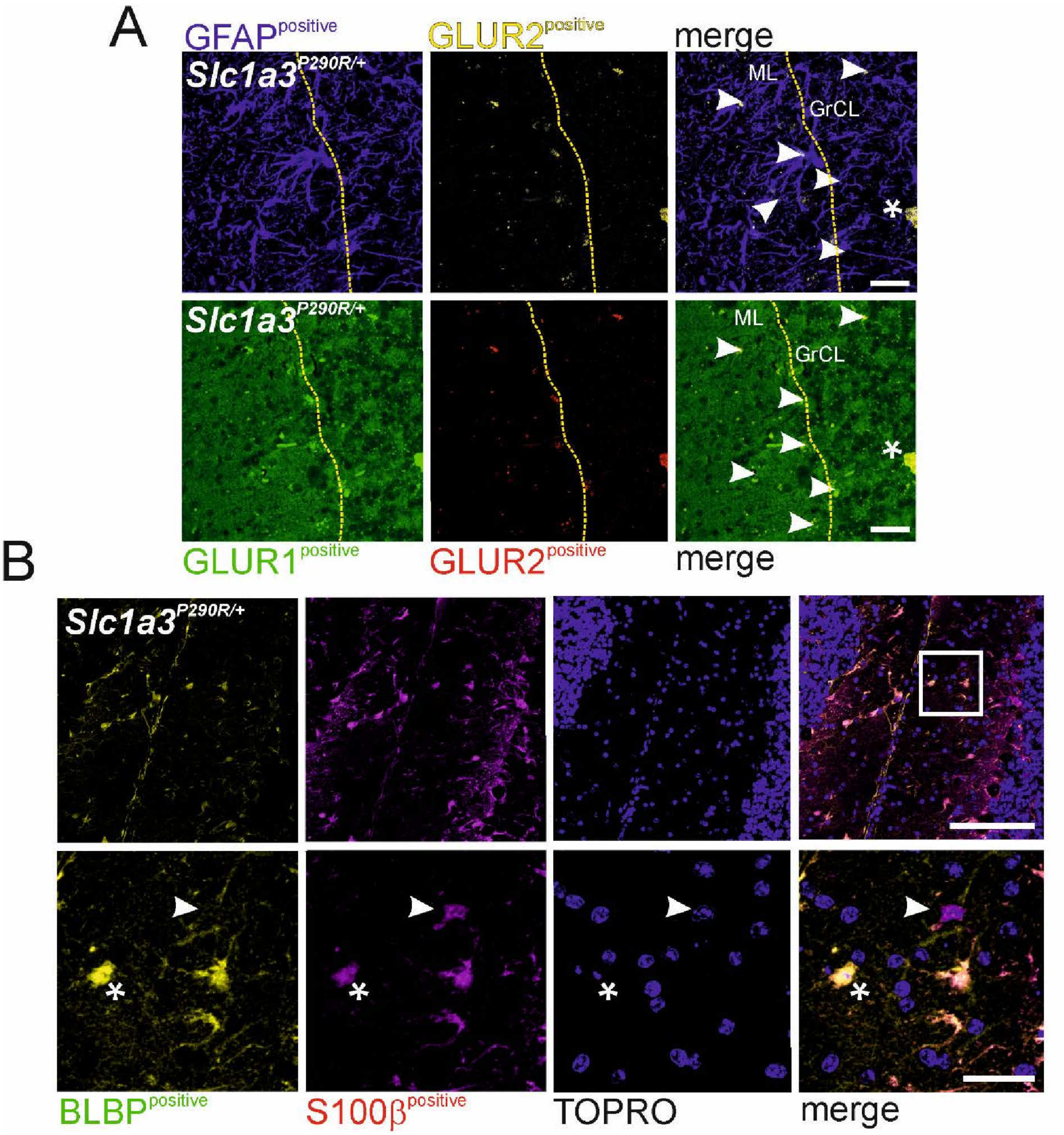

Supplementary Figure 6 – Glial cell types in the molecular layer of *Slc1a3*$^{P290R/+}$. Colocalization (**A**, top) of GFAP and GLUR2 is shown as white (arrowheads). (**A**, bottom) Colocalization of GLUR1 and GLUR2 is shown as yellow (arrowheads). Scale bar: 25 µm. Incidence of two different populations (**B**, BLBP^{positive}/S100β^{positive} (asterisks), BLBP^{negative}/S100β^{positive} (arrowheads)) of glial cells in the molecular layer from *Slc1a3*$^{P290R/+}$ mice. Scale bars 25 µm (A), 100 µm (top), 25 µm (bottom, B).

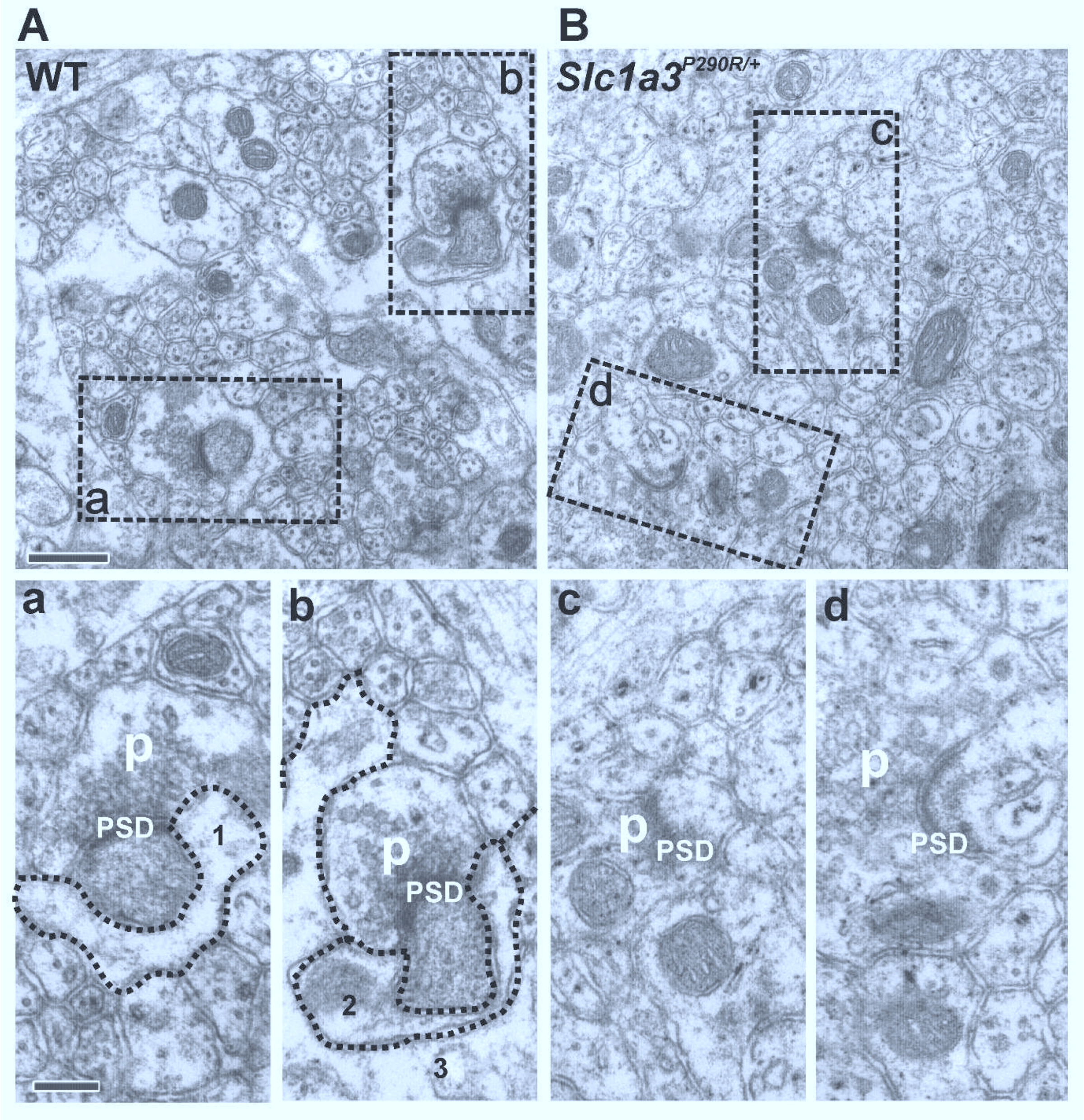

Supplementary Figure 7 – Electron micrographs show impaired wrapping of synapses in the molecular layer through glial cells in *Slc1a3*$^{P290R/+}$ samples. Overview with typical synapse morphology in a molecular layer from a WT mouse (**A**). Magnified insets of two representative regions (**a**, **b**) show the postsynaptic densities (PSD) and the presynapses (p). Dotted lines refer to glial cells, which are involved in shielding the synapse (1–3; bottom). Overview of an area in the molecular layer from a *Slc1a3*$^{P290R/+}$ mouse (**B**). Glial wrapping is virtually absent in *Slc1a3*$^{P290R/+}$ mice as shown in the magnified insets (**c**, **d**). Scale bars: 500 nm (A, B), 200 nm (a – d).

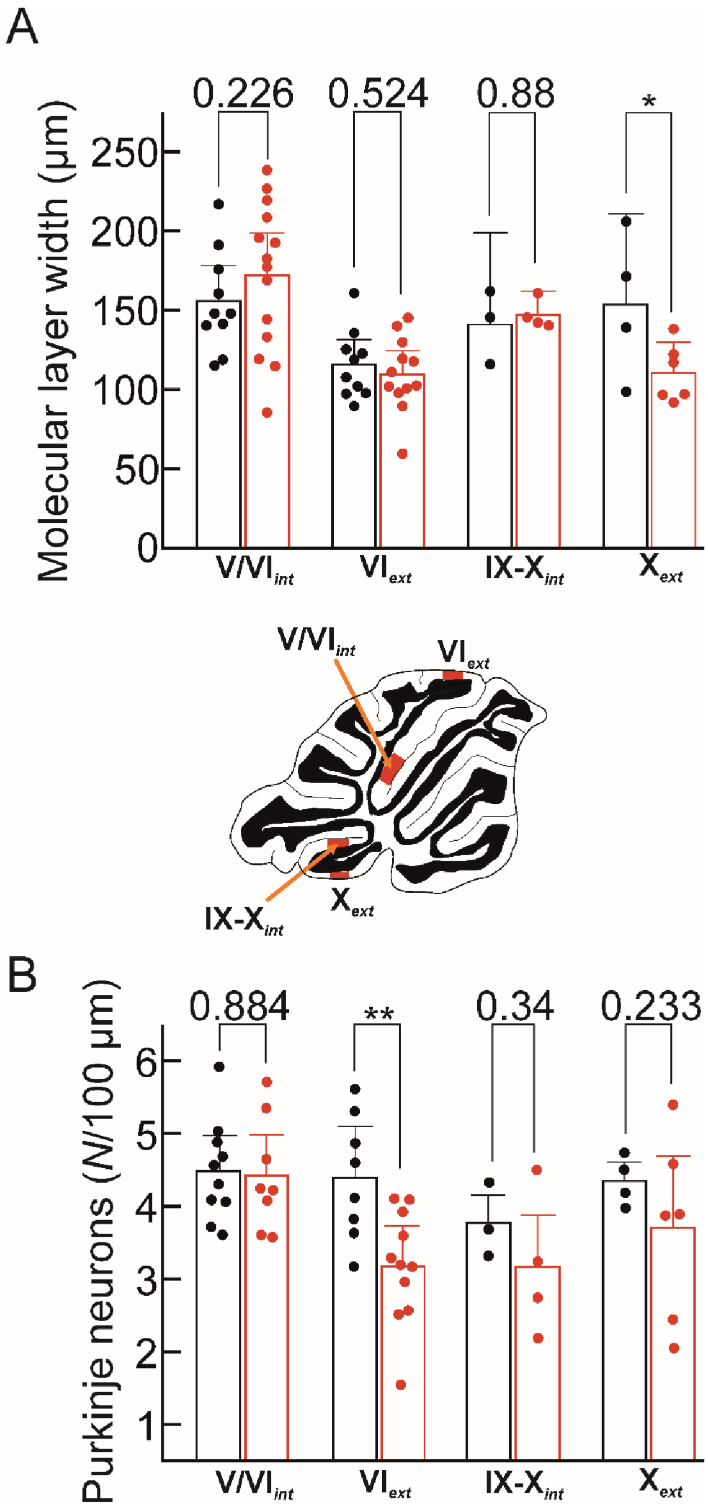

Supplementary Figure 8 – Statistical analysis of molecular layer thickness and Purkinje neuron numbers in WT and *Slc1a3*$^{P290R/+}$ animals. Bar graphs showing mean thicknesses of molecular layers (±*CI*) in the indicated regions (**A**) in the inset (middle). Bar graphs showing mean numbers (±*CI*) of Purkinje neurons/100 µm layer (**B**) in the indicated regions; WT (black), *Slc1a3*$^{P290R/+}$ (red); all points represent the values obtained from individual animals, respectively (A, B: 2-*way* ANOVA with Holm-Sidak *post hoc* tests); all *P*–values are available online for this figure (Supplementary Table 3).

Supplementary Figures
for
Increased glutamate transporter-associated anion currents cause glial apoptosis in episodic ataxia 6

Peter Kovermann[1], Verena Untiet[3], Yulia Kolobkova[1], Miriam Engels[1],Stephan Baader[2], Karl Schilling[2], and Christoph Fahlke[1]

[1]Institut für Biologische Informationsprozesse, Molekular- und Zellphysiologie (IBI-1), Forschungszentrum Jülich, 52425 Jülich, Germany

[2]Anatomisches Institut, Rheinische Friedrich-Wilhelm-Universität, 53115 Bonn, Germany

[3]present address: Center for Translational Neuromedicine, Københavns Universitet, 2200 København N, Denmark

Table of content for Supplementary Figures:

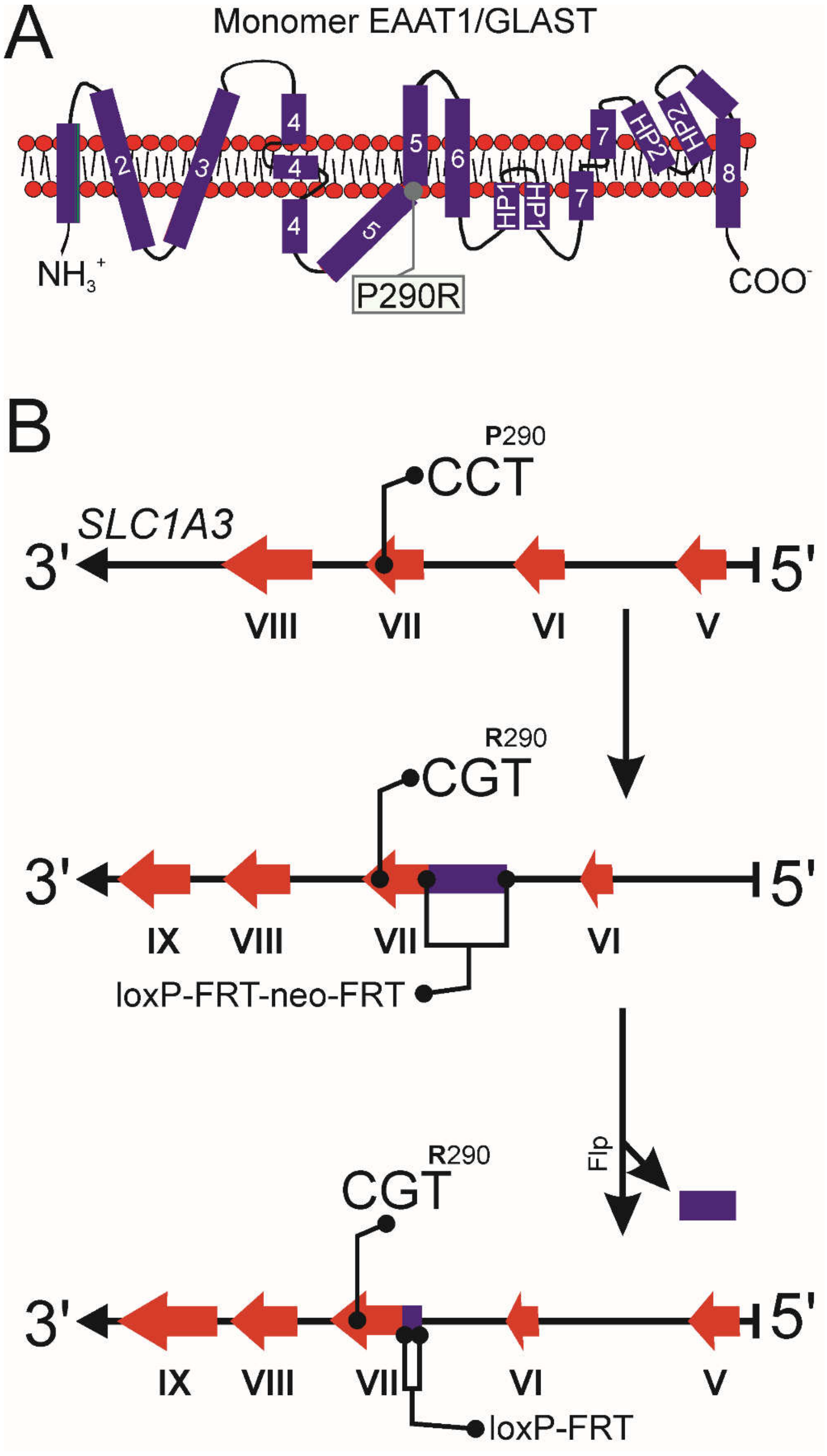

Supplementary Figure 1 – Targeting strategy of *Slc1a3*$^{P290R/+}$ transgene insertion. Transmembrane topology of EAAT1 monomers (**A**) and localization of the disease-associated mutation P290R. Schematic diagram (**B**) showing the location of the P290R mutation in the gene *Slc1a3* with target codons for the WT *Slc1a3*-targeting construct used for homologous recombination (B, top). Recombinase-mediated nucleotide exchange inserts the mutation and an FRT-flanked neomycin cassette (for selection) into exon VII (SA, short arm; LA, long arm; neo, neomycin, B, middle). The mutated *Slc1a3* gene after Flp-mediated excision of the neomycin cassette (B, bottom).

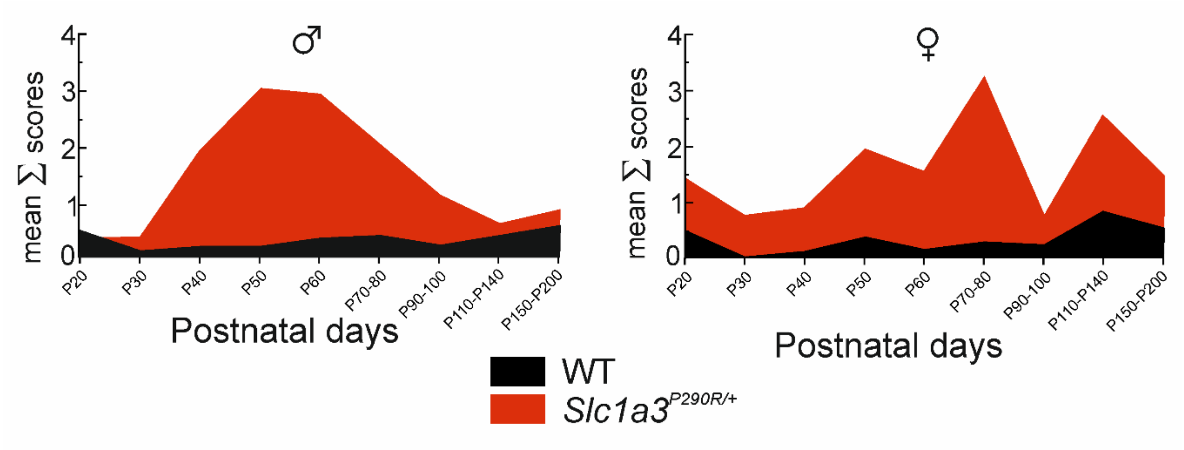

Supplementary Figure 2 – Fitness of WT and transgenic *Slc1a3*$^{P290R/+}$ mice. Age dependences of fitness for WT and *Slc1a3*$^{P290R/+}$ mice of mean sum of scores (see Supplementary Table 2) for male (left) and female (right) animals. These data represent the mean scores of 21/21 ♂ and 10/14 ♀ (WT/Mut) regularly scored animals.

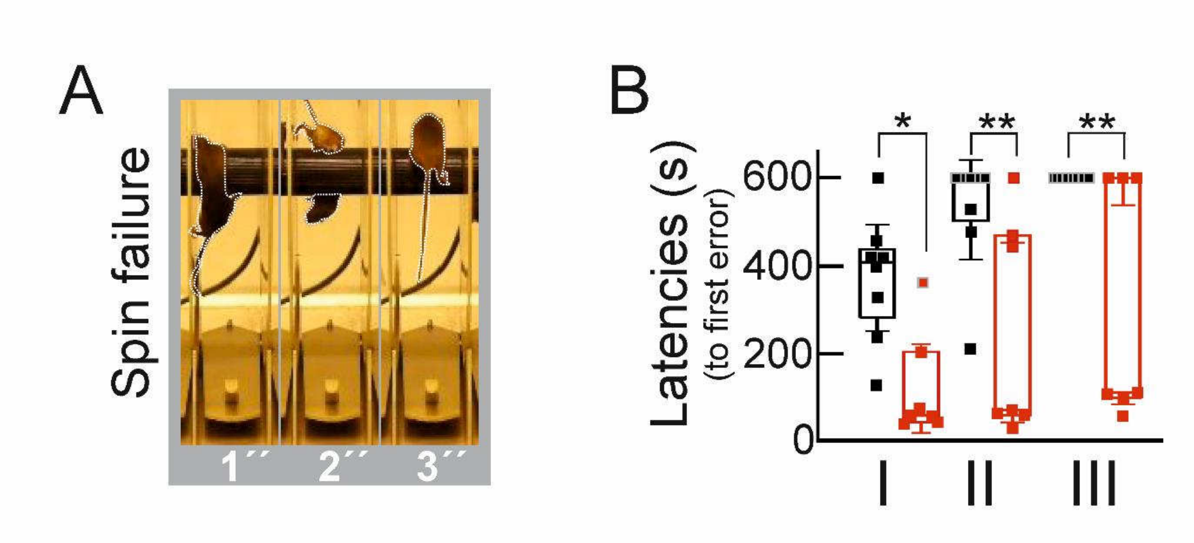

Supplementary Figure 3 – Spin failure case and error latencies of WT and mutant mice on the rotarod. The image series shows a representative case of a spin failure during the rotarod test, where a mouse is rotating with the waltz (**A**). Graph (**B**) depicts analysis of first error latencies for WT (black) and *Slc1a3*$^{P290R/+}$ (red) mice without differentiation between *spin*- and *fall*- errors for the rotarod test shown in Fig. 1 (2-*way* ANOVA with repeated measures and Holm-Sidak *post hoc* tests); all *P*–values are available online for this figure (Supplementary Table 3).

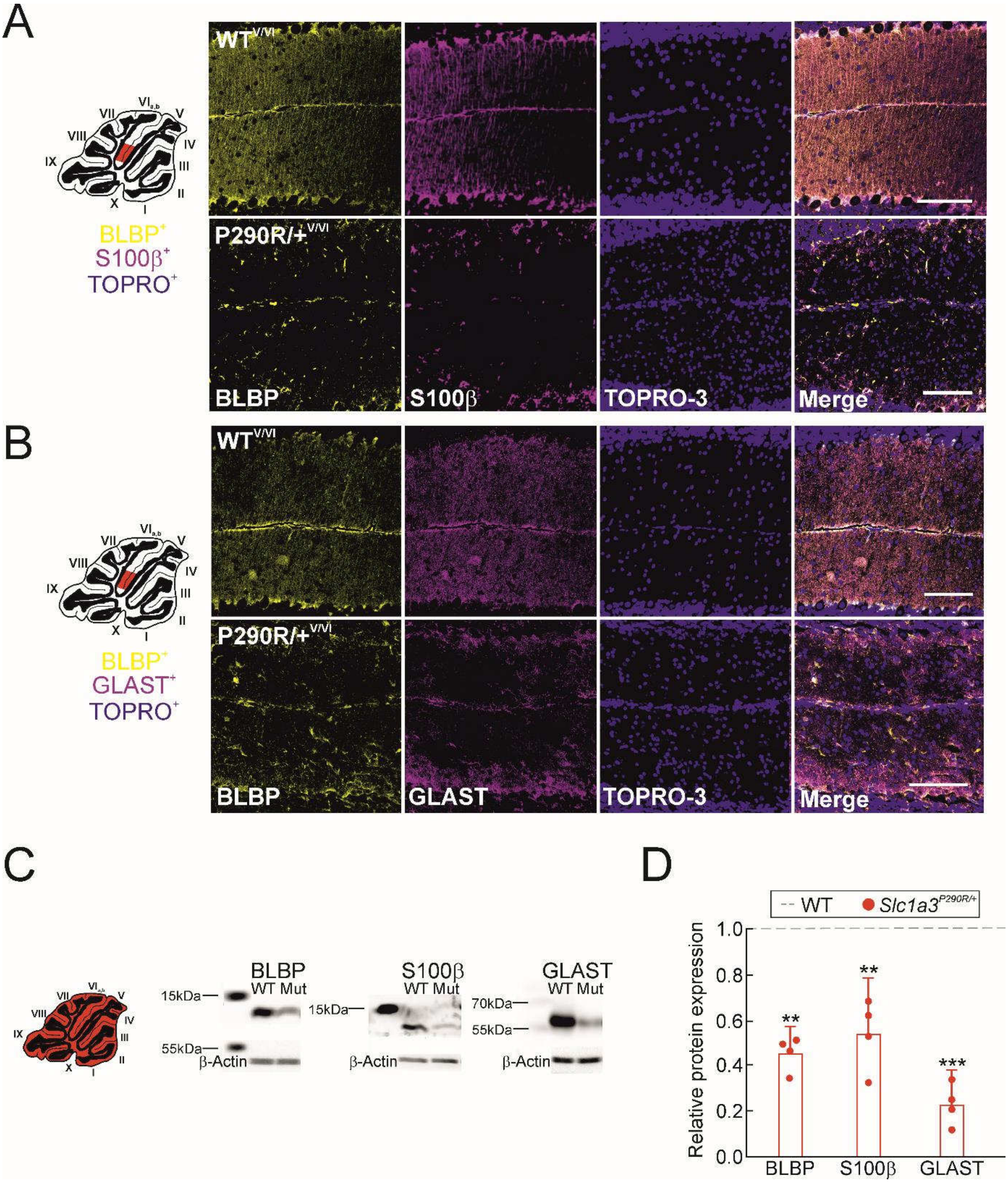

Supplementary Figure 4 – Immunostaining of Bergmann glial cells with specific markers. Confocal images of cerebella from WT and *Slc1a3*$^{P290R/+}$ mice immunostained against glial markers BLBP, S100β and BLBP, GLAST (**A**, **B**) show the differences in protein expression and cellular distribution between cerebella from WT and mutant mice. Western blots from whole cerebella lysates (**C**) depict relative protein expression of BLBP, S100β, and GLAST for WT and *Slc1a3*$^{P290R/+}$ cerebella. Bar graphs providing relative intensities of western blot signals (**D**) illustrate significant reduction of tested Bergmann glial markers a in *Slc1a3*$^{P290R/+}$. In D the relative expression of glial markers is shown as bars with means (±*CI*), after normalization to WT. Each marker was tested in cerebellar lysates from n = 3–4 / 4 (WT/Mut) different animals (2-*way* ANOVA and Holm-Sidak *post hoc* tests); all *P*–values are available online for this figure (Supplementary Table 3). Scale bars: 100 µm.

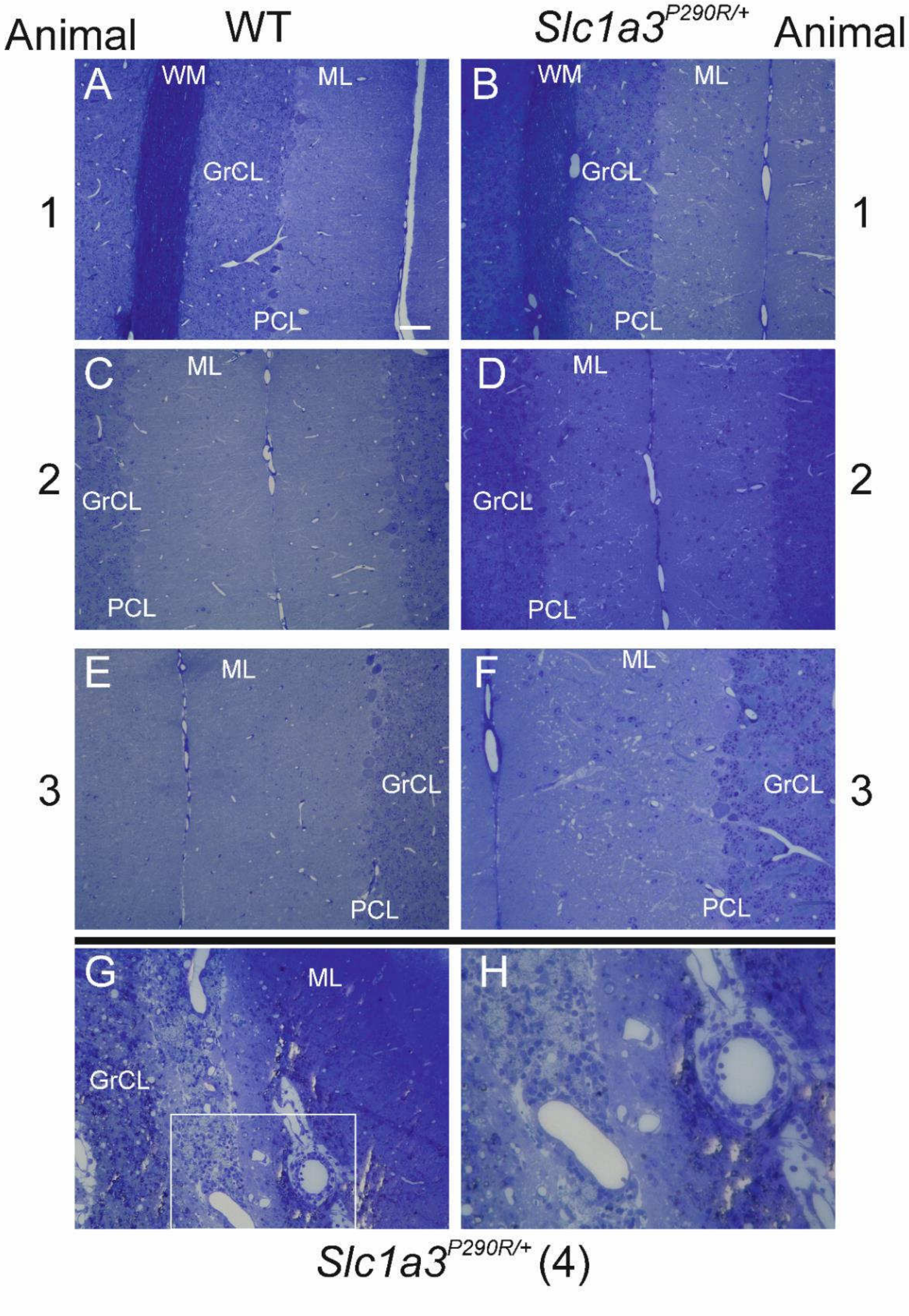

Supplementary Figure 5 – Semisections from the cerebella of WT and *Slc1a3*$^{P290R/+}$ animals at P50. A–F Nissl-stained sagittal semisections from cerebella in three WT (A, C, E) and *Slc1a3*$^{P290R/+}$ (B, D, F) mice, showing more nuclei in the molecular layer of cerebella in *Slc1a3*$^{P290R/+}$ mice. Nissl-stained sagittal section from a cerebellum of a fourth *Slc1a3*$^{P290R/+}$ mouse (**G**, **H**) shows a more severe cellular phenotype at this age. Magnified inset (H) of G. Scale bars: 50 µm (A–D, G), 25 µm (E, F, H).

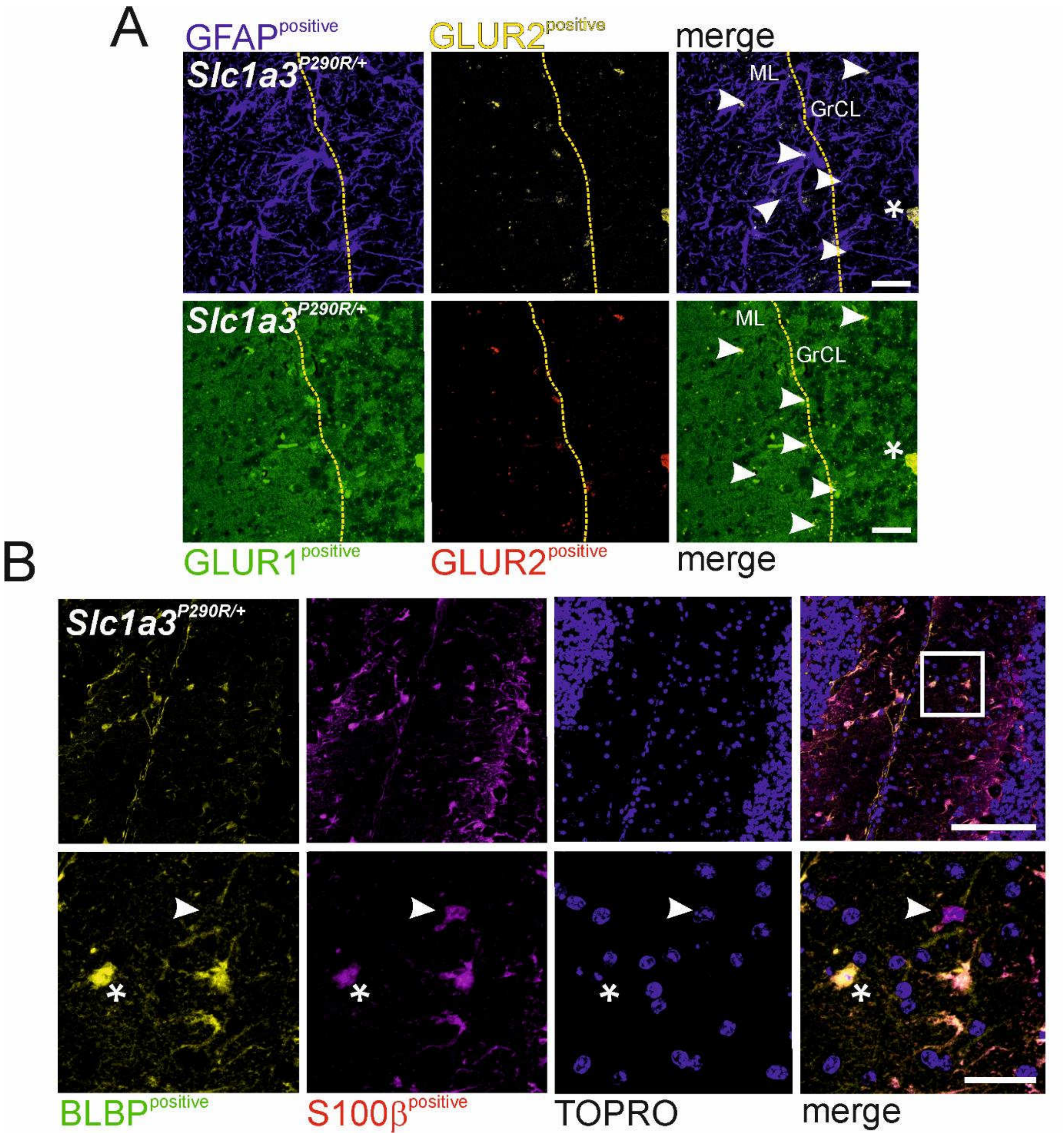

Supplementary Figure 6 – Glial cell types in the molecular layer of *Slc1a3*$^{P290R/+}$. Colocalization (**A**, top) of GFAP and GLUR2 is shown as white (arrowheads). (**A**, bottom) Colocalization of GLUR1 and GLUR2 is shown as yellow (arrowheads). Scale bar: 25 µm. Incidence of two different populations (**B**, BLBP^{positive}/S100β^{positive} (asterisks), BLBP^{negative}/S100β^{positive} (arrowheads)) of glial cells in the molecular layer from *Slc1a3*$^{P290R/+}$ mice. Scale bars 25 µm (A), 100 µm (top), 25 µm (bottom, B).

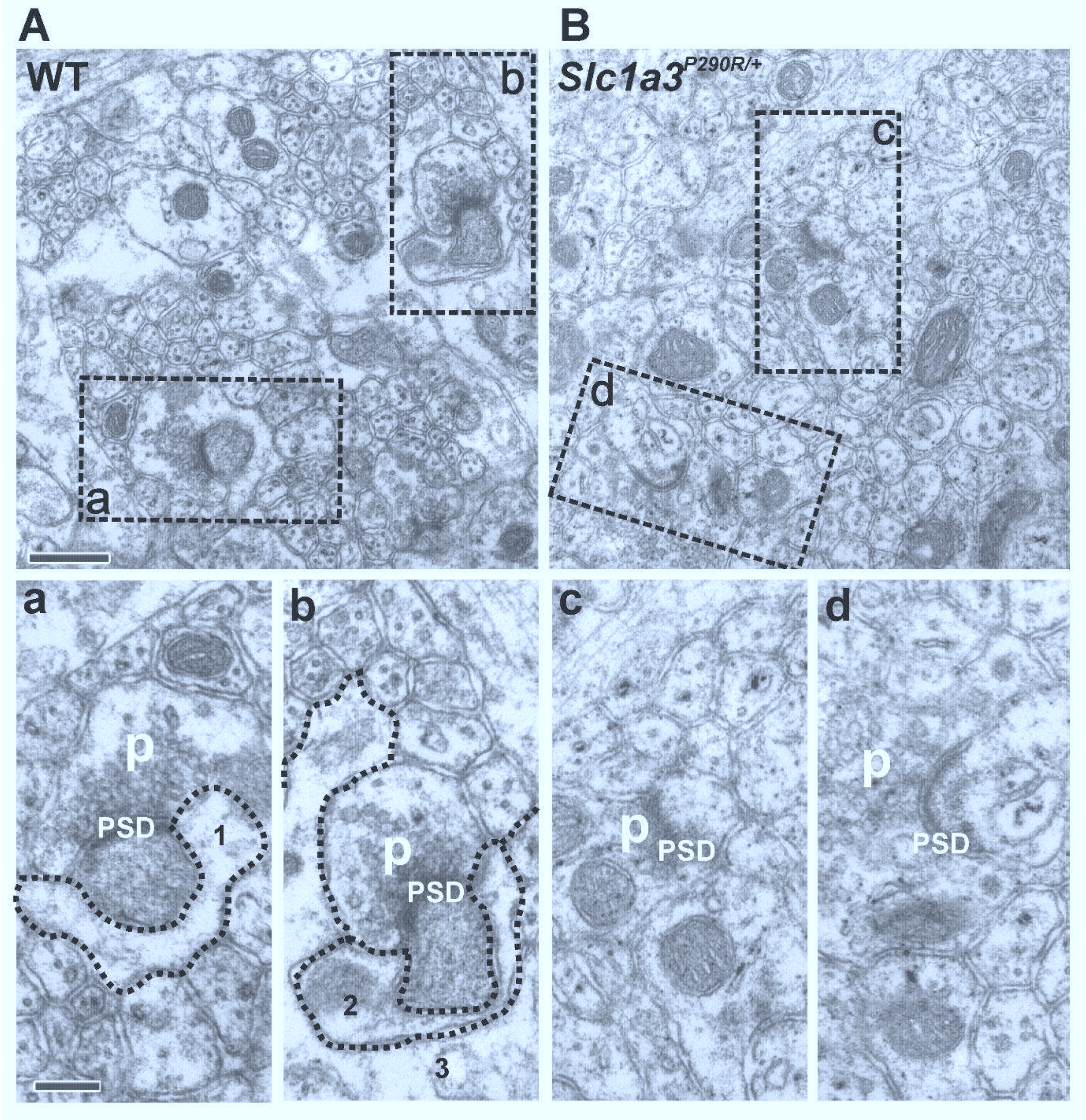

Supplementary Figure 7 – Electron micrographs show impaired wrapping of synapses in the molecular layer through glial cells in *Slc1a3*$^{P290R/+}$ samples. Overview with typical synapse morphology in a molecular layer from a WT mouse (**A**). Magnified insets of two representative regions (**a**, **b**) show the postsynaptic densities (PSD) and the presynapses (p). Dotted lines refer to glial cells, which are involved in shielding the synapse (1–3; bottom). Overview of an area in the molecular layer from a *Slc1a3*$^{P290R/+}$ mouse (**B**). Glial wrapping is virtually absent in *Slc1a3*$^{P290R/+}$ mice as shown in the magnified insets (**c**, **d**). Scale bars: 500 nm (A, B), 200 nm (a – d).

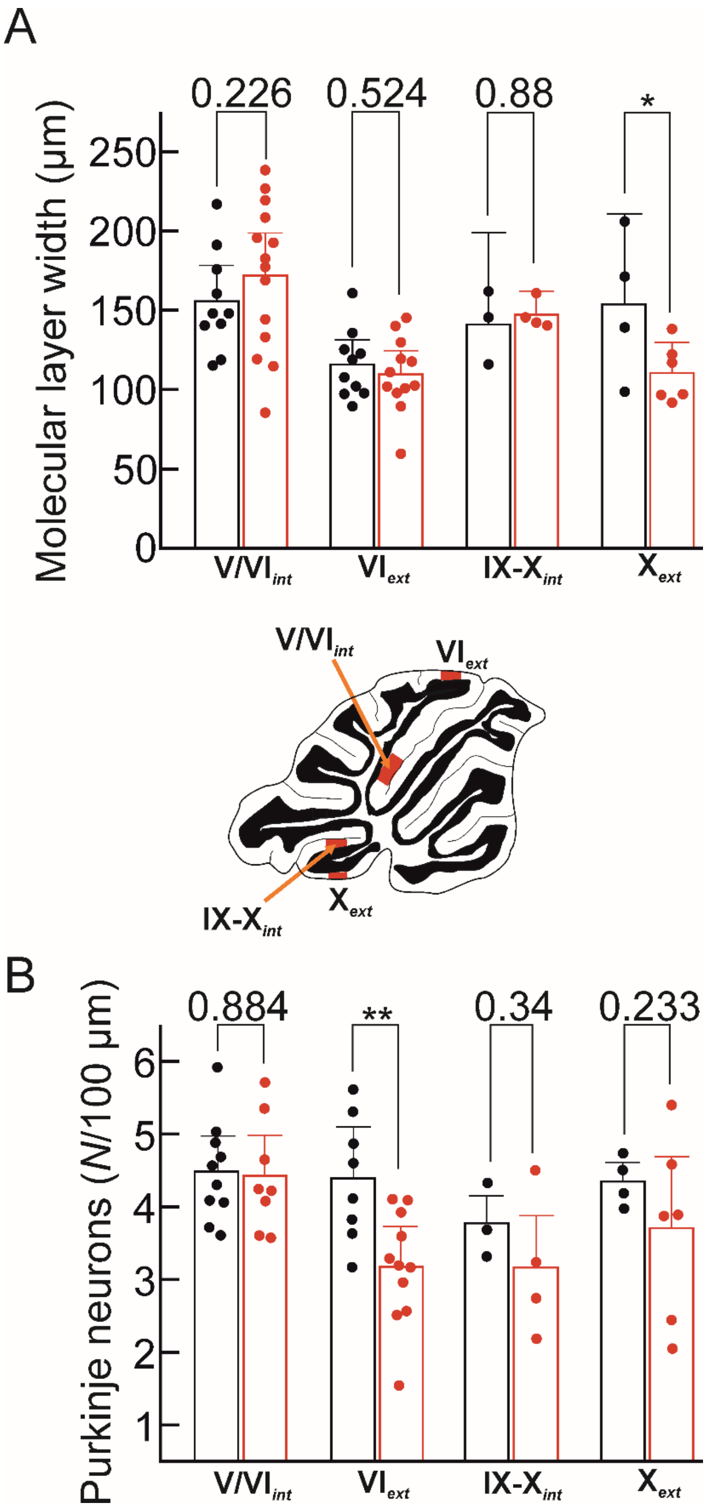

Supplementary Figure 8 – Statistical analysis of molecular layer thickness and Purkinje neuron numbers in WT and *Slc1a3*$^{P290R/+}$ animals. Bar graphs showing mean thicknesses of molecular layers (±*CI*) in the indicated regions (**A**) in the inset (middle). Bar graphs showing mean numbers (±*CI*) of Purkinje neurons/100 µm layer (**B**) in the indicated regions; WT (black), *Slc1a3*$^{P290R/+}$ (red); all points represent the values obtained from individual animals, respectively (A, B: 2-*way* ANOVA with Holm-Sidak *post hoc* tests); all *P*–values are available online for this figure (Supplementary Table 3).

Supplementary Material

for

Increased glutamate transporter-associated anion currents cause glial apoptosis in episodic ataxia 6

Peter Kovermann[1], Verena Untiet[1,3], Yulia Kolobkova[1], Miriam Engels[1], Stephan Baader[2], Karl Schilling[2], and Christoph Fahlke[1]

[1]Institut für Biologische Informationsprozesse, Molekular- und Zellphysiologie (IBI-1), Forschungszentrum Jülich, 52425 Jülich, Germany

[2]Anatomisches Institut, Rheinische Friedrich-Wilhelm-Universität, 53115 Bonn, Germany

[3]Center for Translational Neuromedicine, Københavns Universitet, 2200 København N, Denmark

Table of content for Supplementary Methods and Tables:

1. Supplementary Methods

2. Supplementary Tables

1. Supplementary Methods

1.1 Transgenic animals

Knock-in *Slc1a3*^{tm1P290RCfa} (*Slc1a3*$^{P290R/+}$) mice were generated by site-directed mutagenesis using a mutant *Slc1a3* allele located on chromosome 15 (at 3.82 cM) and encoding a P290R substitution in exon 7. Briefly, a fragment covering exons 4–8 of the *Slc1a3* locus was subcloned and the P290R sequence (agg to gcg) was inserted via PCR synthesis into the end of exon 7 (Polygene Transgenetics, Switzerland). Positive clones were injected into blastocysts from C57BL/6N mice, and surviving blastocysts were the transferred to a CD–1 foster mouse. Germline chimeric foster mice were crossbred with C57BL/6N-derived FLP-deleter mice (B6;SJL-Tg(ACTFLPe)9205Dym/J; JANVIER LABS, France) to excise the neomycin cassette (Supplementary Fig. 1). Since mortality of C57BL/6 knock-in mice prevented successful breeding, we backcrossed the mutation into the more robust mouse strain 129/SvJ (Taconic Biosciences GmbH, Germany) for 10 generations. The animals were housed under standard conditions in the animal facility of Forschungszentrum Jülich according to institute guidelines under a 12 h light/dark cycle (light: 6:00am–6:00pm). Animal testing was done during the light phase. All experiments complied with the German Law for the Protection of Animals and were approved by the Forschungszentrum Jülich and LANUV (State Agency for Nature, Environment and Consumer Protection) of North Rhine-Westphalia (reference nos 84–02.04.2014.A334/A335, to P.K.). The health status of mutant animals was continuously monitored, and animals were treated in strict accordance with defined stop criteria (Supplementary Table 1).

1.2 Analysis of motor coordination of transgenic mice

Motor coordination of transgenic animals was tested with two different tests. We used ledge tests (Guyenet *et al.*, 2010) to test the behavior of animals on a narrow path.

Animals were placed on a 1 cm wide ledge and the test were video-recorded for analysis. Mice younger than postnatal day 30 (P30) were not subjected to the test because they tended be more active (e.g. jumpiness) (van Abeelen and Schoones, 1977; Curzon, 2009). The mean stumble ratio was calculated from the video recordings as the average error rate for each animal during all traverses across the ledge using the equation:

$$\boldsymbol{stumble\ ratio} = \frac{\boldsymbol{\Sigma_1^n \left(N_{failures} \cdot N_{steps}^{-1}\right)_1}}{\boldsymbol{n}} \text{(Eq. 1).}$$

n = number of traverses (2´); $N_{failures}$ = number of paw slips/traverse; N_{steps} = number of steps/traverse.

Mice were as well subjected to another test of motor coordination, the rotarod test. This test measures the time until an animal falls from a rotating rod. The rotarod sessions were video-recorded and then analyzed by latencies to fall and counting spin failures. For each fall event, the remaining score (time in sec) was subtracted from the starting value of 600 (~ test period: 600 s), and the resulting value was corrected for spin failures (Supplementary Fig. 3) by subtracting three points for each missed cycle. Spin failure frequencies for WT and mutant mice were calculated from the number of spin failures during latency to fall. We assumed a lower limit of 1/600 s (≈0.0017 Hz, Fig. 1E). In initial tests we observed that mutant males increase their latency to fall from the rod via excessive spin failures, preventing an appropriate comparison of WT and mutant mice. We therefore excluded males from rotarod tests. Time series data of rotarod tests were averaged and transformed into survival plots (Kaplan, 1958), and corrected latencies were added as box plots (Fig. 1D and F). Blinding and randomization was not possible because of the severe phenotype of mutant animals. The State Agency for Nature, Environment and Consumer Protection of North Rhine-Westphalia (reference nos 84–02.04.2014.A334/A335, to P.K.) ordered permanent observation of transgenic mice during breeding and maintenance. Tests were always performed with all litters, the group sizes were determined by genotype frequency (50:50). All data points in Fig. 1C, and F represent mean values obtained from individual animals during 3 trials per session.

1.3 Visualization and quantification of specific cell types and components

Mice were anesthetized with isoflurane (Piramal Healthcare, UK) and decapitated. The cerebella were excised, transferred to 4% paraformaldehyde (PFA, $[CH_2O]_n$) in phosphate buffer (PB; in mM, 81 $NaH_2PO_4 \cdot 2H_2O$, 9 $Na_2HPO_4H_2O$, pH 7.4), and stored in fixative for 5 days (at 4°C). After dehydration in a graded ethylalcohol series (50%, 70%, 90%, 100% EtOH) brains were embedded in paraffin and sagittal sections (5 µm or 7 µm thick) were cut for immunostainings. Nissl staining was performed as previously described (Paul *et al*, 2008). For immunostaining, endogenous peroxidases were inactivated (in mM, 21 $C_6H_8O_7$ and 6 Na_2HPO_4, 15% (v/v) H_2O_2 for 15´, at RT), and epitopes were unmasked (2000 Tris and 63 EDTA, pH 8.0, at 100°C for 20´) and blocked overnight (bovine serum albumin 1% (w/v) in PB, at 4°C). Sections were incubated for 1-2 days with primary and 45-60´with secondary antibodies diluted in CTA (i.e. 5%ChemiBLOCKER, Merck–Millipore, in PB containing 1% Triton-X100 and 0.05% NaN_3) and 1% Triton-X100. For visualization, sections were incubated in cyanine-dye conjugated secondary antibodies for 60´ at room temperature (RT). A list of all used antibodies is given in in Supplementary Table 2. Fiber or cell numbers in WT and mutant cerebella was counted in sagittal vermis sections (lobes V/VI and IX/X). Bergmann glia cells were quantified by counting the number of $GFAP^{positive}$ fibers in the molecular layer (ML) and the density of neurons or astrocytes by counting the number of $NeuN^{positive}$ cells or $GFAP^{positive}$ cells with a typical multipolar astrocyte shape in defined areas.

1.4 Quantification of Bergmann glia cells

We immunostained paraffin slices (4 µm) from mice cerebella with typical astrocytic and Bergmann glial markers as brain lipid binding protein (BLBP), the Ca^{2+} binding protein S100β, and glutamate-aspartate transporter (GLAST) and counterstained nuclei with TOPRO-3 for confocal microcopy. Bergmann glial cell somata in the Purkinje cell layer (PCL) and ectopic glia in the molecular layer (ML, lobes V/VI and IX/X) were counted separately. Cell numbers are provided as mean numbers of Bergmann glia per 100 µm length (PCL or ML) from individual animals.

1.5 Quantification of glutamatergic and GABAergic synapses in the molecular layer

To determine the number of synapses in the cerebellar molecular layer, paraffin slices were incubated overnight with a combination of primary antibodies against vesicular glutamate transporter 1, vesicular glutamate transporter 2, and anti-glutamate decarboxylase 65/67 and subsequently in cyanine-dye conjugated secondary antibodies from donkey for 60´ at RT. Densities of synapses were quantified by counting VGLUT1$^{\text{positive}}$, VGLUT2-$^{\text{positive}}$ and GAD65/67$^{\text{positive}}$ signals within single confocal planes in randomly selected areas of different sizes of V/VI$_{int}$, VI$_{ext}$, IX/X$_{int}$, and X$_{ext}$. Synapse density was calculated in n = 3-5/4-9 (WT/Mut) mice from means of n = 144/212 (WT/Mut) test areas. Densities are given as boutons per 100 µm^2.

1.6 Transmission electron microscopy

Electron microscopical pictures (Supplementary Fig. 7) were prepared as described previously (Miething, 1992; Jankowski *et al.*, 2009). Briefly, mice were perfused with Karnovsky solution (3% PFA), 3% glutaraldehyde ($C_5H_8O_2$), in phosphate buffered saline containing 10 mM $NaH_2PO_4 \cdot H_2O$ and 150 mM NaCl, pH 7.2) and dissected cerebella were immersed in the same fixative for 6 h. Tissue blocks (1 mm thick) were cut and incubated in 1% Osmiumtetroxid (OsO_4) at RT for 120´. Sections were then dehydrated and embedded in Epon 812 using a 3:2 mixture of Epon A (38% Glycidether 100 in 2-Dodecenylsuccinic acid anhydride, $C_{16}H_{26}O_3$) and Epon B (53% Glycidether 100 in Methylnadic anhydride, $C_{10}H_{10}O_3$). After hardening, semithin sections (1 µm thick) were cut by a Ultramicrotome (Ultracut E from Reichert-Jung) and stained with a 4:1 solution of toluidine blue: pyronine G. Ultrathin sections (70 nm thick) were cut and mounted on Formvar coated slot grids (Plano, Wetzlar, Germany). Grids have been air dried and stained in 2% uranyl acetate and 0.5% lead citrate each for 10´. Sections were analyzed with an electron microscope (EM910, Carl Zeiss, Jena, Germany) equipped with an integrated digital camera (TRS 1K, Carl Zeiss).

1.7 Terminal dUTP nick end labeling (TUNEL)

We used the BrdU-Red DNA Fragmentation assay kit (Abcam, ab66110) for visualization of fragmentated DNA in Bergmann glia nuclei with the TUNEL method. Cryo slices from fixed cerebella (4% PA) from GFAP-EGFP expressing mice were permeabilized overnight at RT with CTA (ChemiBLOCKER, Merck-Millipore) and washed thoroughly with phosphate buffer (PB). Terminal deoxynucleotidyl transferase (T*d*T) enzymes were applied with bromolated *d*UTP for 60´ at 37°C in the dark. Cells were stained with BrdU-Red (Ex/Em: 488/576 nm) labeled antibodies (30´, RT) for visualization of TUNEL signals and with TOPRO-3 (1/1000) for DNA counterstaining. Cerebellar slices were imaged with confocal microscopy within 180´ after staining procedure. All data points in Fig. 5E represent mean values obtained from individual animals.

1.8 Western blot analyses

To quantify relative protein expression levels of the Bergmann glial marker proteins GLAST (glutamate-aspartate transporter), S100β, and BLBP (brain lipid binding protein, Supplementary Fig. 4), we performed western blots from whole cerebellar lysates. Briefly, 3-4 mice were decapitated and their cerebella were homogenized and centrifuged (4°C) at 100,000 g (45´). Supernatant and pellet were separated and individual processed and run on SDS-PAGEs. Transfer of proteins to PVDF membrane was achieved on a Semi-dry blotter (V20-SDB, Scie-Plas) and proteins were visualized with antibodies listed in Supplementary Table 2. Blots were analyzed with Fiji (NIH, USA).

1.9 Analysis of Purkinje neuron spiking and spike pauses

Mean CV2 values from Purkinje neuron spiking activity were calculated using the following equation (Holt *et al.*, 1996):

$$\text{mean of ISI CV2} = \frac{1}{n}\sum_{i=1}^{n} 2 \cdot \frac{|\text{ISI}_{i+1} - \text{ISI}_i|}{(\text{ISI}_{i+1} + \text{ISI}_i)} \quad \text{(Eq. 3).}$$

Interspike intervals (ISIs) in burst plots (Fig. 6B and D) are shaded according to their temporary non-averaged CV2 values during ISI_i to ISI_{i+1}. We defined burst initiation and termination by the lengths of the preceding and successive ISIs, respectively, corrected for the spike activity of each analyzed cell. An ISI of at least the mean ISI + 3σ in each cell was defined as a gap between bursts. Purkinje neuron spiking frequencies were determined within these individual bursts (Fig. 6). CF pauses were evoked by brief (200 ms) pressure ejections of bath solution supplemented with 1 mM Na-glutamate to molecular layer areas (Fig. 7), distal to the Purkinje cell layer with approximately 50−75 µm distance to Purkinje cell somata (PDES-DXH: npi electronic GmbH, 71732 Tamm, Germany). The recovery times were defined as the silent periods between glutamate puffs, and induced bursting activity and recovery of pre-puff simple spike activity. All data points in Fig. 6 and Fig. 7 represent mean values obtained from individual animals.

1.10 Quantification of cerebellar degeneration in old animals

Paraffinated cerebella ($n = 10/10$ animals, WT/Mut, five males and five females for both genotypes) were placed on a grid surface (grid size: 0.25 mm^2) and the dorsal surfaces were measured (Fiji Software, National Institutes of Health, USA). Degeneration in sliced vermis sections was quantified by estimating sagittal area sizes ($n = 4/4$ animals, WT/Mut) after Nissl staining for the white matter, granule cell layer, and molecular layer areas (Fig. 8).

1.11 Analysis of molecular layer width and Purkinje neuron numbers

The thickness of molecular layers was measured with Fiji (ImageJ) in the same regions ($n = 3\text{-}10/4\text{-}14$, WT/Mut) as indicated in Supplementary Fig. 8A. The numbers of Purkinje neurons in younger animals (P27−60) were counted in the internal/external vermal areas $\mathrm{V/VI}_{int}$, VI_{ext}, $\mathrm{IX/X}_{int}$, and X_{ext} and given as numbers of identified Purkinje neurons per 100 µm length of the Purkinje neuron layer ($n = 3\text{-}10/4\text{-}11$ animals, WT/Mut (Supplementary Fig. 8B).

1.12 Supplementary References

Curzon P, Zhang, M., Radek, R.J., Fox, G. B. The Behavioral Assessment of Sensorimotor Processes in the Mouse: Acoustic Startle, Sensory Gating, Locomotor Activity, Rotarod, and Beam Walking. In: Buccafusco JJ, editor. *Methods of Behavior Analysis in Neuroscience 2nd edition.* Boca Raton (FL); 2009: 146.

Guyenet SJ, Furrer SA, Damian VM, Baughan TD, La Spada AR, Garden GA. A simple composite phenotype scoring system for evaluating mouse models of cerebellar ataxia. *J Vis Exp* 2010, 39.

Holt GR, Softky WR, Koch C, Douglas RJ. Comparison of discharge variability in vitro and in vivo in cat visual cortex neurons. *J Neurophysiol* 1996; 75(5): 1806-14.

Jankowski J, Miething A, Schilling K, Baader SL. Physiological purkinje cell death is spatiotemporally organized in the developing mouse cerebellum. *Cerebellum* 2009; 8(3): 277-90.

Kaplan EL, Meier, P. Nonparametric estimation from incomplete observations. *J Am Ass* 1958; 53: 34.

Miething A. Ultrathin sectioning of different areas of the same semithin section. *Microscopy Res Techniq* 1992; 21(1): 73-4.

Paul CA, Beltz B, Berger-Sweeney J. The nissl stain: A stain for cell bodies in brain sections. *CSH Protoc* 2008, prot 4806.

van Abeelen JH, Schoones AH. Ontogeny of behavior in two inbred lines of selected mice. *Dev Psychobiol* 1977; 10(1): 17-23.

2. Supplementary Tables

2.1 Supplementary Table 1:

Score sheet and stop criteria for breeding and animal experiments for mouselines *Slc1a3*^{tm1P290RCfa} (KI P290R Slc1a3) and *Slc1a3*^{tm1Kta} (GLAST KO).

Observation:	**Score**
1. Body weight:	
correlates with mean body weight of particular age	**0**
decrease: ≤ 5% of mean body weight of particular age	**1**
decrease: 5 – 10% of mean body weight of particular age	**2**
decrease: 11 – 20% of mean body weight of particular age	**3**
decrease: >20% of mean body weight of particular age	**4**
2. General condition:	
smooth and glossy fur; clean orifices of the body, clear, glossy eyes,	**0**
defects in fur (overwhelming or reduced grooming)	**1**
unordered and or dead fur, impure orifices of the body	**2**
dead/impure fur, clotted orifices of the body, dreary eyes	**3**
clear breath sounds, animal feel cold, seizures	**4**
3. Spontaneous behavior	
Normal behavior (animal react on blowing/touches), normal social contacts.	**0**
slight problems in motor coordination, temporary tremor, normal social contacts	**1**
limited motor coordination, clear, rare rearing and climbing	**2**
Isolation, lethargy and curved posture	**3**
Isolation, lethargy and curved posture with frequent seizures (>1/8h) or longer than 2´	**4**
4. Symptomatik (Episodic ataxia)	
no symptoms	**0**
Slight ataxia, food and water is reached easily, temporary tremor	**1**
clear ataxia, tremor and short focal seizures, w/o loss of righting reflex, frequency <1/8h, food and water is consumed	**2**
Heavy ataxia, short focal seizures, w/o loss of righting reflex (<2/8h), with relaxing phase.	**3**
Heavy ataxia with frequent focal seizures and loss of righting reflex for >2´ or frequency of seizures >1/day	**4**

2.2 Supplementary Table 2

Target	full name	host	RRID	Use/dilution	Supplier
1st antibodies					
BLBP	brain lipid binding protein	*rb*	AB_10000325	1:200	MerckMillipore, Germany
CASP3	active caspase-3	*rb*	AB_302962	1:20	Abcam, UK
GAD65/67	glutamate decarboxylase 65/67	*rb*	AB_477019	1:5,000	Sigma, Germany
GFAP	glial fibrillary acidic protein	*ms*	AB_477010	1:800	Sigma, Germany
GLAST	glutamate aspartate transporter	*ms*	AB_10829302	1:500	Milteniy, Biotec, Germany
GLUR1	glutamate receptor 1	*gt*	AB_641039	1:100	Santa Cruz, USA
GLUR2	glutamate receptor 2	*rb*	AB_2313803	1:100	MerckMillipore, Germany
NeuN	neuronal nuclei	*rb*	AB_104225	1:400	Abcam, UK
S100	S100β	*ms*	AB_301508	1:100	Abcam, UK
VGLUT1	vesicular glutamate transporter 1	*ms*	AB_887875	1:100	Synaptic Systems, Germany
VGLUT2	vesicular glutamate transporter 2	*gp*	AB_2301731	1:10,000	Merck-Millipore, Germany
2nd antibodies					
Cy2	cyanidin 2-conjugated antibody	*d@rb*	AB_2340612	1:400	Dianova, Germany
Cy2	cyanidin 2-conjugated antibody	*d@gt*	AB_2307341	1:400	Dianova, Germany
Cy2	cyanidin 2-conjugated antibody	*d@ms*	AB_2340827	1:400	Dianova, Germany
Cy3	cyanidin 3-conjugated antibody	*d@gp*	AB_2340460	1:800	Dianova, Germany
Cy5	cyanidin 5-conjugated antibody	*d@ms*	AB_2340813	1:400	Dianova, Germany
Cy5	cyanidin 5-conjugated antibody	*d@rb*	AB_2340607	1:400	Dianova, Germany
Assay					
TOPRO-3	TOPRO-3		No. T3605	1:1,000	Invitrogen, Germany
TUNEL Labeling Kit - BrDU-Red (DNA fragmentation)			No. ab66110	NA	Abcam, UK

rb - rabbit; *ms* - mouse; *gt* - goat; *gp* - guinea pig; *d* - donkey
RRID Portal (Resource identification portal): *https://scicrunch.org/resources*

2.3 Supplementary Table 3: *P-values for Figures*

Figure 1C (median paw slips per step during the ledgetests)

2-way ANOVA	Significance α = 0.05/0.1?	Summary	*P*-value$^{\text{Holm-Sidak}}$
WT::P290R/+	YES	***	<0.001
WT: ♂::♀	NO	*n.s.*	0.441
P290R/+: ♂::♀	NO	*n.s.*	0.124
♂: WT::P290R/+	YES	***	<0.001
♀: WT::P290R/+	YES	***	<0.001

Figure 1E (mean frequencies of spin failures on the rotarod)

2-*way* ANOVA$^{\textit{repeated measures}}$	Significance α = 0.05/0.1?	Summary	P-value$^{\textit{Holm-Sidak}}$
WT::P290R/+ $^{\textit{Trial I}}$	YES	***	<0.001
WT::P290R/+ $^{\textit{Trial II}}$	YES	**	0.005
WT::P290R/+ $^{\textit{Trial III}}$	NO/YES	*n.s.*	0.097

Calculation was performed using average latencies of individual animals from the three trials, respectively

Figure 1F (median rotarod latencies)

2-*way* ANOVA$^{\textit{repeated measures}}$	Significance α = 0.05/0.1?	Summary	P-value$^{\textit{Holm-Sidak}}$
WT::P290R/+ $^{\textit{Trial I}}$	YES	**	0.01
WT::P290R/+ $^{\textit{Trial II}}$	YES	*	0.031
WT::P290R/+ $^{\textit{Trial III}}$	NO	*n.s.*	0.359

Calculation was performed using average latencies of individual animals from the three trials, respectively

Figure 2B (mean numbers of GFAP fibers per 100 µm PCL in region V/VI)

2-way ANOVA	Significance α = 0.05/0.1?	Summary	*P*-value$^{\text{Holm-Sidak}}$
WT::P290R/+ (Age 1)	NO	*n.s.*	0.784
WT::P290R/+ (Age 2)	YES	*	0.012
WT::P290R/+ (Age 3)	NO	*n.s.*	0.371
WT::P290R/+ (Age 4)	YES	**	0.005
WT::P290R/+ (Age 5)	YES	***	<0.001
WT::P290R/+ (Age 6)	YES	***	<0.001
WT::P290R/+ (Age 7)	YES	***	<0.001
WT::P290R/+ (Age 8)	YES	***	<0.001

Figure 2B (mean numbers of GFAP fibers per 100 µm PCL in region IX/X)

2-way ANOVA	Significance α = 0.05/0.1?	Summary	*P*-value$^{\text{Holm-Sidak}}$
WT::P290R/+ (Age 1)	NO	*n.s.*	0.795
WT::P290R/+ (Age 2)	NO/YES	*n.s.*	0.099
WT::P290R/+ (Age 3)	NO	*n.s.*	0.318
WT::P290R/+ (Age 4)	YES	*	0.018
WT::P290R/+ (Age 5)	YES	***	<0.001
WT::P290R/+ (Age 6)	YES	***	<0.001
WT::P290R/+ (Age 7)	YES	***	<0.001
WT::P290R/+ (Age 8)	YES	***	<0.001

Age groups: P5-6 (1), P8-9 (2), P10 (3), P11-12 (4), P15-20 (5), P24-P35 (6), P45-65 (7), P538-P950 (8)

Figure 2C (median BGC$^+$ cells/100 µm PCL in region V/VI)

2-way ANOVA	Significance α = 0.05/0.1 ?	Summary	*P*-value$^{\text{Holm-Sidak}}$
WT::P290R/+ (PCL)	YES	***	<0.001
WT::P290R/+ (ectopic)	NO	*n.s.*	0.185

Figure 2C (median BGC$^+$cells/100 µm PCL in region IX/X)

2-way ANOVA	Significance α = 0.05/0.1 ?	Summary	*P*-value$^{\text{Holm-Sidak}}$
WT::P290R/+ (PCL)	YES	***	<0.001
WT::P290R/+ (ectopic)	NO	*n.s.*	0.298

Figure 2F (median NeuN$^+$ cells /mm^2)

2-way ANOVA	Significance α = 0.05/0.1 ?	Summary	*P*-value$^{\text{Holm-Sidak}}$
WT::P290R/+ (P20–P40)	YES	**	0.002
WT::P290R/+ (P41-100)	YES	*	0.025
WT::P290R/+ (>P100)	YES	***	0.001

Figure 2G (median GFAP$^+$ cells/mm^2)

2-way ANOVA	Significance α = 0.05/0.1 ?	Summary	*P*-value$^{\text{Holm-Sidak}}$
WT::P290R/+ (P20–P40)	NO/YES	*n.s.*	0.093
WT::P290R/+ (P41–100)	NO	*n.s.*	0.121
WT::P290R/+ (>P100)	YES	**	0.002

Figure 3B (median VGLUT1$^+$ clusters /100 µm^2)

2-way ANOVA	Significance $\alpha = 0.05/0.1$?	Summary	P-value$^{\text{Holm-Sidak}}$
WT::P290R/+ (V/VI)	YES	***	<0.001
WT::P290R/+ (VI)	YES	**	0.006
WT::P290R/+ (IX/X)	YES	**	0.003
WT::P290R/+ (X)	YES	***	<0.001

Figure 3C (median VGLUT2$^+$ clusters /100 µm^2)

2-way ANOVA	Significance $\alpha = 0.05/0.1$?	Summary	P-value$^{\text{Holm-Sidak}}$
WT::P290R/+ (V/VI)	YES	***	<0.001
WT::P290R/+ (VI)	YES	*	0.049
WT::P290R/+ (IX/X)	YES	***	<0.001
WT::P290R/+ (X)	YES	*	0.015

Figure 3D (median GAD65/67$^+$ clusters /100 µm^2)

2-way ANOVA	Significance $\alpha = 0.05/0.1$?	Summary	P-value$^{\text{Holm-Sidak}}$
WT::P290R/+ (V/VI)	YES	*	0.046
WT::P290R/+ (VI)	NO	*n.s.*	0.123
WT::P290R/+ (IX/X)	NO	*n.s.*	0.595
WT::P290R/+ (X)	NO	*n.s.*	0.867

Figure 4A (mean current amplitudes, pA)

U-test	Significance $\alpha = 0.05/0.1$?	Summary	*P*-value
WT::P290R/+	YES	*	0.024

Figure 4C (normalized current amplitudes at -100/-120 mV, pA)

2-way ANOVA(repeated measures)	Significance $\alpha = 0.05/0.1$?	Summary	*P*-value
WT::P290R/+ (-100 mV)	YES	*	0.025
WT::P290R/+ (-120 mV)	YES	*	0.017
WT, -80 mV::-100/120 mV	NO/NO	*n.s./n.s.*	0.628/0.282
P290R/+, -80 mV::-100/-120 mV	YES/YES	*/**	0.024/0.004

Figure 4E (Comparisons WT :: P290R: [Cl$^-$]$_{int}$, mM)

2-way **ANOVA**	Significance $\alpha = 0.05/0.1$?	Summary	*P*-value$^{\text{Holm-Sidak}}$
WT::P290R/+ (P4-7)	YES	***	<0.001
WT::P290R/+(P8-10)	YES	***	<0.001
WT::P290R/+(P11-12)	YES	***	<0.001
WT::P290R/+(P13-15)	NO/YES	*n.s.*	0.09

Figure 4 F (Comparisons WT :: P290R+UCPH101: [Cl$^-$]$_{int}$, mM)

1-way **ANOVA on ranks**	Significance $\alpha = 0.05$?	Summary	Dunn´s test
WT::P290R/+(P4-12)	YES	***	YES
WT::WT-P290R/+$^{\text{UCPH}}$(P4-12)	NO	*n.s.*	NO

1-way ANOVA on ranks WT::P290R/+: $P < 0.001$

Figure 5B (left, total apoptotic events)

2-way ANOVA	Significance α = 0.05/0.1 ?	Summary	*P*-value$^{\text{Holm-Sidak}}$
WT::P290R/+ (P8-9)	NO/YES	*n.s.*	0.074
WT::P290R/+ (P10)	YES	**	0.008
WT::P290R/+ (P11)	YES	*	0.043
WT::P290R/+ (P12)	YES	*	0.015
WT::P290R/+ (P13)	NO/YES	*n.s.*	0.073
WT::P290R/+ (P14-15)	NO	*n.s.*	0.56

Figure 5B (right, colocalized GFAP-EGFP/CASP3 signals)

2-way ANOVA	Significance α = 0.05/0.1 ?	Summary	*P*-value$^{\text{Holm-Sidak}}$
WT::P290R/+ (P8-9)	NO/YES	*n.s.*	0.056
WT::P290R/+ (P10)	YES	*	0.038
WT::P290R/+ (P11)	YES	***	<0.001
WT::P290R/+ (P12)	YES	***	<0.001
WT::P290R/+ (P13)	YES	*	0.045
WT::P290R/+ (P14-15)	NO	*n.s.*	0.369

Figure 5E, (*left*, colocalized GFAP-EGFP/TUNEL signals)

1-way ANOVA on ranks	Significance α = 0.05/0.1 ?	Summary	Dunn´s test
WT::P290R/+ (P9-14)	YES	***	YES

1-way ANOVA on ranks WT::P290R/+: *P* = 0.001

Figure 5E, *right* (total apoptosis events, TUNEL signals)

1-way ANOVA on ranks	Significance α = 0.05/0.1 ?	Summary	Dunn´s test
WT::P290R/+ (P9-14)	YES	**	YES

1-way ANOVA on ranks WT::P290R/+: *P* = 0.005

Figure 6E (spiking frequencies of PCs, Hz)

2-way ANOVA	Significance $\alpha = 0.05/0.1$?	Summary	*P*-value$^{\text{Holm-Sidak}}$
WT::P290R/+ (P10)	NO	*n.s.*	0.331
WT::P290R/+ (P20–30)	NO	*n.s.*	0.442
WT::P290R/+ (P40)	YES	***	<0.001

Figure 6F (covariances of PC spiking, CV)

2-way ANOVA	Significance $\alpha = 0.05/0.1$?	Summary	*P*-value$^{\text{Holm-Sidak}}$
WT::P290R/+ (P10)	NO	*n.s.*	0.24
WT::P290R/+ (P20–30)	NO	*n.s.*	0.685
WT::P290R/+ (P40)	NO	*n.s.*	0.348

Figure 6G (covariances of PC spiking, mCV2)

2-way ANOVA	Significance $\alpha = 0.05/0.1$?	Summary	*P*-value$^{\text{Holm-Sidak}}$
WT::P290R/+ (P10)	NO	*n.s.*	0.242
WT::P290R/+ (P20–30)	NO	*n.s.*	0.605
WT::P290R/+ (P40)	NO	*n.s.*	0.383

Figure 7C (CF-pauses of PCs, s)

U-test	Significance $\alpha = 0.05/0.1$?	Summary	*P*-value
WT::P290R/+	YES	*	$P = 0.014$

Figure 8B (transversal cerebellar areas, mm^2)

2-way ANOVA	Significance α = 0.05/0.1 ?	Summary	*P*-value$^{\text{Holm-Sidak}}$
WT$^{♂}$::P290R/+$^{♂}$ (H_l)	NO/YES	*n.s.*	0.077
WT$^{♂}$::P290R/+$^{♂}$ (H_r)	NO	*n.s.*	0.177
WT$^{♂}$::P290R/+$^{♂}$ (V_a)	YES	*	0.032
WT$^{♂}$::P290R/+$^{♂}$ (V_p)	YES	***	<0.001
Σ WT$^{♂}$::P290R/+$^{♂}$	**YES**	**	**0.005**
WT$^{♀}$::P290R/+$^{♀}$ (H_l)	YES	***	<0.001
WT$^{♀}$::P290R/+$^{♀}$ (H_r)	YES	***	<0.001
WT$^{♀}$::P290R/+$^{♀}$ (V_a)	YES	**	0.004
WT$^{♀}$::P290R/+$^{♀}$ (V_p)	YES	***	0.001
Σ WT$^{♀}$::P290R/+$^{♀}$	**YES**	***	**<0.001**

(H_l: left hemisphere; H_r: right hemisphere; V_a: anterior vermis; V_p: posterior vermis)

Figure 8D (sagittal cerebellar areas, vermis, mm^2)

2-way ANOVA	Significance α = 0.05/0.1 ?	Summary	*P*-value$^{\text{Holm-Sidak}}$
WT::P290R/+ (*WM*)	NO	*n.s.*	0.154
WT::P290R/+ (*GCL*)	YES	***	<0.001
WT::P290R/+ (*ML*)	YES	***	<0.001
Σ WT::P290R/+ (*Vermis*)^{t}	**YES**	**	**0.002**

(WM: white matter; GCL: granule cell layer; ML: molecular layer)

Supplementary Figure 3B (latencies to first error, s)

2-way ANOVA (*repeated measures)*	Significance α = 0.05/0.1 ?	Summary	P-value$^{\text{Holm-Sidak}}$
WT::P290R/+ $^{\textit{Trial I}}$	YES	*	0.01
WT::P290R/+ $^{\textit{Trial II}}$	YES	**	0.005
WT::P290R/+ $^{\textit{Trial III}}$	YES	**	0.004

Supplementary Figure 4D (relative protein expression, normalized)

2-way ANOVA	Significance α = 0.05/0.1 ?	Summary	*P*-value$^{\text{Holm-Sidak}}$
WT::P290R/+ (BLBP)	YES	**	0.004
WT::P290R/+ (S100β)	YES	**	0.007
WT::P290R/+ (GLAST)	YES	***	<0.001

Supplementary Figure 8A (width of ML, µm)

2-way ANOVA	Significance α = 0.05/0.1 ?	Summary	P-value$^{\text{Holm-Sidak}}$
WT::P290R/+ VI$_{int}$	NO	*n.s.*	0.226
WT::P290R/+ VI$_{ext}$	NO	*n.s.*	0.524
WT::P290R/+ X$_{int}$	NO	*n.s.*	0.880
WT::P290R/+ X$_{ext}$	YES	*	0.041

Supplementary Figure 8B (number of PCs, N/100 µm PCL)

2-way ANOVA	Significance α = 0.05/0.1 ?	Summary	P-value$^{\text{Holm-Sidak}}$
WT::P290R/+ VI$_{int}$	NO	*n.s.*	0.884
WT::P290R/+ VI$_{ext}$	YES	**	0.003
WT::P290R/+ X$_{int}$	NO	*n.s.*	0.340
WT::P290R/+ X$_{ext}$	NO	*n.s.*	0.233

Supplementary Material

for

Increased glutamate transporter-associated anion currents cause glial apoptosis in episodic ataxia 6

Peter Kovermann[1], Verena Untiet[1,3], Yulia Kolobkova[1], Miriam Engels[1], Stephan Baader[2], Karl Schilling[2], and Christoph Fahlke[1]

[1]Institut für Biologische Informationsprozesse, Molekular- und Zellphysiologie (IBI-1), Forschungszentrum Jülich, 52425 Jülich, Germany

[2]Anatomisches Institut, Rheinische Friedrich-Wilhelm-Universität, 53115 Bonn, Germany

[3]Center for Translational Neuromedicine, Københavns Universitet, 2200 København N, Denmark

Table of content for Supplementary Methods and Tables:

1. Supplementary Methods

2. Supplementary Tables

1. Supplementary Methods

1.1 Transgenic animals

Knock-in *Slc1a3*^{tm1P290RCfa} (*Slc1a3*$^{P290R/+}$) mice were generated by site-directed mutagenesis using a mutant *Slc1a3* allele located on chromosome 15 (at 3.82 cM) and encoding a P290R substitution in exon 7. Briefly, a fragment covering exons 4–8 of the *Slc1a3* locus was subcloned and the P290R sequence (agg to gcg) was inserted via PCR synthesis into the end of exon 7 (Polygene Transgenetics, Switzerland). Positive clones were injected into blastocysts from C57BL/6N mice, and surviving blastocysts were the transferred to a CD–1 foster mouse. Germline chimeric foster mice were crossbred with C57BL/6N-derived FLP-deleter mice (B6;SJL-Tg(ACTFLPe)9205Dym/J; JANVIER LABS, France) to excise the neomycin cassette (Supplementary Fig. 1). Since mortality of C57BL/6 knock-in mice prevented successful breeding, we backcrossed the mutation into the more robust mouse strain 129/SvJ (Taconic Biosciences GmbH, Germany) for 10 generations. The animals were housed under standard conditions in the animal facility of Forschungszentrum Jülich according to institute guidelines under a 12 h light/dark cycle (light: 6:00am–6:00pm). Animal testing was done during the light phase. All experiments complied with the German Law for the Protection of Animals and were approved by the Forschungszentrum Jülich and LANUV (State Agency for Nature, Environment and Consumer Protection) of North Rhine-Westphalia (reference nos 84–02.04.2014.A334/A335, to P.K.). The health status of mutant animals was continuously monitored, and animals were treated in strict accordance with defined stop criteria (Supplementary Table 1).

1.2 Analysis of motor coordination of transgenic mice

Motor coordination of transgenic animals was tested with two different tests. We used ledge tests (Guyenet *et al.*, 2010) to test the behavior of animals on a narrow path.

Animals were placed on a 1 cm wide ledge and the test were video-recorded for analysis. Mice younger than postnatal day 30 (P30) were not subjected to the test because they tended be more active (e.g. jumpiness) (van Abeelen and Schoones, 1977; Curzon, 2009). The mean stumble ratio was calculated from the video recordings as the average error rate for each animal during all traverses across the ledge using the equation:

$$\boldsymbol{stumble\ ratio} = \frac{\sum_{1}^{n}\left(\mathrm{N}_{\mathrm{failures}} \cdot \mathrm{N}_{\mathrm{steps}}^{-1}\right)_{1}}{\mathrm{n}} \text{(Eq. 1).}$$

n = number of traverses (2´); $\mathrm{N}_{\mathrm{failures}}$ = number of paw slips/traverse; $\mathrm{N}_{\mathrm{steps}}$ = number of steps/traverse.

Mice were as well subjected to another test of motor coordination, the rotarod test. This test measures the time until an animal falls from a rotating rod. The rotarod sessions were video-recorded and then analyzed by latencies to fall and counting spin failures. For each fall event, the remaining score (time in sec) was subtracted from the starting value of 600 (~ test period: 600 s), and the resulting value was corrected for spin failures (Supplementary Fig. 3) by subtracting three points for each missed cycle. Spin failure frequencies for WT and mutant mice were calculated from the number of spin failures during latency to fall. We assumed a lower limit of 1/600 s (≈0.0017 Hz, Fig. 1E). In initial tests we observed that mutant males increase their latency to fall from the rod via excessive spin failures, preventing an appropriate comparison of WT and mutant mice. We therefore excluded males from rotarod tests. Time series data of rotarod tests were averaged and transformed into survival plots (Kaplan, 1958), and corrected latencies were added as box plots (Fig. 1D and F). Blinding and randomization was not possible because of the severe phenotype of mutant animals. The State Agency for Nature, Environment and Consumer Protection of North Rhine-Westphalia (reference nos 84–02.04.2014.A334/A335, to P.K.) ordered permanent observation of transgenic mice during breeding and maintenance. Tests were always performed with all litters, the group sizes were determined by genotype frequency (50:50). All data points in Fig. 1C, and F represent mean values obtained from individual animals during 3 trials per session.

1.3 Visualization and quantification of specific cell types and components

Mice were anesthetized with isoflurane (Piramal Healthcare, UK) and decapitated. The cerebella were excised, transferred to 4% paraformaldehyde (PFA, $[CH_2O]_n$) in phosphate buffer (PB; in mM, 81 $NaH_2PO_4 \cdot 2H_2O$, 9 $Na_2HPO_4H_2O$, pH 7.4), and stored in fixative for 5 days (at 4 °C). After dehydration in a graded ethylalcohol series (50%, 70%, 90%, 100% EtOH) brains were embedded in paraffin and sagittal sections (5 µm or 7 µm thick) were cut for immunostainings. Nissl staining was performed as previously described (Paul *et al*, 2008). For immunostaining, endogenous peroxidases were inactivated (in mM, 21 $C_6H_8O_7$ and 6 Na_2HPO_4, 15% (v/v) H_2O_2 for 15´, at RT), and epitopes were unmasked (2000 Tris and 63 EDTA, pH 8.0, at 100 °C for 20´) and blocked overnight (bovine serum albumin 1% (w/v) in PB, at 4 °C). Sections were incubated for 1-2 days with primary and 45-60´with secondary antibodies diluted in CTA (i.e. 5%ChemiBLOCKER, Merck–Millipore, in PB containing 1% Triton-X100 and 0.05% NaN_3) and 1% Triton-X100. For visualization, sections were incubated in cyanine-dye conjugated secondary antibodies for 60´ at room temperature (RT). A list of all used antibodies is given in in Supplementary Table 2. Fiber or cell numbers in WT and mutant cerebella was counted in sagittal vermis sections (lobes V/VI and IX/X). Bergmann glia cells were quantified by counting the number of $GFAP^{positive}$ fibers in the molecular layer (ML) and the density of neurons or astrocytes by counting the number of $NeuN^{positive}$ cells or $GFAP^{positive}$ cells with a typical multipolar astrocyte shape in defined areas.

1.4 Quantification of Bergmann glia cells

We immunostained paraffin slices (4 µm) from mice cerebella with typical astrocytic and Bergmann glial markers as brain lipid binding protein (BLBP), the Ca^{2+} binding protein S100β, and glutamate-aspartate transporter (GLAST) and counterstained nuclei with TOPRO-3 for confocal microcopy. Bergmann glial cell somata in the Purkinje cell layer (PCL) and ectopic glia in the molecular layer (ML, lobes V/VI and IX/X) were counted separately. Cell numbers are provided as mean numbers of Bergmann glia per 100 µm length (PCL or ML) from individual animals.

1.5 Quantification of glutamatergic and GABAergic synapses in the molecular layer

To determine the number of synapses in the cerebellar molecular layer, paraffin slices were incubated overnight with a combination of primary antibodies against vesicular glutamate transporter 1, vesicular glutamate transporter 2, and anti-glutamate decarboxylase 65/67 and subsequently in cyanine-dye conjugated secondary antibodies from donkey for 60´ at RT. Densities of synapses were quantified by counting $VGLUT1^{positive}$, $VGLUT2\text{-}^{positive}$ and $GAD65/67^{positive}$ signals within single confocal planes in randomly selected areas of different sizes of V/VI_{int}, VI_{ext}, IX/X_{int}, and X_{ext}. Synapse density was calculated in *n* = 3-5/4-9 (WT/Mut) mice from means of *n* = 144/212 (WT/Mut) test areas. Densities are given as boutons per 100 μm^2.

1.6 Transmission electron microscopy

Electron microscopical pictures (Supplementary Fig. 7) were prepared as described previously (Miething, 1992; Jankowski *et al.*, 2009). Briefly, mice were perfused with Karnovsky solution (3% PFA), 3% glutaraldehyde ($C_5H_8O_2$), in phosphate buffered saline containing 10 mM $NaH_2PO_4 \cdot H_2O$ and 150 mM NaCl, pH 7.2) and dissected cerebella were immersed in the same fixative for 6 h. Tissue blocks (1 mm thick) were cut and incubated in 1% Osmiumtetroxid (OsO_4) at RT for 120´. Sections were then dehydrated and embedded in Epon 812 using a 3:2 mixture of Epon A (38% Glycidether 100 in 2-Dodecenylsuccinic acid anhydride, $C_{16}H_{26}O_3$) and Epon B (53% Glycidether 100 in Methylnadic anhydride, $C_{10}H_{10}O_3$). After hardening, semithin sections (1 µm thick) were cut by a Ultramicrotome (Ultracut E from Reichert-Jung) and stained with a 4:1 solution of toluidine blue: pyronine G. Ultrathin sections (70 nm thick) were cut and mounted on Formvar coated slot grids (Plano, Wetzlar, Germany). Grids have been air dried and stained in 2% uranyl acetate and 0.5% lead citrate each for 10´. Sections were analyzed with an electron microscope (EM910, Carl Zeiss, Jena, Germany) equipped with an integrated digital camera (TRS 1K, Carl Zeiss).

1.7 Terminal dUTP nick end labeling (TUNEL)

We used the BrdU-Red DNA Fragmentation assay kit (Abcam, ab66110) for visualization of fragmentated DNA in Bergmann glia nuclei with the TUNEL method. Cryo slices from fixed cerebella (4% PA) from GFAP-EGFP expressing mice were permeabilized overnight at RT with CTA (ChemiBLOCKER, Merck-Millipore) and washed thoroughly with phosphate buffer (PB). Terminal deoxynucleotidyl transferase (T*d*T) enzymes were applied with bromolated *d*UTP for 60´ at 37°C in the dark. Cells were stained with BrdU-Red (Ex/Em: 488/576 nm) labeled antibodies (30´, RT) for visualization of TUNEL signals and with TOPRO-3 (1/1000) for DNA counterstaining. Cerebellar slices were imaged with confocal microscopy within 180´ after staining procedure. All data points in Fig. 5E represent mean values obtained from individual animals.

1.8 Western blot analyses

To quantify relative protein expression levels of the Bergmann glial marker proteins GLAST (glutamate-aspartate transporter), S100β, and BLBP (brain lipid binding protein, Supplementary Fig. 4), we performed western blots from whole cerebellar lysates. Briefly, 3-4 mice were decapitated and their cerebella were homogenized and centrifuged (4°C) at 100,000 g (45´). Supernatant and pellet were separated and individual processed and run on SDS-PAGEs. Transfer of proteins to PVDF membrane was achieved on a Semi-dry blotter (V20-SDB, Scie-Plas) and proteins were visualized with antibodies listed in Supplementary Table 2. Blots were analyzed with Fiji (NIH, USA).

1.9 Analysis of Purkinje neuron spiking and spike pauses

Mean CV2 values from Purkinje neuron spiking activity were calculated using the following equation (Holt *et al.*, 1996):

$$\mathbf{mean\ of\ ISI\ CV2} = \frac{1}{n}\sum_{i=1}^{n} 2 \cdot \frac{|\mathrm{ISI}_{i+1} - \mathrm{ISI}_{i}|}{(\mathrm{ISI}_{i+1} + \mathrm{ISI}_{i})} \text{(Eq. 3).}$$

Interspike intervals (ISIs) in burst plots (Fig. 6B and D) are shaded according to their temporary non-averaged CV2 values during ISI_i to ISI_{i+1}. We defined burst initiation and termination by the lengths of the preceding and successive ISIs, respectively, corrected for the spike activity of each analyzed cell. An ISI of at least the mean ISI + 3σ in each cell was defined as a gap between bursts. Purkinje neuron spiking frequencies were determined within these individual bursts (Fig. 6). CF pauses were evoked by brief (200 ms) pressure ejections of bath solution supplemented with 1 mM Na-glutamate to molecular layer areas (Fig. 7), distal to the Purkinje cell layer with approximately 50−75 µm distance to Purkinje cell somata (PDES-DXH: npi electronic GmbH, 71732 Tamm, Germany). The recovery times were defined as the silent periods between glutamate puffs, and induced bursting activity and recovery of pre-puff simple spike activity. All data points in Fig. 6 and Fig. 7 represent mean values obtained from individual animals.

1.10 Quantification of cerebellar degeneration in old animals

Paraffinated cerebella (*n* = 10/10 animals, WT/Mut, five males and five females for both genotypes) were placed on a grid surface (grid size: 0.25 mm^2) and the dorsal surfaces were measured (Fiji Software, National Institutes of Health, USA). Degeneration in sliced vermis sections was quantified by estimating sagittal area sizes (*n* = 4/4 animals, WT/Mut) after Nissl staining for the white matter, granule cell layer, and molecular layer areas (Fig. 8).

1.11 Analysis of molecular layer width and Purkinje neuron numbers

The thickness of molecular layers was measured with Fiji (ImageJ) in the same regions (*n* = 3-10/4-14, WT/Mut) as indicated in Supplementary Fig. 8A. The numbers of Purkinje neurons in younger animals (P27−60) were counted in the internal/external vermal areas V/VI_{int}, VI_{ext}, IX/X_{int}, and X_{ext} and given as numbers of identified Purkinje neurons per 100 µm length of the Purkinje neuron layer (*n* = 3-10/4-11 animals, WT/Mut (Supplementary Fig. 8B).

1.12 Supplementary References

Curzon P, Zhang, M., Radek, R.J., Fox, G. B. The Behavioral Assessment of Sensorimotor Processes in the Mouse: Acoustic Startle, Sensory Gating, Locomotor Activity, Rotarod, and Beam Walking. In: Buccafusco JJ, editor. *Methods of Behavior Analysis in Neuroscience 2nd edition.* Boca Raton (FL); 2009: 146.

Guyenet SJ, Furrer SA, Damian VM, Baughan TD, La Spada AR, Garden GA. A simple composite phenotype scoring system for evaluating mouse models of cerebellar ataxia. *J Vis Exp* 2010, 39.

Holt GR, Softky WR, Koch C, Douglas RJ. Comparison of discharge variability in vitro and in vivo in cat visual cortex neurons. *J Neurophysiol* 1996; 75(5): 1806-14.

Jankowski J, Miething A, Schilling K, Baader SL. Physiological purkinje cell death is spatiotemporally organized in the developing mouse cerebellum. *Cerebellum* 2009; 8(3): 277-90.

Kaplan EL, Meier, P. Nonparametric estimation from incomplete observations. *J Am Ass* 1958; 53: 34.

Miething A. Ultrathin sectioning of different areas of the same semithin section. *Microscopy Res Techniq* 1992; 21(1): 73-4.

Paul CA, Beltz B, Berger-Sweeney J. The nissl stain: A stain for cell bodies in brain sections. *CSH Protoc* 2008, prot 4806.

van Abeelen JH, Schoones AH. Ontogeny of behavior in two inbred lines of selected mice. *Dev Psychobiol* 1977; 10(1): 17-23.

2. Supplementary Tables

2.1 Supplementary Table 1:

Score sheet and stop criteria for breeding and animal experiments for mouselines *Slc1a3*^{tm1P290RCfa} (KI P290R Slc1a3) and *Slc1a3*^{tm1Kta} (GLAST KO).

Observation:	**Score**
1. Body weight:	
correlates with mean body weight of particular age	**0**
decrease: ≤ 5% of mean body weight of particular age	**1**
decrease: 5 – 10% of mean body weight of particular age	**2**
decrease: 11 – 20% of mean body weight of particular age	**3**
decrease: >20% of mean body weight of particular age	**4**
2. General condition:	
smooth and glossy fur; clean orifices of the body, clear, glossy eyes,	**0**
defects in fur (overwhelming or reduced grooming)	**1**
unordered and or dead fur, impure orifices of the body	**2**
dead/impure fur, clotted orifices of the body, dreary eyes	**3**
clear breath sounds, animal feel cold, seizures	**4**
3. Spontaneous behavior	
Normal behavior (animal react on blowing/touches), normal social contacts.	**0**
slight problems in motor coordination, temporary tremor, normal social contacts	**1**
limited motor coordination, clear, rare rearing and climbing	**2**
Isolation, lethargy and curved posture	**3**
Isolation, lethargy and curved posture with frequent seizures (>1/8h) or longer than 2´	**4**
4. Symptomatik (Episodic ataxia)	
no symptoms	**0**
Slight ataxia, food and water is reached easily, temporary tremor	**1**
clear ataxia, tremor and short focal seizures, w/o loss of righting reflex, frequency <1/8h, food and water is consumed	**2**
Heavy ataxia, short focal seizures, w/o loss of righting reflex (<2/8h), with relaxing phase.	**3**
Heavy ataxia with frequent focal seizures and loss of righting reflex for >2´ or frequency of seizures >1/day	**4**

2.2 Supplementary Table 2

Target	full name	host	RRID	Use/dilution	Supplier
1st antibodies					
BLBP	brain lipid binding protein	*rb*	AB_10000325	1:200	MerckMillipore, Germany
CASP3	active caspase-3	*rb*	AB_302962	1:20	Abcam, UK
GAD65/67	glutamate decarboxylase 65/67	*rb*	AB_477019	1:5,000	Sigma, Germany
GFAP	glial fibrillary acidic protein	*ms*	AB_477010	1:800	Sigma, Germany
GLAST	glutamate aspartate transporter	*ms*	AB_10829302	1:500	Milteniy, Biotec, Germany
GLUR1	glutamate receptor 1	*gt*	AB_641039	1:100	Santa Cruz, USA
GLUR2	glutamate receptor 2	*rb*	AB_2313803	1:100	MerckMillipore, Germany
NeuN	neuronal nuclei	*rb*	AB_104225	1:400	Abcam, UK
S100	S100β	*ms*	AB_301508	1:100	Abcam, UK
VGLUT1	vesicular glutamate transporter 1	*ms*	AB_887875	1:100	Synaptic Systems, Germany
VGLUT2	vesicular glutamate transporter 2	*gp*	AB_2301731	1:10,000	Merck-Millipore, Germany
2nd antibodies					
Cy2	cyanidin 2-conjugated antibody	*d@rb*	AB_2340612	1:400	Dianova, Germany
Cy2	cyanidin 2-conjugated antibody	*d@gt*	AB_2307341	1:400	Dianova, Germany
Cy2	cyanidin 2-conjugated antibody	*d@ms*	AB_2340827	1:400	Dianova, Germany
Cy3	cyanidin 3-conjugated antibody	*d@gp*	AB_2340460	1:800	Dianova, Germany
Cy5	cyanidin 5-conjugated antibody	*d@ms*	AB_2340813	1:400	Dianova, Germany
Cy5	cyanidin 5-conjugated antibody	*d@rb*	AB_2340607	1:400	Dianova, Germany
Assay					
TOPRO-3	TOPRO-3		No. T3605	1:1,000	Invitrogen, Germany
TUNEL Labeling Kit - BrDU-Red (DNA fragmentation)			No. ab66110	NA	Abcam, UK

rb - rabbit; *ms* - mouse; *gt* - goat; *gp* - guinea pig; *d* - donkey

RRID Portal (Resource identification portal): *https://scicrunch.org/resources*

2.3 Supplementary Table 3: *P-values for Figures*

Figure 1C (median paw slips per step during the ledgetests)

2-way ANOVA	Significance α = 0.05/0.1?	Summary	*P*-value$^{\text{Holm-Sidak}}$
WT::P290R/+	YES	***	<0.001
WT: ♂::♀	NO	*n.s.*	0.441
P290R/+: ♂::♀	NO	*n.s.*	0.124
♂: WT::P290R/+	YES	***	<0.001
♀: WT::P290R/+	YES	***	<0.001

Figure 1E (mean frequencies of spin failures on the rotarod)

2-*way* ANOVA$^{\textit{repeated measures}}$	Significance α = 0.05/0.1?	Summary	P-value$^{\textit{Holm-Sidak}}$
WT::P290R/+ $^{\textit{Trial I}}$	YES	***	<0.001
WT::P290R/+ $^{\textit{Trial II}}$	YES	**	0.005
WT::P290R/+ $^{\textit{Trial III}}$	NO/YES	*n.s.*	0.097

Calculation was performed using average latencies of individual animals from the three trials, respectively

Figure 1F (median rotarod latencies)

2-*way* ANOVA$^{\textit{repeated measures}}$	Significance α = 0.05/0.1?	Summary	P-value$^{\textit{Holm-Sidak}}$
WT::P290R/+ $^{\textit{Trial I}}$	YES	**	0.01
WT::P290R/+ $^{\textit{Trial II}}$	YES	*	0.031
WT::P290R/+ $^{\textit{Trial III}}$	NO	*n.s.*	0.359

Calculation was performed using average latencies of individual animals from the three trials, respectively

Figure 2B (mean numbers of GFAP fibers per 100 µm PCL in region V/VI)

2-way ANOVA	Significance $\alpha = 0.05/0.1$?	Summary	*P*-value$^{\text{Holm-Sidak}}$
WT::P290R/+ (Age 1)	NO	*n.s.*	0.784
WT::P290R/+ (Age 2)	YES	*	0.012
WT::P290R/+ (Age 3)	NO	*n.s.*	0.371
WT::P290R/+ (Age 4)	YES	**	0.005
WT::P290R/+ (Age 5)	YES	***	<0.001
WT::P290R/+ (Age 6)	YES	***	<0.001
WT::P290R/+ (Age 7)	YES	***	<0.001
WT::P290R/+ (Age 8)	YES	***	<0.001

Figure 2B (mean numbers of GFAP fibers per 100 µm PCL in region IX/X)

2-way ANOVA	Significance $\alpha = 0.05/0.1$?	Summary	*P*-value$^{\text{Holm-Sidak}}$
WT::P290R/+ (Age 1)	NO	*n.s.*	0.795
WT::P290R/+ (Age 2)	NO/YES	*n.s.*	0.099
WT::P290R/+ (Age 3)	NO	*n.s.*	0.318
WT::P290R/+ (Age 4)	YES	*	0.018
WT::P290R/+ (Age 5)	YES	***	<0.001
WT::P290R/+ (Age 6)	YES	***	<0.001
WT::P290R/+ (Age 7)	YES	***	<0.001
WT::P290R/+ (Age 8)	YES	***	<0.001

Age groups: P5-6 (1), P8-9 (2), P10 (3), P11-12 (4), P15-20 (5), P24-P35 (6), P45-65 (7), P538-P950 (8)

Figure 2C (median BGC$^+$ cells/100 µm PCL in region V/VI)

2-way ANOVA	Significance α = 0.05/0.1 ?	Summary	*P*-value$^{\text{Holm-Sidak}}$
WT::P290R/+ (PCL)	YES	***	<0.001
WT::P290R/+ (ectopic)	NO	*n.s.*	0.185

Figure 2C (median BGC$^+$cells/100 µm PCL in region IX/X)

2-way ANOVA	Significance α = 0.05/0.1 ?	Summary	*P*-value$^{\text{Holm-Sidak}}$
WT::P290R/+ (PCL)	YES	***	<0.001
WT::P290R/+ (ectopic)	NO	*n.s.*	0.298

Figure 2F (median NeuN$^+$ cells /mm^2)

2-way ANOVA	Significance α = 0.05/0.1 ?	Summary	*P*-value$^{\text{Holm-Sidak}}$
WT::P290R/+ (P20–P40)	YES	**	0.002
WT::P290R/+ (P41-100)	YES	*	0.025
WT::P290R/+ (>P100)	YES	***	0.001

Figure 2G (median GFAP$^+$ cells/mm^2)

2-way ANOVA	Significance α = 0.05/0.1 ?	Summary	*P*-value$^{\text{Holm-Sidak}}$
WT::P290R/+ (P20–P40)	NO/YES	*n.s.*	0.093
WT::P290R/+ (P41–100)	NO	*n.s.*	0.121
WT::P290R/+ (>P100)	YES	**	0.002

Figure 3B (median VGLUT1$^+$ clusters /100 µm^2)

2-way ANOVA	Significance α = 0.05/0.1 ?	Summary	*P*-value$^{\text{Holm-Sidak}}$
WT::P290R/+ (V/VI)	YES	***	<0.001
WT::P290R/+ (VI)	YES	**	0.006
WT::P290R/+ (IX/X)	YES	**	0.003
WT::P290R/+ (X)	YES	***	<0.001

Figure 3C (median VGLUT2$^+$ clusters /100 µm^2)

2-way ANOVA	Significance α = 0.05/0.1 ?	Summary	*P*-value$^{\text{Holm-Sidak}}$
WT::P290R/+ (V/VI)	YES	***	<0.001
WT::P290R/+ (VI)	YES	*	0.049
WT::P290R/+ (IX/X)	YES	***	<0.001
WT::P290R/+ (X)	YES	*	0.015

Figure 3D (median GAD65/67$^+$ clusters /100 µm^2)

2-way ANOVA	Significance α = 0.05/0.1 ?	Summary	*P*-value$^{\text{Holm-Sidak}}$
WT::P290R/+ (V/VI)	YES	*	0.046
WT::P290R/+ (VI)	NO	*n.s.*	0.123
WT::P290R/+ (IX/X)	NO	*n.s.*	0.595
WT::P290R/+ (X)	NO	*n.s.*	0.867

Figure 4A (mean current amplitudes, pA)

***U*-test**	**Significance α = 0.05/0.1 ?**	**Summary**	***P*-value**
WT::P290R/+	YES	*	0.024

Figure 4C (normalized current amplitudes at -100/-120 mV, pA)

2-way ANOVA(repeated measures)	**Significance α = 0.05/0.1 ?**	**Summary**	***P*-value**
WT::P290R/+ (-100 mV)	YES	*	0.025
WT::P290R/+ (-120 mV)	YES	*	0.017
WT, -80 mV::-100/120 mV	NO/NO	*n.s./n.s.*	0.628/0.282
P290R/+, -80 mV::-100/-120 mV	YES/YES	*/**	0.024/0.004

Figure 4E (Comparisons WT :: P290R: [Cl$^-$]$_{int}$, mM)

***2-way* ANOVA**	**Significance α = 0.05/0.1 ?**	**Summary**	***P*-value$^{Holm-Sidak}$**
WT::P290R/+ (P4-7)	YES	***	<0.001
WT::P290R/+(P8-10)	YES	***	<0.001
WT::P290R/+(P11-12)	YES	***	<0.001
WT::P290R/+(P13-15)	NO/YES	*n.s.*	0.09

Figure 4 F (Comparisons WT :: P290R+UCPH101: [Cl$^-$]$_{int}$, mM)

***1-way* ANOVA on ranks**	**Significance α = 0.05 ?**	**Summary**	**Dunn´s test**
WT::P290R/+(P4-12)	YES	***	YES
WT::WT-P290R/+^{UCPH}(P4-12)	NO	*n.s.*	NO

1-way ANOVA on ranks WT::P290R/+: $P < 0.001$

Figure 5B (left, total apoptotic events)

2-way ANOVA	**Significance α = 0.05/0.1 ?**	**Summary**	***P*-value$^{\text{Holm-Sidak}}$**
WT::P290R/+ (P8-9)	NO/YES	*n.s.*	0.074
WT::P290R/+ (P10)	YES	**	0.008
WT::P290R/+ (P11)	YES	*	0.043
WT::P290R/+ (P12)	YES	*	0.015
WT::P290R/+ (P13)	NO/YES	*n.s.*	0.073
WT::P290R/+ (P14-15)	NO	*n.s.*	0.56

Figure 5B (right, colocalized GFAP-EGFP/CASP3 signals)

2-way ANOVA	**Significance α = 0.05/0.1 ?**	**Summary**	***P*-value$^{\text{Holm-Sidak}}$**
WT::P290R/+ (P8-9)	NO/YES	*n.s.*	0.056
WT::P290R/+ (P10)	YES	*	0.038
WT::P290R/+ (P11)	YES	***	<0.001
WT::P290R/+ (P12)	YES	***	<0.001
WT::P290R/+ (P13)	YES	*	0.045
WT::P290R/+ (P14-15)	NO	*n.s.*	0.369

Figure 5E, (*left*, colocalized GFAP-EGFP/TUNEL signals)

***1-way* ANOVA on ranks**	**Significance α = 0.05/0.1 ?**	**Summary**	**Dunn´s test**
WT::P290R/+ (P9-14)	YES	***	YES

1-way ANOVA on ranks WT::P290R/+: $P = 0.001$

Figure 5E, *right* (total apoptosis events, TUNEL signals)

***1-way* ANOVA on ranks**	**Significance α = 0.05/0.1 ?**	**Summary**	**Dunn´s test**
WT::P290R/+ (P9-14)	YES	**	YES

1-way ANOVA on ranks WT::P290R/+: $P = 0.005$

Figure 6E (spiking frequencies of PCs, Hz)

2-way ANOVA	Significance α = 0.05/0.1 ?	Summary	*P*-value$^{\text{Holm-Sidak}}$
WT::P290R/+ (P10)	NO	*n.s.*	0.331
WT::P290R/+ (P20–30)	NO	*n.s.*	0.442
WT::P290R/+ (P40)	YES	***	<0.001

Figure 6F (covariances of PC spiking, CV)

2-way ANOVA	Significance α = 0.05/0.1 ?	Summary	*P*-value$^{\text{Holm-Sidak}}$
WT::P290R/+ (P10)	NO	*n.s.*	0.24
WT::P290R/+ (P20–30)	NO	*n.s.*	0.685
WT::P290R/+ (P40)	NO	*n.s.*	0.348

Figure 6G (covariances of PC spiking, mCV2)

2-way ANOVA	Significance α = 0.05/0.1 ?	Summary	*P*-value$^{\text{Holm-Sidak}}$
WT::P290R/+ (P10)	NO	*n.s.*	0.242
WT::P290R/+ (P20–30)	NO	*n.s.*	0.605
WT::P290R/+ (P40)	NO	*n.s.*	0.383

Figure 7C (CF-pauses of PCs, s)

U-test	Significance α = 0.05/0.1 ?	Summary	*P*-value
WT::P290R/+	YES	*	$P = 0.014$

Figure 8B (transversal cerebellar areas, mm^{2})

2-way ANOVA	Significance α = 0.05/0.1 ?	Summary	*P*-value$^{\text{Holm-Sidak}}$
WT$^{♂}$::P290R/+$^{♂}$ (H_l)	NO/YES	*n.s.*	0.077
WT$^{♂}$::P290R/+$^{♂}$ (H_r)	NO	*n.s.*	0.177
WT$^{♂}$::P290R/+$^{♂}$ (V_a)	YES	*	0.032
WT$^{♂}$::P290R/+$^{♂}$ (V_p)	YES	***	<0.001
Σ WT$^{♂}$::P290R/+$^{♂}$	**YES**	**	**0.005**
WT$^{♀}$::P290R/+$^{♀}$ (H_l)	YES	***	<0.001
WT$^{♀}$::P290R/+$^{♀}$ (H_r)	YES	***	<0.001
WT$^{♀}$::P290R/+$^{♀}$ (V_a)	YES	**	0.004
WT$^{♀}$::P290R/+$^{♀}$ (V_p)	YES	***	0.001
Σ WT$^{♀}$::P290R/+$^{♀}$	**YES**	***	**<0.001**

(H_l: left hemisphere; H_r: right hemisphere; V_a: anterior vermis; V_p: posterior vermis)

Figure 8D (sagittal cerebellar areas, vermis, mm^{2})

2-way ANOVA	Significance α = 0.05/0.1 ?	Summary	*P*-value$^{\text{Holm-Sidak}}$
WT::P290R/+ (*WM*)	NO	*n.s.*	0.154
WT::P290R/+ (*GCL*)	YES	***	<0.001
WT::P290R/+ (*ML*)	YES	***	<0.001
Σ WT::P290R/+ (*Vermis*)^{t}	**YES**	**	**0.002**

(WM: white matter; GCL: granule cell layer; ML: molecular layer)

Supplementary Figure 3B (latencies to first error, s)

2-way ANOVA (*repeated measures)*	Significance $\alpha = 0.05/0.1$?	Summary	P-value$^{\text{Holm-Sidak}}$
WT::P290R/+ $^{\textit{Trial I}}$	YES	*	0.01
WT::P290R/+ $^{\textit{Trial II}}$	YES	**	0.005
WT::P290R/+ $^{\textit{Trial III}}$	YES	**	0.004

Supplementary Figure 4D (relative protein expression, normalized)

2-way ANOVA	Significance $\alpha = 0.05/0.1$?	Summary	*P*-value$^{\text{Holm-Sidak}}$
WT::P290R/+ (BLBP)	YES	**	0.004
WT::P290R/+ (S100β)	YES	**	0.007
WT::P290R/+ (GLAST)	YES	***	<0.001

Supplementary Figure 8A (width of ML, µm)

2-way ANOVA	Significance $\alpha = 0.05/0.1$?	Summary	P-value$^{\text{Holm-Sidak}}$
WT::P290R/+ VI_{int}	NO	*n.s.*	0.226
WT::P290R/+ VI_{ext}	NO	*n.s.*	0.524
WT::P290R/+ X_{int}	NO	*n.s.*	0.880
WT::P290R/+ X_{ext}	YES	*	0.041

Supplementary Figure 8B (number of PCs, N/100 µm PCL)

2-way ANOVA	Significance $\alpha = 0.05/0.1$?	Summary	P-value$^{\text{Holm-Sidak}}$
WT::P290R/+ VI_{int}	NO	*n.s.*	0.884
WT::P290R/+ VI_{ext}	YES	**	0.003
WT::P290R/+ X_{int}	NO	*n.s.*	0.340
WT::P290R/+ X_{ext}	NO	*n.s.*	0.233

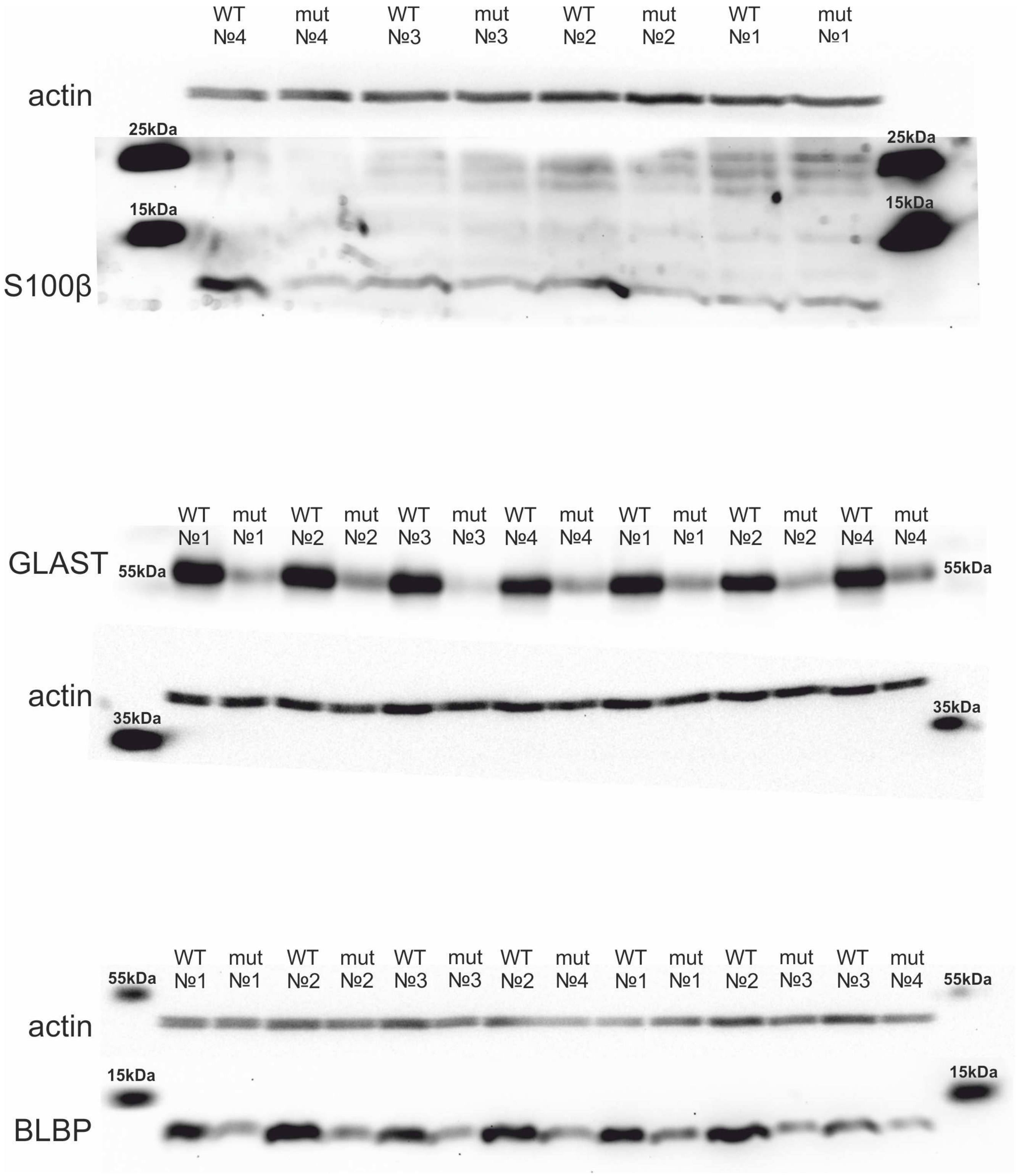

Supplement: Full length blots containing all tested animals for the markers S100β, GLAST, and BLBP. Signals were normalized to actin bands for quantification (Supplementary Material 1.8; Supplementary Fig. 4) Details about the used antibodies are provided in Supplementary Table 2